Development of solid-state electrolyte for lithium batteries

Nuno Filipe Aguiar Eusébio
Master in Engineering Physics
Department of Physics and Astronomy
Faculty of Sciences of the University of Porto
and Faculty of Engineering of
the University of Porto
2024

This page is intentionally left blank.

Development of solid-state electrolyte for lithium batteries

Nuno Filipe Aguiar Eusébio
Master in Engineering Physics
Department of Physics and Astronomy
2024

Supervisor
Profª. Drª. Helena Braga, Associate Professor, Faculty of Engineering, University of Porto

External Host Supervisor
Drª. Liliana Truta, Researcher, CeNTI – Centre for Nanotechnology and Smart Materials

This page is intentionally left blank.

"You miss 100 % of the shots you don't take. - Wayne Gretzky"

Michael Scott

This page is intentionally left blank.

Acknowledgements

First, I would like to express my gratitude to my two supervisors, Professor Helena Braga and Researcher Liliana Truta, for their guidance, help, and teachings over the past nine months. I also thank them for their patience, encouragement, and constant support, always willing to share their knowledge and guide me during the most challenging moments.

A special thank you as well to the entire CeNTI team, especially to João Teixeira, Sónia Alves, and Pedro Sampaio, for the technical support, constant collaboration, and for the welcoming and motivating work environment that contributed so much to the completion of this project.

To Beatriz Gomes and Manuela Baptista, collaborators at MatER, thank you very much for your support in the final stretch of my thesis.

I am also grateful to all the professors who shared their knowledge and experience with me, contributing to my personal and professional development.

I would also like to extend my gratitude to my mother, father, and to Maria. Thank you, Mom, for teaching me to fight throughout my life and being my greatest example of resilience and strength. Thank you, Dad, for always keeping me grounded and being a constant source of positivity in my life.

I cannot forget the rest of my family for all their support and the cold winters in Azêvo, where I would sit in front of the fireplace while my grandmothers would always say to me, "Oh my dear, don't wear yourself out with those books."

A thank you also to my childhood friends from Aveiro, who, although we didn't become football players as we once dreamed, continue to celebrate each other's achievements in our new paths.

To the friends I made over these 5 years of study at FCUP, thank you for fighting and overcoming every obstacle together, including the long nights trying to understand quantum mechanics.

This page is intentionally left blank.

Abstract

This thesis investigates the creation of solid-state electrolytes for lithium batteries, which is an important topic for developing electrochemical energy storage. The study was carried out during an internship at CeNTI, an institute dedicated to intelligent materials and nanotechnology research. The focus was on synthesizing and analysing solid polymer electrolytes (SPEs) and their integration, along with amorphous glass ferroelectric electrolytes, into coin cells with lithium metal anodes and Lithium Iron Phosphate (LFP) cathodes.

This study underscores the importance of optimizing Lithium Perchlorate ($LiClO_4$) concentration and polymer matrix selection to improve electrolyte properties. Composites of Polyvinylidene Fluoride (PVDF), Polyvinyl Alcohol (PVA), and Sodium Alginate (Na-Alg) with varying $LiClO_4$ concentrations were prepared. Techniques like FTIR, mechanical testing, porosity analysis, and electrochemical impedance spectroscopy were used for characterization. Results show that higher $LiClO_4$ concentrations increase ionic conductivity due to more mobile ions, though mechanical stability worsens significantly. In a Swagelok cell with steel electrodes, the highest ionic conductivity, 1.30×10^{-5} S cm^{-1}, was achieved with 40:60 PVA / NaAlg / 20 % $LiClO_4$ of the total polymer content

Incorporating amorphous glass ferroelectric electrolytes, such as Lithium Barium Perchlorate ($Li_{2.99}Ba_{0.005}ClO$), into solid polymer electrolytes (SPE) enhances lithium battery performance. This improvement is achieved by inducing inductive behavior, reducing internal resistance, and increasing ionic conductivity through ion polarization within the SPE. The combination of polymeric and amorphous glass ferroelectric electrolytes presents a promising strategy for developing more efficient and durable lithium batteries.

Keywords: Electrochemical Energy Storage; Ferroelectric Electrolytes; Inductive behavior; Inorganic Electrolytes; Lithium Batteries; Solid-state Electrolytes; Solid Polymer Electrolytes.

This page is intentionally left blank.

Resumo

Esta tese investiga a criação de eletrólitos em estado sólido para baterias de lítio, um tema importante para o desenvolvimento de sistemas de armazenamento de energia eletroquímica. O estudo foi realizado durante um estágio no CeNTI, um instituto dedicado à investigação de materiais inteligentes e nanotecnologia. O foco foi a síntese e análise de eletrólitos poliméricos sólidos (SPEs) e sua integração, juntamente com eletrólitos ferroelétricos vítreos amorfos, em coin cells com ânodos de lítio metálico e cátodos de Fosfato de Ferro e Lítio (LFP).

Este estudo destaca a importância de otimizar a concentração de Perclorato de Lítio ($LiClO_4$) e a seleção da matriz polimérica para melhorar as propriedades dos eletrólitos. Foram preparados compósitos de Fluoreto de Polivinilideno (PVDF), Álcool Polivinílico (PVA) e Alginato de Sódio (NaAlg) com diferentes concentrações de $LiClO_4$. Técnicas como FTIR, testes mecânicos, análise de porosidade e espectroscopia de impedância eletroquímica foram utilizadas para caracterização. Os resultados mostram que concentrações mais elevadas de $LiClO_4$ aumentam a condutividade iónica devido a mais iões móveis, embora a estabilidade mecânica piore significativamente. Em uma célula Swagelok com eletrodos de aço, a maior condutividade iônica, 1.30×10^{-5} S cm^{-1}, foi alcançada com 40:60 PVA / NaAlg / 20 % de $LiClO_4$ em relação ao polímero total.

A incorporação de eletrólitos ferroelétricos vítreos amorfos, como Perclorato de Lítio e Bário ($Li_{2.99}Ba_{0.005}ClO$), em eletrólitos poliméricos sólidos (SPE) melhora o desempenho das baterias de lítio. Esta melhoria é alcançada por meio da indução de comportamento indutivo, redução da resistência interna e aumento da condutividade iónica através da polarização dos iões dentro do SPE. A combinação de eletrólitos poliméricos e eletrólitos ferroelétricos vítreos amorfos apresenta uma estratégia promissora para o desenvolvimento de baterias de lítio mais eficientes e duráveis.

Palavras-chave: Armazenamento de Energia Eletroquímica; Baterias de Lítio; Comportamento indutivo; Eletrólitos Ferroelétricos; Eletrólitos Inorgânicos; Eletrólitos Poliméricos Sólidos; Eletrólitos Sólidos.

This page is intentionally left blank.

Contents

Acknowledgements i

Abstract iii

Resumo v

Contents x

List of Tables xi

List of Figures xv

Acronyms xvii

1 Introduction 1

1.1 Context 1

1.2 CeNTI 1

1.3 Motivation 1

1.4 Objectives 2

2 State of the Art 3

2.1 Energy Storage Technologies 3

2.2 Batteries History 4
2.3 The Role of Lithium in Energy Storage: Advantages, Challenges, and Global Impact 5
2.4 Battery Operation and Composition 6
2.5 Considerations for Assessing Battery Quality 10
2.6 Classifications of Lithium-Ion Batteries 11
2.7 Electrolytes 13
2.8 Liquid electrolytes 14
2.9 Solid electrolytes 15
2.9.1 Gel polymer electrolytes (GPE) 16
2.9.2 Solid polymer electrolytes (SPE) 16
2.9.3 Inorganic Li-Ion Electrolytes 17
2.9.4 Organic and inorganic composite electrolytes (OICSE) 18
2.10 Ion conduction in solid electrolytes 19
2.10.1 Ion conduction in amorphous and crystalline phases 19
2.10.2 Single ion conducting (SIC) and dual ion conducting (DIC) 20
2.10.3 Nernst-Einstein equation 22
2.10.4 Arrhenius Model 22
2.11 Key components of SPEs: salts and polymer hosts 23
2.11.1 Lithium perchlorate ($LiClO_4$) as a conductive salt 23
2.11.2 Polyvinylidene fluoride (PVDF) as polymer matrix 23
2.11.3 Polyvinyl Alcohol (PVA) as a polymer matrix 25
2.11.4 PVA / Sodium Alginate (NaAlg) as polymer matrix 26
2.11.5 $Li_{2.99}Ba_{0.005}ClO$ as amorphous glass ferroelectric electrolyte 27

3 Experimental Techniques **29**

3.1 Reaction materials . . . 29

3.2 Methods . . . 30

3.2.1 Drop cast . . . 30

3.2.2 Doctor Blade . . . 30

3.2.3 Non-solvent induced phase separation (NIPS) . . . 31

3.3 Synthesized electrolytes . . . 32

3.3.1 $Li_{2.99}Ba_{0.005}ClO$ electrolyte . . . 32

3.3.2 PVDF / $LiClO_4$ electrolyte . . . 32

3.3.3 PVA / NaAlg / $LiClO_4$ electrolyte . . . 33

3.4 Coin cell assembly . . . 34

3.4.1 LFP as cathode . . . 34

3.4.2 Lithium metallic as anode . . . 35

3.5 Characterisation Techniques . . . 35

3.5.1 Fourier Transform Infrared Spectroscopy . . . 35

3.5.2 Determining the porosity of the membrane using n-butanol . . . 36

3.5.3 Mechanical test . . . 37

3.5.4 Laser Induced Breakdown Spectroscopy (LIBS) . . . 38

3.6 Electrochemical Analysis . . . 38

3.6.1 Electrochemical Impedance Spectroscopy . . . 39

3.6.1.1 Impedance Components in Electrochemical Systems . . . 42

3.6.2 Cyclic Voltammetry . . . 43

3.6.3 Chronoamperometry . . . 45

3.6.4 Galvanostatic Charge and Discharge . . . 46

4 Results and Discussion **47**

4.1 Solid Electrolyte - PVDF / $LiClO_4$ 47

4.1.1 FTIR in PVDF membrane 47

4.1.2 PVDF membrane porosity 49

4.1.3 PVDF / $LiClO_4$ membrane porosity 50

4.1.4 LIBS study in PVDF / $LiClO_4$ 51

4.1.5 FTIR in PVDF / $LiClO_4$ 52

4.1.6 Arrehenius law - PVDF / $LiClO_4$ 53

4.1.7 Lithium charge transfer calculated by Chronoamperometry- PVDF / $LiClO_4$ 55

4.1.8 $LiClO_4$ Concentration Optimization 55

4.2 Solid Electrolyte: PVA / NaAlg / $LiClO_4$ 57

4.2.1 PVA / NaAlg FTIR analyse 57

4.2.2 Porosity test in PVA / NaAlg / $LiClO_4$ membrane 58

4.2.3 Mechanical Properties of PVA / NaAlg / $LiClO_4$ membrane 60

4.2.4 Arrhenius law - PVA / NaAlg / $LilClO_4$ 61

4.2.5 Lithium charge transfer- PVA / NaAlg / $LilClO_4$ 62

4.2.6 $LiClO_4$ Concentration Optimization 62

4.3 Coin cell 64

5 Conclusions and Future Work **69**

References **71**

List of Tables

2.1 Key Historical Developments in Battery Technology 4

2.2 Battery Parameters and Descriptions 11

2.3 Comparison of different types of lithium-ion batteries - part 1 [32] 12

2.4 Comparison of different types of lithium-ion batteries - part 2 [32] 13

2.5 Categories of Polymer Electrolytes. 17

4.1 Ionic conductivity of PVDF / $LiClO_4$ electrolytes made by NIPS and Doctor Blade 56

4.2 Mechanical properties of 40:60 and 60:40 PVA / NaAlg blends with different $LiClO_4$ concentrations. 61

4.3 Activation Energy (Ea) of PVA / NaAlg blends with varying $LiClO_4$ concentrations. 61

4.4 Transference number (t_{Li^+}) of PVA / NaAlg blends with varying $LiClO_4$ concentrations. 62

4.5 Ionic conductivity of PVA / NaAlg blends with varying $LiClO_4$ concentrations. . 63

4.6 Summary of cell parameters and theoretical specific capacity for different PVDF and PVA / NaAlg blends with $LiClO_4$ and $Li_{2.99}Ba_{0.005}ClO$ additives. 65

This page is intentionally left blank.

List of Figures

2.1 Comparison of fuel cells, batteries, supercapacitors, and capacitors. Source: [6] . 3

2.2 Comparing the gravimetric and volumetric capacities, standard reduction potential, and abundance in the Earth's crust of metal anodes used or proposed for electrochemical storage systems. [13] 5

2.3 Comparison of the composition of a lithium-ion battery and a solid-state battery. Source: [14] 6

2.4 Battery Dendrites in traditional Lithium-metal cell. Source: [18] 7

2.5 Discharge process of a battery. Source: [1] 8

2.6 The SEI film production process follows a near-shore aggregation mechanism rather than a surface development strategy. Source: [23] 10

2.7 Type of electrolytes 14

2.8 Characteristics of three common electrolytes in lithium batteries. [39] 19

2.9 Schematic of Li ion transport pathways in two types of SPEs: a) typical amorphous SPEs; b) specific crystalline complex SPEs. [57] 20

2.10 Cyclic Voltammogram for Dual-Ion Conduction and Single-Ion Conduction.Source: [60] 21

2.11 Diagram showing the chain conformation for PVDF's α, β, and γ phases. [64] . . 24

3.1 Drop cast method [79] 30

3.2 Doctor blade apparatus where the spreading speed of the solution can be adjusted (left) and electrolyte solution to be spread (right) 31

3.3 Non-solvent induced phase separation (NIPS) process: (a) polymer dissolution, (b) solution spreading, (c) Dispensing solution on substrate with Mayer bar, (d) immersion in the coagulation bath, (e) phase inversion and (f) membrane drying. 32

3.4 On the left: Coin cell using SPE. On the right: Coin cell using SPE and amorphous glass ferroelectric electrolyte ($Li_{2.99}Ba_{0.005}ClO$). 34

3.5 Mid-infrared representative spectrum. The fingerprint region is the region below 1500 cm^{-1}. The functional group region is above 1500 cm^{-1}. Source: [87] 36

3.6 Mechanical testing machine 37

3.7 On the left: gold electrodes (gold/SPE/gold). On the right: Swagelok cell with steel electrodes. [93] 38

3.8 Nyquist graphs for various electrical circuits. a) Pure resistance R (only real part of the impedance); b) Pure capacitor C (only imaginary part of the impedance); c) R and C in series; d) R and C in parallel; e) R and C in parallel connected in series with a resistance (there is a shift to the right in relation to graph d) due to this series resistance); f) The same circuit as in e) but with a capacitor in extra series. g) Randles-Ershler circuit, with R_1 and R_2 being highlighted in this EIS graph.[94, 95] 39

3.9 Generic physical model for EIS investigation of SSBs. [96] 41

3.10 Inductive behavior in SSBs. [98] 42

3.11 Typical CV diagram (a) for an ideal supercapacitor; (b) with mostly resistive behavior; (c) of a device of distorted energy storage due to faradaic reactions . . 43

3.12 Left: Typical reversible cyclic voltammogram characteristics; Right: Effect of increasing scan rate on CV. [102] 44

3.13 Typical chronoamperometry [103] 45

3.14 Typical charge and discharge voltage versus capacity. [106] 46

4.1 FTIR-ATR spectra of the different PVDF membranes 48

4.2 β phase content of the PVDF membranes 48

4.3 PVDF membrane using the NIPS method 49

4.4 Porosity comparison of PVDF membrane with different $LiClO_4$ concentrations, (a) by the Doctor Blade method; (b) by the NIPS method 50

4.5 LIBS study in PVDF / $LiClO_4$ electrolyte made by NIPS 51

4.6 FTIR study in PVDF / $LiClO_4$ membranes, (a) by NIPS method; (b) by Doctor Blade method. 52

4.7 FTIR test in PVDF / $LiClO_4$ electrolyte 53

4.8 Impedance spectra of 15% PVDF 20% $LiClO_4$ at various temperatures. 54

4.9 Chronoamperometry- 15% PVDF / 20% $LiClO_4$ SPE made by Doctor Blade . . 55

4.10 Equivalent circuit and its fitting of 15% PVDF / 20% $LiClO_4$ SPE made by NIPS 56

4.11 FTIR test in 60:40 PVA / NaAlg / (5,10,20) % $LiClO_4$ electrolytes and in 40:60 PVA / NaAlg / (5,10,20) % $LiClO_4$ 58

4.12 Porosity test in 60:40 PVA / NaAlg / (5,10,20) % $LiClO_4$ electrolytes and in 40:60 PVA / NaAlg / (5,10,20) % $LiClO_4$ 59

4.13 Tensile stress-strain curves for PVA-NaAlg membranes in machine direction/ Doctor Blade direction (DB) 60

4.14 Equivalent circuit and its fitting of of 40:60 PVA / NaAlg / 20% $LiClO_4$ SPE made by Doctor Blade 63

4.15 EIS - Coin Cell NE01 40:60 PVA / NaAlg / 20% $LiClO_4$ 66

4.16 EIS - Coin Cell CC03 40:60 PVA / NaAlg / 20% $LiClO_4$ / LiBa 66

4.17 CV- Coin Cell NE01 40 % PVA / 60 % NaAlg / 20% $LiClO_4$ 66

4.18 CV- Coin Cell CC03 40 % PVA / 60 % NaAlg / 20% $LiClO_4$ / LiBa 66

4.19 Charge/discharge of the NE01 coin cell using SPE (40% PVA, 60% NaAlg, 20% $LiClO_4$). Left: potential vs. time. Right: capacitance vs. time. 67

This page is intentionally left blank.

Acronyms

CA Chronoamperometry

CeNTI Centre for Nanotechnology and Advanced Materials

CPE Constant Phase Element

CV Cyclic Voltammetry

DIC Dual Ion Conducting

EDLC Electrical Double-Layer Capacitor

Ea Activation Energy

EIS Electrochemical Impedance Spectroscopy

FTIR Fourier-Transform Infrared Spectroscopy

FCUP Faculty of Science of University of Porto

FEUP Faculty of Engineering of University of Porto

GPEs Gel Polymer Electrolytes

GCD Galvanostatic Charge and Discharge

HOMO Highest Occupied Molecular Orbital

ISE Inorganic Solid Electrolytes

LIB Lithium-Ion Batteries

LIBS Laser-Induced Breakdown Spectroscopy

LiBa Lithium Barium Perchlorate ($Li_{2.99}Ba_{0.005}ClO$) electrolyte

LFP Lithium Iron Phosphate

LUMO Lowest Unoccupied Molecular Orbital

MatER Materials for Energy Research

NaAlg Sodium Alginate

NIPS Non-Solvent Induced Phase Separation

NMC Nickel Manganese Cobalt

O-ICSE Organic and Inorganic Composite Electrolytes

PEC Polycarbonate

PDMS Poly(dimethylsiloxane)

PEO Poly(ethylene oxide)

PMMA Poly(methyl methacrylate)

PPC Polypropylene carbonate

PVDF Poly(vinylidene fluoride)

PVA Poly(vinyl alcohol)

PVC Poly(vinyl chloride)

PVP Poly(vinylpyrrolidone)

PTMC Poly(trimethylene carbonate)

SC Solid-State Cells

SIC Single Ion Conducting

SN Succinonitrile

SSEs Solid-State Electrolytes

SSBs Solid-State Batteries

SPEs Solid Polymer Electrolytes

SEI Solid Electrolyte Interphase

$\mathbf{R}_{CT}$ Charge Transfer Resistance

$\mathbf{R}_{SOL}$ Solution Resistance

W Warburg Impedance

Chapter 1

Introduction

1.1 Context

The growing global energy demand, driven by population growth, has intensified the search for sustainable energy sources. Lithium-ion batteries are the most popular, used in electric vehicles and electronic devices due to their low weight and high charge capacity (3860 $mAhg^{-1}$) [1]. Lithium has a low density and high chemical potential, providing energy efficiency. However, its low abundance in the Earth's crust and restricted location of reserves pose political and economic challenges, thus leading the European Union to consider this a critical material. [2]

1.2 CeNTI

CeNTI (Center for Nanotechnology and Smart, Functional, and Technical Materials) is an institution dedicated to R&D activities in the fields of nanotechnology, advanced materials, and intelligent systems. CeNTI develops customizable solutions for energy generation and storage, sustainable new materials, and flexible solid-state batteries. Additionally, it offers diagnostic and reconditioning services for second-life batteries. [3]

1.3 Motivation

The main motivation of this thesis is to address the challenge of low ionic conductivity in current solid polymer electrolytes. This work aims to develop new electrolytes that combine high

ionic conductivity with excellent mechanical stability. [4].

1.4 Objectives

The primary objective of this thesis is to develop and characterize solid polymer electrolytes (SPEs) for lithium batteries, focusing on improving ionic conductivity, mechanical properties, and chemical stability. This research aims to:

- Synthesize SPEs using PVDF, PVA, NaAlg, and $LiClO_4$.
- Evaluate SPEs using FTIR, mechanical testing, porosity analysis, and electrochemical impedance spectroscopy.
- Assess the performance of SPEs in coin cells to determine optimal configurations.
- Investigate the impact of adding amorphous glass ferroelectric electrolyte, such as $Li_{2.99}Ba_{0.005}ClO$, to the SPE when assembling coin cells.

The main goal is to advance next-generation lithium batteries with enhanced safety, performance, and longevity.

Chapter 2

State of the Art

2.1 Energy Storage Technologies

The comparison of capacitors, supercapacitors, batteries, and fuel cells reveals their various properties and uses in energy storage systems. While capacitors and supercapacitors can provide high energy densities, rapid recharging, and extended lifespans, batteries have comparatively large storage capacity but limited power. Fuel cells, on the other hand, have been acknowledged for their efficiency and energy density, although they are more complex and require additional infrastructure to operate. Each technology has advantages and disadvantages, making it appropriate for a variety of applications, including high-power energy storage and fast backup systems. Figure 2.1 shows the comparison of fuel cells, batteries, supercapacitors, and capacitors. [5]

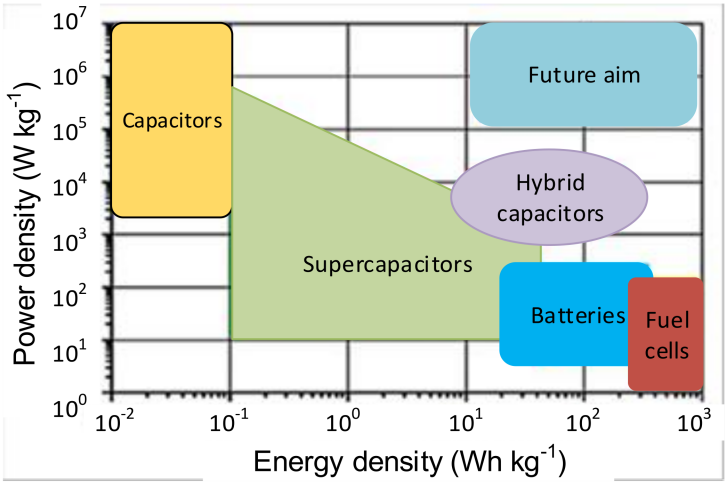

Figure 2.1: Comparison of fuel cells, batteries, supercapacitors, and capacitors. Source: [6]

The focus of the thesis was exclusively on the development of solid electrolytes for batteries, without addressing the other technologies mentioned.

2.2 Batteries History

The difficulty of meeting the world's energy needs has arisen from the population's exponential growth, which has raised interest in the quest for sustainable and renewable energy sources. [7]

The electrochemical cell, or battery, transforms chemical energy into electricity, a concept advanced by Luigi Galvani and Alessandro Volta in the 18th century. [8]

Table 2.1 outlines major milestones in the evolution of battery technology, highlighting the contributions of many scientists and inventors across time.

Table 2.1: Key Historical Developments in Battery Technology

Year	Scientist	Description
1800	Alessandro Volta	The voltaic pile, the first electric pile, was made of alternating copper and zinc discs stacked and connected by wires, immersed in sulfuric acid. It generated hydrogen bubbles, had limited voltage, and lasted about an hour. [8]
1836	John Frederic Daniell	Invented a different kind of battery by joining a stack of two metal electrodes, one composed of zinc and the other of copper, with a salt bridge in between. [9]
1859	Raymond Gaston Planté	Devised a lead-acid battery system using lead foil electrodes separated by textiles soaked in sulfuric acid. It could produce a voltage of up to 2 volts. [10]
1866	George Leclanché	Created the dry acid battery, widely used because of its affordability and versatility. [11]
1970s	Development of Lithium Batteries	The first lithium batteries were non-rechargeable, utilizing lithium's electrochemical potential. Lithium-ion batteries, with high energy density and safety, followed, and later, lithium-metal polymer batteries further increased storage capacity.[12]

In the next section, the challenges and application of lithium in metals are covered in more

depth.

2.3 The Role of Lithium in Energy Storage: Advantages, Challenges, and Global Impact

Due to its low density (0.534 g cm^{-3}), lithium has the highest theoretical charge storage capacity, at 3860 $mAhg^{-1}$. It is also recognized for its high absolute chemical potential, enabling battery cells to achieve the highest potential difference, directly influencing the power and energy stored and supplied to the circuit. [1]

There are also some drawbacks to be considered, notably regarding the abundance of lithium (Li) in the Earth's crust. Due to its low abundance in the Earth's crust and specific accessibility in certain regions of the globe, lithium exploration often results in political and/or economic barriers. According to the European Union (EU), Li is currently considered a critical raw material. [2]

Nowadays, an increasing number of people are seeking alternatives to Li-ion batteries.

Figure 2.2 compares metal anodes for electrochemical storage, highlighting their gravimetric and volumetric capacities, standard reduction potentials, and Earth crust abundance. It shows that lithium has the highest standard reduction potential and gravimetric capacity, making Li-ion batteries highly effective, despite lithium's lower abundance compared to other elements.

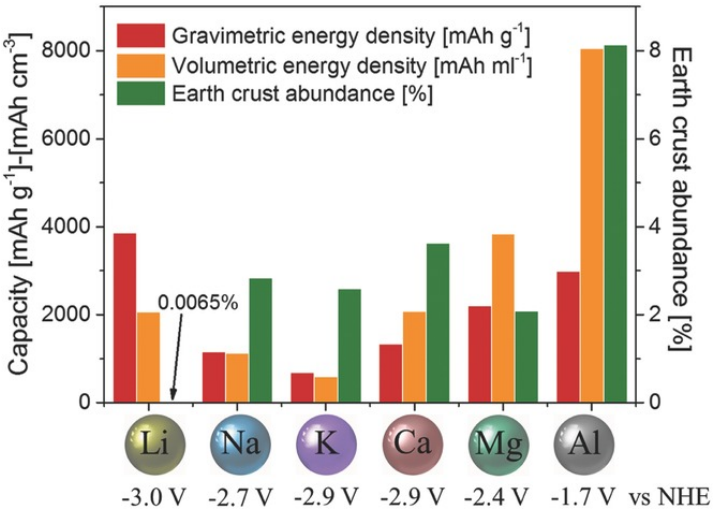

Figure 2.2: Comparing the gravimetric and volumetric capacities, standard reduction potential, and abundance in the Earth's crust of metal anodes used or proposed for electrochemical storage systems. [13]

Having explored the history and prospects of batteries, it is now crucial to understand how they work in detail.

2.4 Battery Operation and Composition

Generally, a rechargeable battery is composed of two electrodes, two current collectors, an electrolyte, and a separator. If the battery uses a solid electrolyte, there is no need for a separator, as the solid electrolyte functions as both the separator and ionic conductor. [1]

The electrodes are often referred to as the cathode and the anode. [1]

The figure below highlights the key differences in composition between lithium-ion batteries, which use liquid or gel electrolytes and require a separator, and solid-state batteries, which feature a solid electrolyte and eliminate the need for a separator. [14]

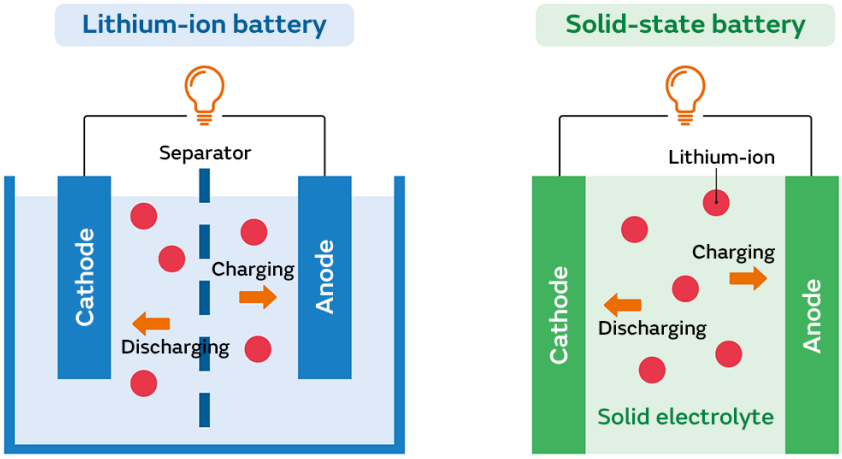

Figure 2.3: Comparison of the composition of a lithium-ion battery and a solid-state battery. Source: [14]

The focus of this thesis is the study of the solid electrolyte, the component between the cathode and anode in solid-state batteries (right scheme from figure 2.3)

In the standard configuration of a battery, the two electrodes are spatially isolated from each other but are electrically connected via an external circuit. This allows electrons to be transferred between the electrodes [15]. Aluminum and copper are the most commonly used current collectors in batteries due to their high electrical conductivity and stability. [16]

On the absolute scale, the anode has a higher potential than the cathode. During discharge, the positive electrode (cathode) is reduced, while the negative electrode (anode) releases electrons that flow through an external circuit from the anode to the cathode. During charging, the roles reverse: the positive electrode becomes the anode and undergoes reduction, while the negative electrode becomes the cathode and electrons flow through an external circuit from cathode to anode. [15]

In the case of discharge lithium-ion batteries, the transfer of electrons from the anode to the cathode is accompanied by the extraction of lithium ions (Li^+) from the anode, which is subsequently inserted into the cathode, thus balancing the charges. [1]

When lithium-ion batteries are charged quickly, especially at low temperatures, lithium cations can accumulate on the surface of the negative electrode, forming dendrites which in turn can puncture the separator between the electrodes, causing a short circuit [17], as shown in the figure 2.4.

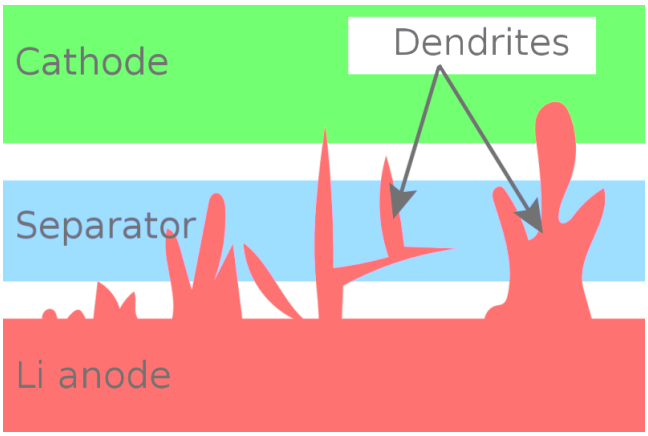

Figure 2.4: Battery Dendrites in traditional Lithium-metal cell. Source: [18]

When dendrites and internal short circuits occur, most electrons follow this path, realizing heat according to Joule's law and increasing the risk of fire and explosion, especially as liquid or gel electrolytes are flammable and can release oxygen. [17]

Lithium-ion batteries are designed to be initially used in a discharged state. In other words, when these batteries are manufactured, the cathode already contains lithium ions because this is the stable condition (Lithiated Phase). During discharge, the cathode is charged with more lithium ions. Therefore, to use a lithium-ion battery, it must first be charged. During the charging process, it is essential to provide enough energy to overcome the potential difference ε (V), which is the difference in energy between the discharged and charged states of the battery.[1]

$$\epsilon = \frac{\mu_A - \mu_C}{e} \tag{2.1}$$

Where μ_A and μ_C are the chemical potentials (in eV) of the negative (anode) and positive (cathode) electrodes, respectively, during discharge, with e as the electron charge. [1]

However, a battery cannot be considered an ideal system. Part of the energy it generates is consumed to induce the directional movement of ions in the electrolyte, as well as to promote the displacement of electrons in the electrodes to the active surfaces [1]. In some cases, this energy is also dissipated, as there is a nonzero probability that electrons will overcome quantum energy barriers towards the electrolyte. This phenomenon is due to the discrete nature of the energy levels of electrons, which can only occupy discrete values, not a continuous range of values. [19]

During the discharge process of a battery, there are three distinct stages, each associated with a specific phenomenon, illustrated by figures (A), (B), and (C) from figure 2.5. In the first stage, figure 2.5 (A), we observe the difference in the chemical potentials of the electrodes and the molecular structure of the electrolyte, thus initiating the electrochemical process. When the battery is in an open circuit, parallel-plate capacitors, known as electric double-layer capacitors (EDLCs), are formed as cations migrate to the electrolyte/cathode interface due to the higher chemical potential of the cathode compared to the electrolyte. Figure 2.5 (B): This configuration allows the electrochemical potentials between the electrodes and the electrolyte to be balanced, even in an open circuit. As the discharge proceeds, the battery enters a state of dynamic equilibrium, as indicated in figure 2.5 (C). At this stage, the potential differences across the flat capacitors fluctuate with changes in the absolute chemical potentials, driving the movement of ions within the electrolyte. As the chemical potentials approach equilibrium, the cations begin to move more freely, no longer hindered by Coulombic forces. This dynamic process plays a crucial role in ensuring the continuous operation of the battery during discharge. [1]

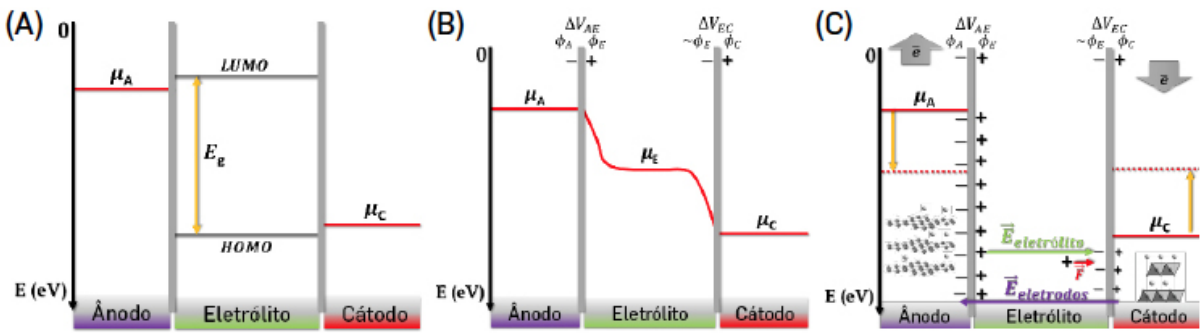

Figure 2.5: Discharge process of a battery. Source: [1]

Electric double-layer capacitors (EDLCs) are not uniform and depend on the electrolyte composition, the applied charge to the electrode, and the temperature [20]. It has potential differences: $\Delta V_{AE} = \phi_E - \phi_A$ and $\Delta V_{EC} = \phi_C - \phi_E$. Where ϕ_E is the potential at the electrolyte, ϕ_A is the potential at the anode and ϕ_C is the potential at the cathode. They are modeled as parallel-plate capacitors with capacitance equation 2.2:

$$C = \frac{\varepsilon_0 \varepsilon_r A}{d} \tag{2.2}$$

Where d is the plate separation, A is the area, ε_r is the relative permittivity, and ε_0 is the vacuum permittivity. The battery voltage is the sum of the voltage differences across these capacitors at the electrolyte-negative electrode interfaces. [1]

EDLC and the solid electrolyte interface (SEI) are crucial components for the performance and durability of lithium-ion batteries. EDLC directly affects which electrolyte species are reduced, impacting the formation of the SEI. [20, 21]

SEI layer on the anode of lithium-ion batteries is formed from lithium available in the cathode and the electrolyte salt. Its primary function is to prevent the decomposition of the electrolyte, which would otherwise consume more lithium ions. During the first charge cycle, approximately 10% of the battery's capacity is consumed in the initial formation of the SEI, resulting in irreversible capacity loss. [22]

The initial formation of the SEI involves reduction reactions on a bare electrode surface, where solvent molecules lower the surface voltage and influence the electric double-layer capacitor (EDLC), and this process is complemented by the aggregation of less soluble decomposition products near the surface to form a nanometer-thick SEI film on the anode. This "near-shore aggregation" mechanism allows the SEI to serve as a protective passivation layer. Formed from electrolyte decomposition products during charge and discharge cycles, this layer permits the passage of lithium ions while blocking electrons, thereby enhancing battery stability and efficiency. [23]

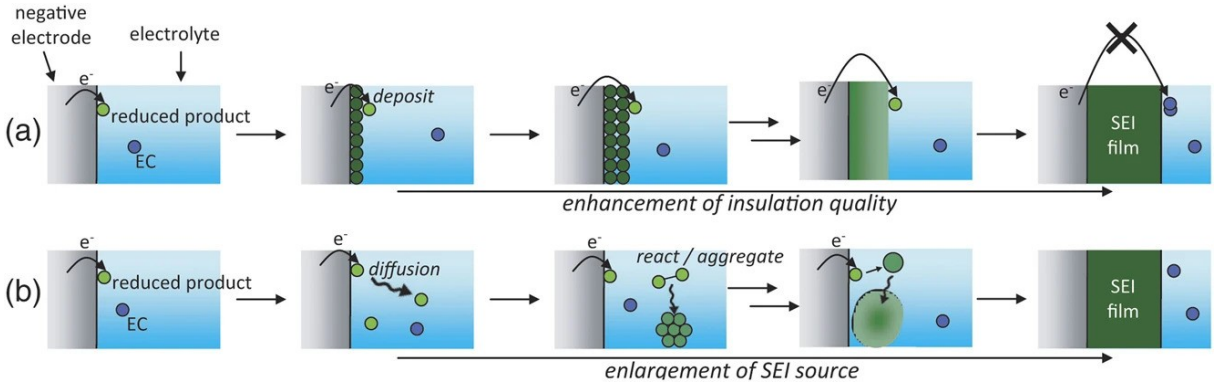

Figure 2.6: The SEI film production process follows a near-shore aggregation mechanism rather than a surface development strategy. Source: [23]

The initial SEI on lithium metal is typically rich in inorganic species, which slows its growth. Conversely, an SEI rich in organic components tends to grow more quickly. The SEI on lithium metal anodes comprises three main components: initial inorganic compounds, insoluble species formed from reactions with the electrolyte, and products of electrochemical reduction reactions. [24]

Balancing the anode's surface area with the amount of lithium available for SEI formation is crucial. An inadequate or continuously forming SEI over cycles can increase internal resistance, reduce efficiency, and decrease battery capacity. Ideally, the SEI should exhibit selective lithium permeability and stability across various thermal and electrochemical conditions. [22]

In conclusion, a detailed understanding of how batteries work is fundamental to exploring their benefits and limitations. The next section will cover the essential considerations for assessing the quality of batteries, highlighting the critical factors that influence their performance and safety.

2.5 Considerations for Assessing Battery Quality

When analysing a battery's effectiveness, several elements play crucial roles, requiring a meticulous evaluation of parameters such as specific charge, energy density, cyclic performance, and self-discharge rate, as is shown in table 2.2, to ensure its quality and long-lasting performance.

Table 2.2: Battery Parameters and Descriptions

Specific battery charge (mAh g^{-1})	Amount of charge it can store per unit mass. [25]
Energy density (E_{bat}) (Wh m^{-3})	Stored energy per unit volume. [26]
Gravimetric density (Wh kg^{-1})	Amount of energy the battery can store relative to its mass. $$\text{Gravimetric Density} = C \times V_{\text{avg}}$$ where C is the specific capacity (mAh/g), and V_{avg} is the average discharge voltage (volts). [26]
Cyclic performance	Battery behavior during several charging-discharging cycles. [27]
Operating Temperature Range (°C)	The range of temperatures within which the battery operates optimally. [28]
Coulombic Efficiency (%)	The effectiveness of the battery in converting input energy during charging and delivering output energy during discharging. [25]
Self-Discharge Rate (%)	A battery's self-discharge rate is the rate at which it loses charge when not in use. This rate can reach 3-5 % per month for some types, meaning a new battery may hold only 95 % of its charge after a month.[29]

The ideal battery, a reliable energy storage solution, must meet eight key criteria: high specific energy, affordability, long lifespan, safety, wide temperature range, low toxicity, fast charging capability with low self-discharge, and minimal performance degradation. [30]

2.6 Classifications of Lithium-Ion Batteries

Table 2.3 compares three types of lithium-ion batteries: Lithium Cobalt Oxide (LCO), Lithium Manganese Oxide (LMO), and Lithium Nickel Manganese Cobalt Oxide (NMC), providing insights into their characteristics and performance [31]. These batteries are classified based on the materials used in their cathodes.

Table 2.3: Comparison of different types of lithium-ion batteries - part 1 [32]

	Lithium Cobalt Oxide (LCO)	**Lithium Manganese Oxide (LMO)**	**Lithium Nickel Manganese Cobalt Oxide (NMC)**
Advantages	High specific energy.	Lower resistance, improved current, and thermal stability.	High specific charge, economically feasible, low self-heating rates, and high charging voltage capability.
Drawbacks	Short lifespan, low thermal stability, and limited load capabilities, potentially causing overheating and safety issues.	Limited cycle and calendar life.	Nickel and cobalt mining dependence, thermal runaway
Voltages	3.0–4.2 V	3.0–4.2 V	3.0–4.2 V
Specific energy (capacity)	150–200 Wh/kg	100-150 Wh/kg	150–220 Wh/kg
Cycle life	500-1000	300–700	1000-2000
Thermal runaway	150°C	250°C	210°C

Table 2.4 compares Lithium Iron Phosphate (LFP), Lithium Nickel Cobalt Aluminum Oxide (NCA), and Lithium Titanate (LTO) batteries.

Table 2.4: Comparison of different types of lithium-ion batteries - part 2 [32]

	Lithium Iron Phosphate (LiFePO4) — LFP	**Lithium Nickel Cobalt Aluminum Oxide (LiNiCoAlO2) — NCA**	**Lithium Titanate (Li2TiO3) — LTO**
Advantages	High electrochemical performance, low resistance, high current rating, long cycle life, thermal stability, safety, and tolerance to abuse. [33]	High specific energy, good specific power, and long life span	Fast charging, high discharge current, and low-temperature discharge.
Drawbacks	Reduced energy density and poor low-temperature charging. [33]	Lacks safety and cost.	Expensive and low specific energy.
Voltages	2.5–3.65 V	3.0–4.2 V	1.8–2.85 V
Specific energy (capacity)	90-120 Wh/kg	200–260 Wh/kg	50-80 Wh/kg
Cycle life	> 2000	500	3000-7000
Thermal runaway	270ºC	150ºC	177 ºC [34]

In the thesis, $LiFePO_4$ cathodes were used, as LFP batteries are preferred for their high electrochemical performance, safety, and long cycle life. [33]

2.7 Electrolytes

An ideal solid electrolyte for batteries must exhibit several key characteristics to ensure effective and safe performance. It should have high ionic conductivity to promote ion movement while maintaining low electrical conductivity to prevent energy losses and short circuits. The electrolyte needs to be flexible enough to accommodate electrode volume changes during charge and discharge cycles. A wide electrochemical stability window is crucial for compatibility with high-voltage cathodes. Additionally, a high cation transference number is essential to avoid negative charge buildup near the anode and ensure uniform ion deposition, preventing dendrite formation. Mechanical strength is necessary to inhibit uncontrolled ion development, and optimal wettability with low interfacial resistance guarantees efficient contact and ion transfer with the electrodes. Finally, the electrolyte must have thermal stability to function safely across a range of temperatures and be easy to fabricate at a low cost to enable large-scale production and

accessibility. [4, 31]

Electrolytes are classified into liquids and solids, as presented in figure 2.7, each with advantages and drawbacks. [31]

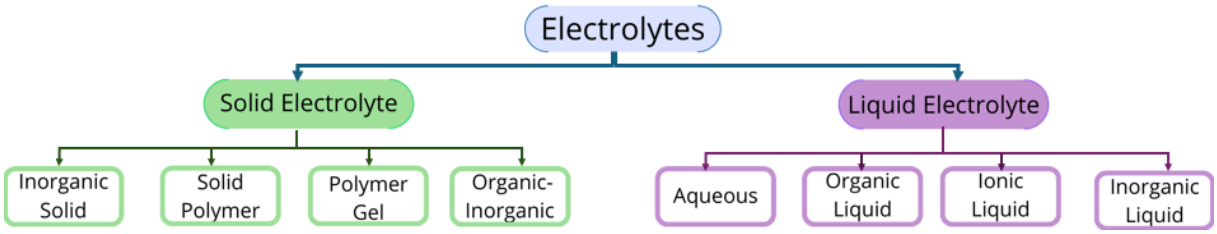

Figure 2.7: Type of electrolytes

In the next subchapter, these electrolytes will be thoroughly addressed.

2.8 Liquid electrolytes

Although liquid electrolytes have good interfacial contact and high ionic conductivity, they are prone to severe leakage problems and high reactivity. In liquid electrolytes, exothermic processes at the electrode surface quickly raise the energy storage medium's total temperature, causing electrolyte breakdown and the production of flammable gases— a phenomenon known as thermal runaway. This poses serious risks because it can cause device breakage, fire, smoke, and even explosions. Additionally, the formation of lithium dendrites during charge and discharge cycles is another major issue when using liquid electrolytes, potentially leading to short circuits and catastrophic battery failures. [31]

There are many different types of liquid electrolytes, including aqueous electrolytes, organic liquid electrolytes, ionic liquid electrolytes, and inorganic liquid electrolytes, each with its unique properties and applications. [31]

Aqueous electrolytes are electrolytes based on water solvents for the compounds that provide conducting ions after their dissociation. It is a cost-effective and efficient battery material due to its high ionic conductivity and ability to withstand high electrical currents without damage from oxygen cycling (during overcharging, oxygen produced at the positive electrode diffuses through the separators and can be reduced to water at the negative electrode). This allows for a longer service life and safer operation. Furthermore, aqueous electrolytes can be used in sealed, maintenance-free environments, simplifying charging equipment and lowering operational

expenses. However, these electrolytes have limits, such as a significant self-discharge rate for systems with voltages more than 1.23 V, which may limit their use in some situations. [35]

Ionic liquids (ILs) electrolytes are molten salts that remain liquid at or near room temperature, are made of organic/inorganic cations and anions, and do not require a solvent, as opposed to organic, inorganic, and aqueous liquids [36]. They are promising solutions for lithium-ion batteries due to their strong ionic conductivity, thermal stability, and non-flammability, which improve safety and electrochemical performance. Unfortunately, the cost issue is still a problem in considering commercial applications. [37]

To address these issues, particularly the risks of leakage, thermal runaway, and dendrite formation, this research project will focus on the study of solid electrolytes.

2.9 Solid electrolytes

Solid electrolytes are a promising alternative to liquid electrolytes due to their physical and chemical stability, ability to prevent unwanted structures, and superior electrochemical stability, making them suitable for high-energy-density lithium metal anodes and high-potential cathodes. [38, 39]

Moreover, solid electrolytes simplify mass production and battery assembly by enabling easy serial stacking, improving pack efficiency and volumetric energy density, and reducing battery management system complexity. Their higher thermal stability and thermal conductivity also mean less heat generation, eliminating the need for cooling systems and lowering accessory costs. [39]

Because solid electrolytes enable the use of lithium metal anodes, which have a far higher theoretical capacity than currently employed lithium-ion anodes, batteries with solid electrolytes have higher energy densities. Lithium metal and liquid electrolytes can react to produce an insulating layer on the anode surface that stops lithium ions from flowing. This may lower battery performance and ultimately cause a battery to fail. Conversely, solid electrolytes are typically more stable and less likely to react with lithium metal. [40]

To achieve high energy density in solid-state batteries (SSBs), the limit of the SPE thickness is around 20 μm. However, producing electrolytes with a thickness of less than 50 μm is tough due to technological and material limitations because reducing the thickness of electrolytes can

compromise their mechanical properties. Despite these difficulties, reaching a 20 μm is crucial for competing with liquid electrolyte batteries. The separators used in liquid batteries nowadays are 20 μm in size. For SSBs to match or surpass their energy density, the SE thickness needs to be lowered without sacrificing the battery's chemical stability and structural integrity. [41]

Solid electrolytes can be classified into four types: gel polymer electrolytes (GPE), solid polymer electrolytes (SPE), inorganic solid electrolytes (ISE) and organic and inorganic composite electrolytes (OICSE). [4]

2.9.1 Gel polymer electrolytes (GPE)

Gel polymer electrolytes (GPEs) are a type of polymer electrolyte that contains a small amount of liquid solvent within the polymer matrix to enhance ionic conductivity and material flexibility. This combination merges the properties of liquid and solid electrolytes, offering high ionic conductivity, good thermal stability, low flammability, and easy processing [42]. However, the poor mechanical strength of GPEs and the risk of solvent loss through evaporation can limit their widespread application. [43]

2.9.2 Solid polymer electrolytes (SPE)

Polymer electrolytes, consisting of long polymeric chains with high ion concentrations, provide improved safety, dendrite resistance, and excellent mechanical flexibility due to the polymeric backbone. They also exhibit high wettability, meaning the solid material adheres well and forms a uniform interface with the electrodes, along with a broad electrochemical stability window [4, 39]. These properties make solid polymer electrolytes (SPEs) particularly suitable for flexible and wearable electronics, such as flexible phones [31]. However, challenges persist in achieving the required ionic conductivity (in the range of 0.01–1 mS/cm at room temperature [44]).

In the field of solid polymer electrolytes (SPEs) for lithium-ion batteries, several innovative materials are being explored to improve ionic conductivity and electrochemical stability, as is shown in table 2.5.

Table 2.5: Categories of Polymer Electrolytes.

	Description	Example
Polyether-Based SPEs [45]	Offer leak resistance and flexibility. Challenges arise with low temperatures and increased crystallinity.	PEO
Polycarbonate-Based SPEs [45], [46]	Improved ionic conductivity, coordination structures, and high-voltage ambient-temperature applications. Complex preparation.	PEC, PPC, PTMC
Polysiloxane-Based SPEs [47]	Flexible backbone, low glass transition temperature, and superior electrochemical stability.	PDMS
Plastic Crystal-Based SPEs [45]	Combine liquid electrolyte ionic conductivity with solid mechanical stability. Enhanced plasticity and superior ionic conduction.	SN
Vinyl-based SPEs [31]	Hydrophilic polymers known for their affordability and flexibility.	PVA, PVC, PVP, PMMA
Fluoride-based SPEs [39]	High chemical and electrochemical stability, good mechanical properties, and low glass transition temperatures.	PVDF

The key components of SPEs include salts and polymer hosts with specific properties. In SPEs, the salt provides free ions for conduction, while the polymer offers mechanical stability by increasing the electrolyte's viscosity. The salts used in SPEs should have large anions and low dissociation energy, which facilitates easy dissociation and results in the presence of free mobile ions. The polymer host must exhibit fast segmental motion of the polymer chain and possess special functional groups that promote salt dissolution. Additionally, it should have a high molecular weight, a wide electrochemical window, and a high degradation temperature to ensure stability and efficient ionic conductivity. [48]

Achieving high conductivity while maintaining mechanical properties remains a significant challenge in salt-doped polymer blends. [49]

2.9.3 Inorganic Li-Ion Electrolytes

Inorganic lithium-ion electrolytes (ILCs) are a kind of inorganic solid materials that can conduct lithium ions, including oxides (Oxide-Type Li-Ion electrolytes), sulfides (Sulfide-Type Li-Ion electrolytes), chloride, and nitrides. [40]

ILCs allow for rapid ion transport while possessing non-flammability and non-corrosiveness [40]. However, they face significant challenges, including low wettability, harsh processing conditions, and high interface impedance, which hinder their widespread application. [39]

Oxide-type Li-Ion electrolytes include Perovskite-type solid electrolytes ($Li_{3x}La_{(2/3)x}TiO_3$), anti-perovskite electrolytes, NASICON-type electrolytes ($Na_{1+x}Zr_2P_{3x}Si_xO_{12}$), and garnet-type electrolytes ($Li_5La_3M_2O_{12}$), all of which exhibit significant ionic conductivities suitable for lithium-ion batteries. Perovskites offer high ionic mobility due to cation deficiency [50], anti-perovskites provide stability and high conductivity with chemical tunability [51], NASICONs benefit from structural enhancements [52], and garnets feature unique crystalline architectures promoting efficient lithium-ion conduction [53].

Sulfide-Type Li-Ion electrolytes are represented by Thio-LISICONs, including $Li_{4-x}M_{1-y}M'_yS_4$, which exhibit superior electrochemical performance compared to LISICONs, with a particular focus on $Li_{4-x}Ge_{1-x}P_xS_4$. Lithium Germanium Phosphorous Sulfide (LGPS) is known for its exceptional ion conductivity but faces challenges such as instability at interfaces and high production costs. Argyrodites, particularly Li_6PS_5X, are valued for their unique ion conductivity and cation mobility, with halides such as Cl, Br, and I further enhancing performance [45].

2.9.4 Organic and inorganic composite electrolytes (OICSE)

To enhance battery performance, organic-inorganic composite solid electrolytes (OICSEs) integrate polymer matrices with ionic conductive inorganic fillers, including ceramic fillers, ferroelectric ceramics, and clays. This hybrid approach offers superior safety, flexibility, and ionic conductivity compared to purely inorganic electrolytes. [45, 54]

To summarize this section, figure 2.8 highlights the key characteristics of the three main types of electrolytes: liquid, inorganic, and polymer.

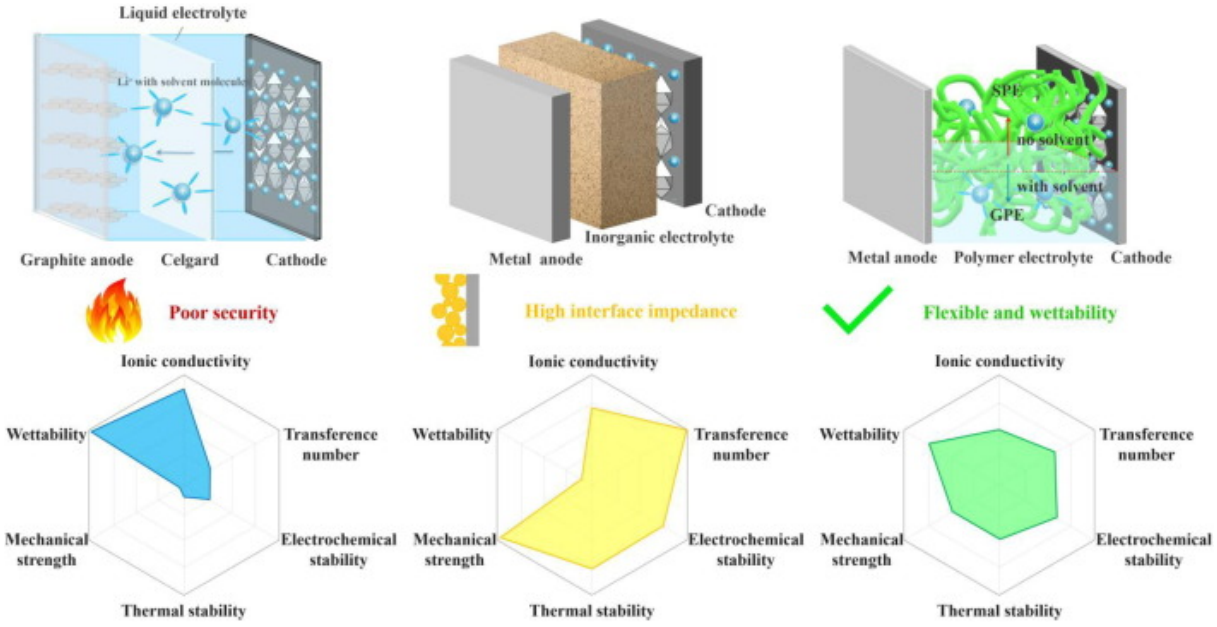

Figure 2.8: Characteristics of three common electrolytes in lithium batteries. [39]

2.10 Ion conduction in solid electrolytes

The efficient ionic conduction in solid electrolytes is crucial for the electrochemical performance of devices such as solid-state batteries, as it directly affects ion transfer, cycle life stability, and overall safety, making it a key factor in the advancement of energy storage technologies. [45]

2.10.1 Ion conduction in amorphous and crystalline phases

Solid polymer electrolytes primarily move ions within the amorphous phase, where polymer chains have greater mobility and structural disorder, while the crystalline phase organizes polymer chains rigidly, limiting ion movement. [45]

Local free volumes (also known as cavities or holes) with atomic and molecular dimensions are present in amorphous phases due to the molecular relaxing of polymer chains and terminal ends and uneven molecular packing. [49]

Ion transport in solid polymer electrolytes (SPEs) involves a combination of ion hopping and segmental motion of polymer chains, where a wave-like peristalsis creates temporary pathways that incessantly replace segments solvating lithium ions, enabling continuous ion migration. [55]

For ion hopping to occur, there must be mobile ions and vacant sites within the polymer

matrix for these ions to occupy. Effective conduction requires equivalent potential energies for these sites and low activation energy for ion movement, driven by thermal vibrations [31]. If the potential energy of a vacant site is significantly different from that of an occupied site, ions will encounter resistance, hindering conduction. [31]

In contrast, in the crystalline regions, ion conduction involves lithium ions migrating through vacancy diffusion within folded and stacked polymer chains, forming helical channels that facilitate ion hopping, though this process is slower compared to the amorphous phase. [56]

Scheme 2.9 illustrates the two primary mechanisms of ion transport in polymers.

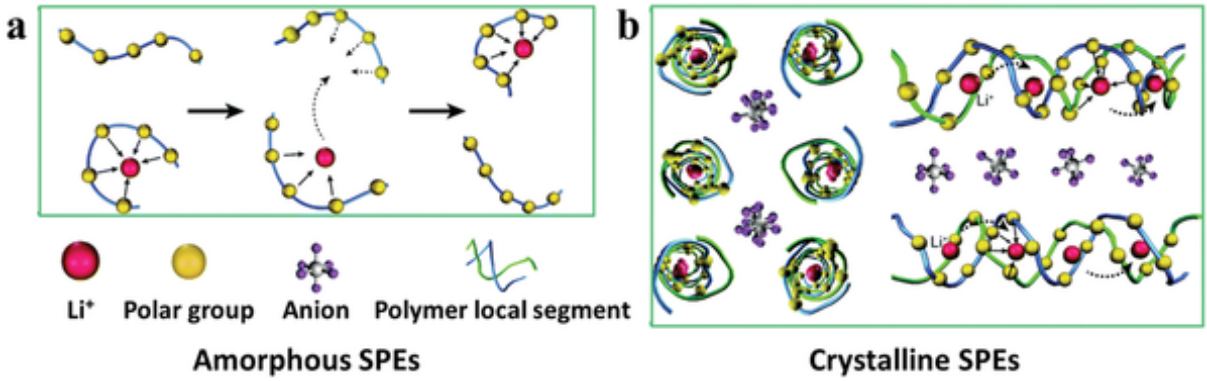

Figure 2.9: Schematic of Li ion transport pathways in two types of SPEs: a) typical amorphous SPEs; b) specific crystalline complex SPEs. [57]

Ratner et al. [58] investigated how lithium ions interact with polar groups in polymer chains. These polar groups solvate the lithium ions, creating a "shell" around them that facilitates their passage through the polymer. The quantity and stability of polar groups in the polymer chain directly affect its ability to solvate and transport lithium ions. The strength and efficiency of polymers also influence conductivity, with stronger, more flexible chains facilitating better ionic transport. [45]

2.10.2 Single ion conducting (SIC) and dual ion conducting (DIC)

Electrolytes for solid-state lithium-ion batteries are classified according to the movement of anions inside the electrolyte. There are two types of electrolytes: single ion conducting (SIC) and dual ion conducting (DIC). [59]

Because anions are immobilized, SIC electrolytes avoid concentration polarization and lithium-ion gradients. This results in more uniform ion migration, which reduces electrolyte leakage and

dendrite formation, thereby enhancing battery performance and safety. However, the formation of lithium dendrite is influenced by factors that go beyond the limitations of mass transport, such as the behavior of the interface and the homogeneity of the coating. On the other hand, current SIC electrolytes have limited ionic conductivity, poor electrochemical stability, and insufficient interface contact with electrodes, limiting their commercial applicability. [59]

In contrast, double-ion conduction (DIC) occurs when solid polymer electrolytes interact with mobile ions, resulting in mass transport limits known as concentration polarization [60]. Above the current limit, this causes unequal distribution of lithium ions across the electrolyte, raising ionic resistance and causing a potential difference, which limits charge transfer efficiency. However, the concentration polarization is generally not pronounced at moderate currents. DIC-based electrolytes have kinetic advantages over single-ion conduction (SIC) because of more efficient ion transport at moderate currents. [60]

The difference in cyclic voltammetry profiles between single and dual ion conduction arises from their ion transport mechanisms as presented in figure 2.10

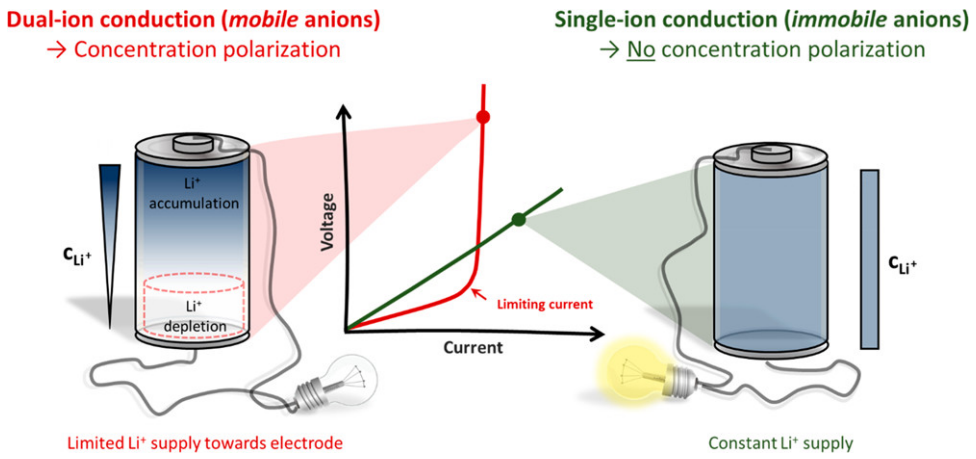

Figure 2.10: Cyclic Voltammogram for Dual-Ion Conduction and Single-Ion Conduction.Source: [60]

The limiting current in dual-ion conduction (DIC) systems marks the point where concentration polarization significantly impacts battery performance, causing a sharp increase in voltage due to Li^+ ion accumulation and depletion. This occurs because the transport of Li^+ ions cannot keep up with the applied current, leading to increased ionic resistance and reduced efficiency. [60]

2.10.3 Nernst-Einstein equation

The Nernst-Einstein equation (equation 2.3) links ionic conductivity to ion diffusion, influenced by concentration and charge, where n_i and q_i are the concentration and charge of the free ions, respectively, and k_BT is the thermal energy, where k_B is the Boltzmann constant and T is the temperature. [61]

$$\sigma = \frac{1}{K_BT} \sum n_i q i^2 D_i \tag{2.3}$$

In polymer–salt complexes, ion movement is hindered by the large polymer chains and crystalline domains. Ionic conductivity depends on the number of ions and the mobility of the polymer chain. [55]

Charge density (η) is influenced by the polymer's dielectric constant (ε) and dissociation energy (U), as described by equation 2.4: [55]

$$\eta = \eta_0 \exp\left(\frac{-U}{\varepsilon k_B T}\right) \tag{2.4}$$

An increase in the dielectric constant (ε) leads to a higher charge carrier concentration because ε is directly related to the capacitance and stored charge, thereby improving ionic conductivity by increasing the number and migration speed of movable ions. [55]

2.10.4 Arrhenius Model

The Arrhenius is essential for understanding the impact of temperature on ionic conductivity in solid polymer electrolytes (SPEs).

The Arrhenius behavior describes how the ionic conductivity (σ) of solid polymer electrolytes varies with temperature, according to equation 2.5: [62]

$$\sigma(T) = \sigma_0 e^{-\frac{E_a}{k_B T}} \tag{2.5}$$

Where $\sigma(T)$ is the conductivity at temperature T, σ_0 is the pre-exponential factor, E_a is the activation energy and k_B is the Boltzmann constant.

In this behavior, the conductivity increases exponentially with temperature as ion mobility is

enhanced by thermal energy. This is because higher temperatures provide more thermal energy, which helps overcome the energy barriers for ion movement, facilitating ion hopping and thus increasing conductivity. Therefore, there is a linear relationship between $\ln(\sigma)$ and $\frac{1000}{T}$. The activation energy (E_a) can be determined from the slope of this line, which represents $-\frac{E_a}{k_B}$ and measures the minimum energy required for ions to move through the material, with lower values indicating easier movement and higher ionic conductivity. [62]

2.11 Key components of SPEs: salts and polymer hosts

This section details the specific salt, polymers, and compounds used in this study.

2.11.1 Lithium perchlorate ($LiClO_4$) as a conductive salt

$LiClO_4$ is a well-known salt used as an electrolyte in lithium-ion batteries due to its low lattice energy (723 kJ/mol [63]). Compared to other lithium-based salts, $LiClO_4$ is less expensive and contains no fluorine, reducing the corrosiveness, toxicity, and environmental impact of salt. It exhibits strong conductivity, great anodic stability, and low hygroscopicity, making it stable under normal moisture conditions. These distinct qualities make $LiClO_4$ an excellent component in polymer/$LiClO_4$ composites, enhancing their utility, particularly in battery technology. [49]

2.11.2 Polyvinylidene fluoride (PVDF) as polymer matrix

PVDF electrolytes, which were first created in the 1980s, were chosen for their superior qualities in lithium battery applications. Throughout the twentieth century, research on PVDF-based electrolytes, particularly gel forms, expanded, with inert inorganic additives and polymer blends used for modification. [39]

Poly(vinylidene fluoride) (PVDF) is considered promising due to several key properties. Firstly, it exhibits exceptional mechanical strength and toughness, which enhances its durability and reliability in various applications. Additionally, PVDF offers a wide voltage window, making it suitable for a range of electrochemical devices. It also demonstrates impressive thermal stability, operating effectively at long-term temperatures up to 150°C and having a decomposition temperature as high as 400°C [39]. Furthermore, PVDF possesses strong electrochemical stability, ensuring consistent performance over time. Another advantage is its high relative permittivity,

which refers to its ability to store electrical energy in an electric field. This high permittivity reduces ion-ion interactions, facilitating easier dissociation of lithium ions as the polarized portions of the polymer stabilize the ions [39].

The limitations of PVDF (polyvinylidene fluoride) as a polymer electrolyte are its low ionic conductivity, high crystallinity and lack of reactive groups. [39]

This semi-crystalline polymer exhibits five distinct crystalline phases, with the most studied being the α, β, and γ phases.[64]

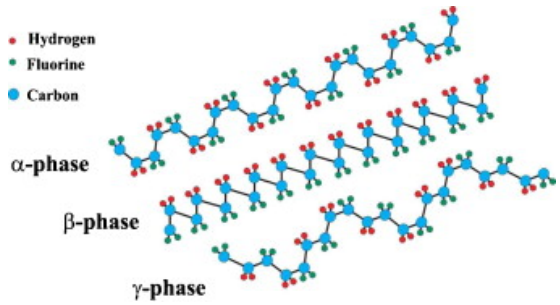

Figure 2.11: Diagram showing the chain conformation for PVDF's α, β, and γ phases. [64]

FTIR results quantify the β-phase content in PVDF using the Lambert-Beer law. The relative β-phase content, $F(\beta)$, is calculated from absorbance values at 766 cm^{-1} and 840 cm^{-1} with absorption coefficients $K_\alpha = 6.1 \times 10^4\, cm^2 mol^{-1}$ and $K_\beta = 7.7 \times 10^4\, cm^2 mol^{-1}$. [64]

$$F(\beta) = \frac{A_\beta}{(K_\beta/K_\alpha)A_\alpha + A_\beta} \tag{2.6}$$

Achieving the β phase is particularly crucial due to its superior dipole alignment within PVDF chains, resulting in enhanced mechanical flexibility and electrolyte stability [65]. Additionally, the β phase exhibits superior dielectric properties compared to the α phase. These properties lead to improved charge storage capabilities, accelerated ion dissociation, reduced ion aggregation, and an overall increase in charge carriers. [66]

PVDF, with its high anodic stability and dielectric constant, can be used to ionize lithium salts, resulting in high-quality functional polymer electrolytes. Increasing $LiClO_4$ increases the average pore size, as Khushbu Gohel et al. [67] examine the impact of salt on PVDF membranes, emphasizing its role in increasing pore size, which contributes to enhanced ionic conductivity through the disruption of PVDF's crystallinity caused by the interaction between Li^+ ions and fluorine.

According to Shen et. al [68], the conductivity of PVDF with $LiClO_4$ ranges from 10^{-6} S/cm to 10^{-4} S/cm, depending on the percentage of $LiClO_4$.

2.11.3 Polyvinyl Alcohol (PVA) as a polymer matrix

PVA is a synthetic biopolymer produced by the hydrolysis of polyvinyl acetate. It is recognized for its semi-crystalline nature, biocompatibility, non-toxic characteristics, eco-friendliness, high solubility, affordability, excellent film-forming capacity, outstanding elongation, and heat stability [31]. Despite these advantages, PVA's hydrophilic nature poses a disadvantage for battery electrolytes, as it can absorb moisture and is affected by any aqueous solution. [31]

PVA's chemical structure consists of a carbon backbone with hydroxyl (OH) side chains, represented by the chemical formula $[CH_2CH(OH)]_n$. The physicochemical properties of PVA are significantly influenced by its molecular weight and the degree of hydrolysis [31, 69]. The molecular weight of PVA ranges from 20,000 to 400,000, depending on the initial vinyl acetate polymer length and the extent of hydrolysis, which, whether complete or partial, occurs under alkaline or acidic conditions and removes acetate groups, greatly impacting PVA's characteristics [31].

One of the most notable features of PVA is its exceptional performance as an oxygen barrier, surpassing any other known polymer. This property can enhance battery performance by preventing the oxidation of sensitive components, increasing electrolyte stability, and improving battery safety [31]. However, PVA's stability over long cycles can be a challenge, potentially leading to membrane cracking and capacity loss. To address this, PVA is often combined with other materials like salts (e.g. potassium iodide (KI), potassium chloride (KCl), sodium chloride (NaCl) [70] and $LiClO_4$ [71]) and plasticizers (e.g. glycerol [72]) to improve stability [55].

PVA's predominantly amorphous nature enhances ionic conductivity by providing greater polymer chain mobility and increased free volume for ion transport. Additionally, its low reactivity with lithium-metal anodes enhances electrode-electrolyte interfacial stability [55]. The polymer's polar groups, such as —OH, effectively dissolve the conducting salt and form electrostatic (Coulombic) interactions with the ions, aiding in salt dissociation and stabilizing the ions within the polymer matrix. This coupling ensures that the dissociated ions remain mobile and do not recombine quickly, enhancing the ionic conductivity of the SPE [55].

The addition of salt to PVA enhances the amorphous region and free volume, promoting local

polymer chain segmental motion and ion migration. This increases conductivity by facilitating greater ion mobility and hydrogen bond formation with PVA chains [55]. The temperature-conductivity relationship for PVA-based electrolytes with different salt amounts follows the Arrhenius model, with conductivity increasing linearly with temperature [55].

According to Gunawan et al. [71], the conductivity of PVA with $LiClO_4$ ranges from 10^{-5} S/cm to 10^{-4} S/cm, depending on the percentage of $LiClO_4$.

Comparing PVA and PVDF, the two polymers used in this study, PVA exhibits a higher elongation at break (220.7 %) compared to PVDF (22.5 %) [73]. Although PVA has slightly lower tensile strength (48.4 MPa) and a significantly lower Young's modulus (707.9 MPa) compared to PVDF (53.5 MPa and 2450 MPa, respectively) [74]. It also exhibits a higher melting temperature (185°C) compared to PVDF (172°C) and a lower decomposition temperature (240°C) compared to PVDF (400°C) [75].

2.11.4 PVA / Sodium Alginate (NaAlg) as polymer matrix

PVA is being blended with Sodium Alginate (NaAlg), a seaweed polysaccharide, to improve its mechanical properties and expand its applications. [49]

Adding NaAlg to PVA offers several advantages. This blend forms a composite matrix with high miscibility and improved mechanical strength, due to significant interactions between the hydroxyl groups of PVA and the carbonyl groups of NaAlg via inter-chain hydrogen bonding. Furthermore, sodium alginate decreases the crystallinity of PVA by breaking its crystalline structure through these hydrogen bonds, which increases the polymer's flexibility and amorphous regions. Consequently, the reduced crystallinity and the presence of flexible polymer chains facilitate achieving high ionic conductivity. [49]

The addition of $LiClO_4$ to the PVA / NaAlg composite causes an increase in crystallinity due to the interaction of Li^+ ions with the polymer chains, forming hydrogen bonds. These interactions result in tighter packing of the polymer chains, leading to a more regular organization and higher crystallinity. As the concentration of $LiClO_4$ increases, the intensity of these interactions also increases, promoting a greater amount of crystalline regions in the material. [49]

2.11.5 $Li_{2.99}Ba_{0.005}ClO$ as amorphous glass ferroelectric electrolyte

The precursor of LiBa ($Li_{2.99}Ba_{0.005}ClO$) is Li_3OCl, an inorganic substance from the family of lithium-rich antiperovskites. Li_3OCl has an antiperovskite structure with chlorine (Cl^-) at the center of the cube, oxygen (O^{2-}) at the core of the octahedron, and lithium (Li^+) at the octahedron's vertices, resulting in a lithium-rich structure. [76]

Doping with additional elements is one of the most effective ways to improve the properties of inorganic materials. Braga et al. [76] did a study in which they doped Li_3OCl with several elements and found that the most effective doping was accomplished with barium, resulting in the composition $Li_{2.99}Ba_{0.005}ClO$, also known as LiBa. Doping boosted ionic conductivity due to the high radius of the Ba^2+ ion, resulting in more lattice anisotropy and improved lithium-ion mobility [76]. Furthermore, the water-based synthesis proposed by the author results in an amorphous glass electrolyte, that is usually associated with high ionic conductivity because their open structures facilitate the ionic hoping process. During electrochemical impedance spectroscopy and cyclic voltammetry [76], it was observed that LiBa also had ferroelectric characteristics, such as negative capacitance and spontaneous polarization. [76, 77]

Ferroelectric materials are dielectric materials with spontaneous electrical polarization that can be changed without an external electric field [78]. When used as solid electrolytes in batteries, these materials enhance ion mobility through internal polarization effects created by the orientation of permanent dipoles within the material. This polarization effect reduces internal resistance, increases ionic conductivity, stabilizes charge-discharge cycles, reduces hysteresis, and enhances electrochemical performance. [76]

Thus, LiBa can be characterized as an amorphous glass ferroelectric electrolyte with intriguing properties for usage in solid-state batteries. [76]

LiBa exhibits an extremely high dielectric constant, from 10^9 at 25 °C to 10^{10} at 220 °C, and high ionic conductivity of 25 mS cm^{-1} at 25°C. It remains stable in cyclic voltammetry within a voltage range of -10 to +10 V. [76]

This page is intentionally left blank.

Chapter 3

Experimental Techniques

An overview of the materials and experimental techniques is given in this chapter. Solid electrolyte synthesized methods are covered after the reaction materials. The characterization methods are then described in more detail.

3.1 Reaction materials

Polymers

- $(C_2H_4O)_x$, Polyvinyl Alcohol - PVA -, M.W= 3000-88000 g/mol (KURARAY POVAL ^{TM})
- $(CH_2CF_2)_n$, Polyvinylidene fluoride - PVDF - Nanopowder, 99,9 %, M.W= 600000 g/mol (TOB: XIAMEN TOB NEW ENERGY TECHNOLOGY CO.)
- $NaC_6H_7O_6$, Sodium alginate, NaAlg, MW = 12000 g/mol to 40000 g/mol, (Sigma-Aldrich)
- $C_6H_{10}O_5$, Cellulose

Salts

- $LiClO_4$, Lithium perchlorate (thermo scientific, 98%)
- LiCl (Sigma-Aldrich, >99% pure)
- LiOH (Sigma-Aldrich, 98% pure)
- $Ba(OH)_2$ (Sigma-Aldrich, 95% pure)
- NaCl (Merck, 99.9% pure)

- NaOH (Merck, >99.9% pure)

Solvents

- C_3H_7NO, N,N-Dimethylformamide, DMF, (thermo scientific, 99.5%)
- H_2O, Destiled water

3.2 Methods

3.2.1 Drop cast

A solution containing the required electrolyte components is deposited onto a substrate, allowing the solvent to evaporate (figure 3.1). A concentrated combination of electrolyte ingredients is left behind, and it eventually solidifies to create a thin coating on the substrate surface. Despite controlling the volume of solution applied to the substrate, it is difficult to ensure that the membrane forms homogeneously and with the desired thickness, as we do not have full control over the distribution of the solution. This procedure was conducted as a preliminary test to assess the coating formation. [79]

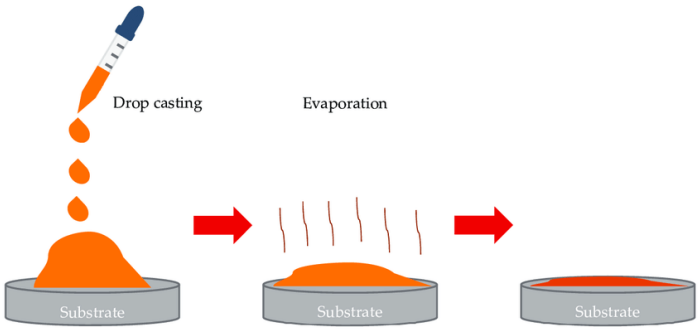

Figure 3.1: Drop cast method [79]

3.2.2 Doctor Blade

Doctor Blade is a method usually applied to produce thin sheets. It involves continuous relative movement between the blade and substrate. A well-mixed coating solution is placed on the substrate, and when the spreader moves with a set velocity and gap, the paste spreads over the substrate, creating a film (figure 3.2). Doctor Blade velocity and the coating solution's viscoelastic properties are crucial in determining the final film's thickness uniformity and homogeneity. After

this, the resulting film is dried at ambient temperature.[80]

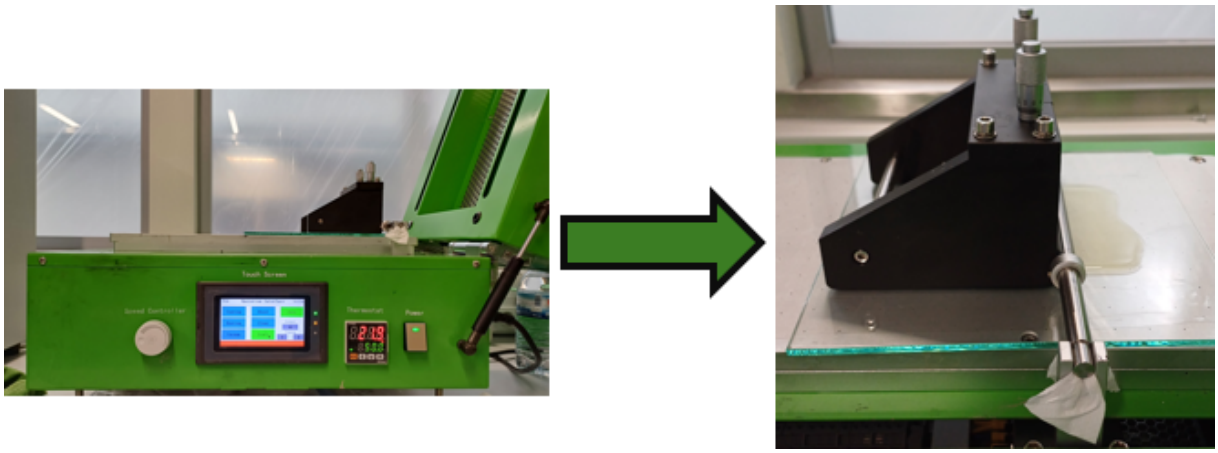

Figure 3.2: Doctor blade apparatus where the spreading speed of the solution can be adjusted (left) and electrolyte solution to be spread (right)

The Doctor blade technique was performed with the equipment from TOB XIAMEN TOB NEW ENERGY TECHNOLOGY CO., LTD

3.2.3 Non-solvent induced phase separation (NIPS)

The polymer solution obtained is first applied on a clean glass substrate and uniformly spread using the Mayer Bar, with a specific gap on top of the substrate to obtain a thin film. The phase separation process is then triggered by submerging the assembled product in a container filled with ultrapure water at a temperature of 75 °C. Using this technique, the difference in polarity between DMF and water disrupts the molecular interactions, forcing the membrane to crystallize and separate instantly from the glass substrate. The membranes are then allowed to air dry for a full day at room temperature. [81]

Figure 3.3 presents an overview of the NIPS process, illustrating the key steps from polymer dissolution to membrane drying.

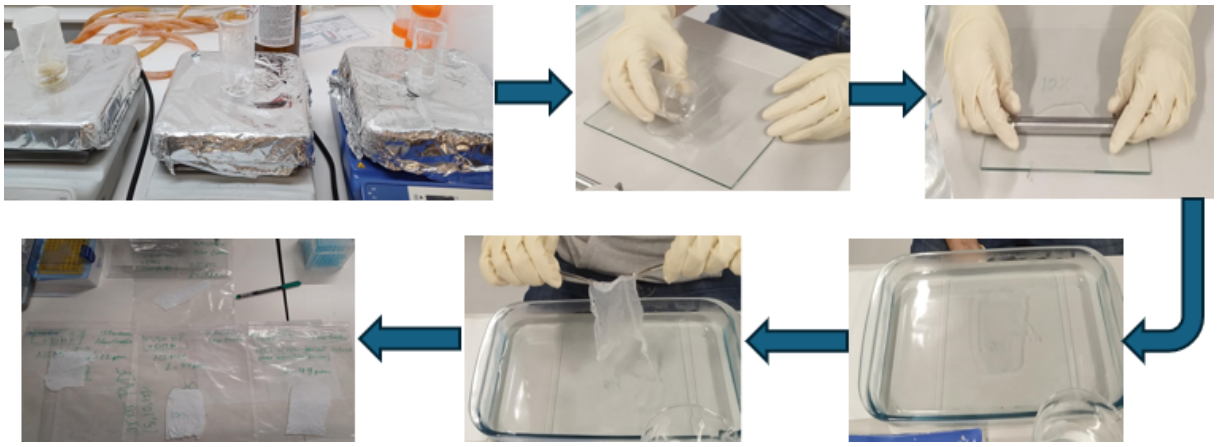

Figure 3.3: Non-solvent induced phase separation (NIPS) process: (a) polymer dissolution, (b) solution spreading, (c) Dispensing solution on substrate with Mayer bar, (d) immersion in the coagulation bath, (e) phase inversion and (f) membrane drying.

If the membranes were dried at room temperature without undergoing the separation process, the resulting solid electrolyte would exhibit porosity greater than the ideal. With this method, the expected pore size is around 1 μm, which is desirable for solid electrolytes applied to batteries. [81]

3.3 Synthesized electrolytes

3.3.1 $Li_{2.99}Ba_{0.005}ClO$ electrolyte

$Li_{2.99}Ba_{0.005}ClO$ glass electrolyte was synthesized from LiCl, LiOH, and $Ba(OH)_2$. After drying between 230 and 250 °C, the material was ground for 40 minutes at 300 rpm. The $Li_{2.99}Ba_{0.005}ClO$ powder was mixed with absolute ethanol and applied to a cellulose sheet, which was added to enhance the mechanical stability of the electrolyte.

3.3.2 PVDF / $LiClO_4$ electrolyte

PVDF / $LiClO_4$ electrolyte was prepared using two methods: the Doctor Blade and the NIPS technique.

DMF was added to beakers with different masses of PVDF, to make up different concentrations of polymer in solution. The beakers were agitated on separate plates at a temperature of 25ºC and a stirring speed of 120 rpm for a duration of 4 hours to thoroughly dissolve the PVDF.

After full dissolution, homogeneous and transparent solutions were obtained. After this step, different amounts of $LiClO_4$ (5%, 10% and 20%) were added to three PVDF solutions in DMF and dissolved for 3 hours at 25ºC and 120 rpm to fully homogenise the salt in the polymeric mixture. The solution was distributed over a glass substrate with a leveling bar adjusted to a thickness of 200 μm.

From this step, the two techniques diverge. Using the Doctor Blade method, the film is simply dried at room temperature. In contrast, with the NIPS technique, the membranes are removed from the glass substrate by immersing them in water at 75ºC. Finally, these membranes are dried at room temperature for 24 hours.

According to the study of Teixeira et Al. [81], the membranes produced at $T_{dissolution} = 25°C$ exhibited an average pore size closest to the ideal, lower porosity, and greater rigidity. This makes the NIPS technique at $T_{dissolution} = 25°C$ a promising option for PVDF membrane production, especially when compared to membranes produced at higher temperatures ranging from 25°C to 100°C.

3.3.3 PVA / NaAlg / $LiClO_4$ electrolyte

The PVA / NaAlg / $LiClO_4$ electrolyte contains 4% of total polymer (i.e., PVA / NaAlg), with different ratios in the relation PVA / NaAlg being applied (60% PVA / 40% NaAlg and 40% PVA / 60% NaAlg).

Initially, PVA was mixed with NaAlg in water at 60ºC and 120 rpm for 4 hours. After achieving a homogeneous mixture, $LiClO_4$ was added to the solution at concentrations of 5%, 10%, and 20%, and the solution was agitated for an additional 3 hours at 25ºC. Following this, the solution was processed using two techniques: Drop Casting and Doctor Blade.

The decision to use both Drop Casting and Doctor Blade procedures was made strategically to compare how different application techniques effect coating development. Drop Casting was initially used to evaluate the coating process and discover difficulties with uniformity and thickness. Based on these findings, the Doctor Blade approach was used to enhance the process, allowing for more exact control over coating thickness and consistency.

3.4 Coin cell assembly

The initial step in assembling the coin cell is to apply pressure between the electrolyte and the lithium iron phosphate ($LiFePO_4$ or LFP) cathode to enhance adhesion. This is done using a device that applies 25 bar of pressure at a temperature of 50°C. After this, the components are placed in an argon-filled glove box along with other necessary materials. Inside the glove box, the coin cell is assembled according to the configurations represented in figure 3.4. The left figure shows a coin cell with only the SPE, while the right figure includes the SPE combined with $Li_{2.99}Ba_{0.005}ClO$ electrolyte. Finally, the cell is sealed under a vacuum pressure of 6×10^{-1} torr to ensure a secure and airtight assembly.

Figure 3.4: On the left: Coin cell using SPE. On the right: Coin cell using SPE and amorphous glass ferroelectric electrolyte ($Li_{2.99}Ba_{0.005}ClO$).

The spacer in a coin cell fills the gap to securely hold all components in place, ensuring proper contact between the electrodes and the separator, which maintains consistent electrical performance and prevents short circuits. Additionally, it functions as a current collector. [82]

The spring protects the internal components from being crushed when the battery is squeezed together. If springs were placed on both electrodes, the cell may not shut properly, exposing the electrolyte to air and causing the experiment to fail. [83]

3.4.1 LFP as cathode

Lithium iron phosphate (LFP) is a promising cathode for lithium-ion batteries due to its safety, sustainability, and longevity. The ideal potentials are 4.12 V for charging and 2.80 V for discharging. Humidity also significantly impacts the electrochemical behavior of LFP. [84]

The theoretical capacity of the commercial LFP used to assemble the coin cell is 135 mAh/g with an active material mass loading of 93.4%. The specific capacity calculation for the coin cell must consider the ratio of the areas of the lithium metal (anode) to the LFP, as the lithium has a smaller area. Therefore, the coefficient $\left(\frac{8}{10}\right)^2 = 0.64$ is used in the calculation. The resulting specific capacity is given by $135 \times 0.934 \times 0.64$, which equals approximately 80.52 mAh/g. This adjustment ensures that the specific capacity is correctly calculated based on the diameter of the lithium. [85]

3.4.2 Lithium metallic as anode

Metallic lithium is an ideal anode material for batteries due to its high energy density compared to other anode materials. However, metallic lithium oxidizes very easily, necessitating careful preparation to avoid contact with any spacers or environments that could cause oxidation. Therefore, it should always be handled in an argon-filled glove box to prevent oxidation. [86]

3.5 Characterisation Techniques

3.5.1 Fourier Transform Infrared Spectroscopy

A Fourier transform spectrophotometer is an instrument that can determine a compound's absorption spectrum more quickly and non-destructively than other spectrophotometers. It employs an infrared beam from a black-body source that is channeled through an interferometer to generate both constructive and destructive interference. The beam then passes through the sample, where certain energy frequencies are absorbed. The detector evaluates the interferogram signal in terms of energy against time at all frequencies. To obtain the spectrum, the background is subtracted from the sample spectrum using Fourier transformation software. [87]

The mid-IR range of 4000 to 666 cm^{-1} is the analysis region for infrared spectra in FTIR spectroscopy. This region's absorption bands show which functional groups are present in particular compounds. Separate wavenumber ranges are used to detect different types of bonds, such as single, double, and triple bonds: 2500–4000 cm^{-1} for single bonds, 2000–2500 cm^{-1} for triple bonds, and 1500–2000 cm^{-1} for double bonds. Whole molecule vibrations, measured at lower wavenumbers (650–1500 cm^{-1}), add to a complicated pattern that is utilized in identification. [88]

Figure 3.5 illustrates the mid-infrared spectrum.

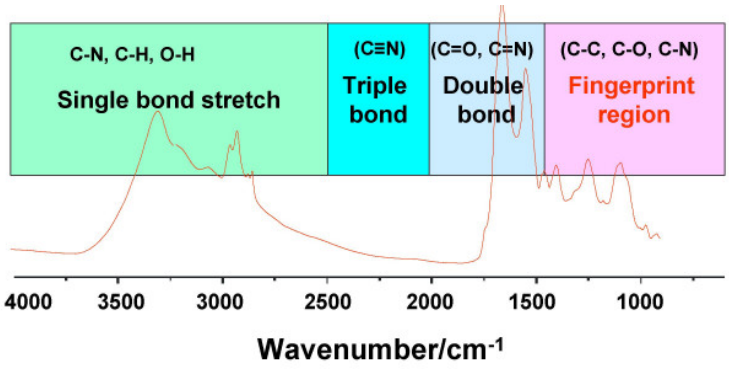

Figure 3.5: Mid-infrared representative spectrum. The fingerprint region is the region below 1500 cm^{-1}. The functional group region is above 1500 cm^{-1}. Source: [87]

To enhance the signal-to-noise ratio of the spectra, 16 scans were performed on each sample. Additionally, the spectrum's resolution was set to 4 cm^{-1} to ensure sufficient accuracy in identifying spectral peaks.

For analysis, acquiring high-quality spectra requires the use of sample handling procedures. Attenuated total reflection (ATR), diffuse reflectance, transmission, and genuine specular reflectance/reflection absorption are the four primary methods. [88]

ATR-FTIR spectroscopy detects changes in an internally reflected infrared beam interacting with a material. The spectrum is produced as the sample absorbs the evanescent wave from internal reflections [88]. This technique allows the identification of crystalline phases within the PVDF membranes through the analysis of their FTIR-ATR spectra.

The FTIR analysis was conducted using a Perkin Elmer Spectrum 100.

3.5.2 Determining the porosity of the membrane using n-butanol

To determine the porosity of the PVDF separator using n-butanol, first weigh the dry membrane before immersing it in an n-butanol solution for 150 minutes. Every 30 minutes, the wet membrane is weighed to track changes. The membrane's porosity (% by volume) is computed using the equation 3.1: [89, 90]

$$P(\%) = \left(\frac{\frac{m_{\mathrm{BuOH}}}{\rho_{\mathrm{BuOH}}}}{\frac{m_{\mathrm{BuOH}}}{\rho_{\mathrm{BuOH}}} / \frac{m_{\mathrm{P}}}{\rho_{\mathrm{P}}}} \right) \times 100 \tag{3.1}$$

m_p and m_{BuOH} represent the mass dry and mass wet membranes with butanol mass, ρ_p is the density of the membrane, and ρ_{BuOH} is the density of the butanol. [89, 90]

3.5.3 Mechanical test

Mechanical testing is an important stage in determining the physical characteristics of polymer membranes, with particular emphasis on tensile strength, Young's modulus, and elongation. These qualities give insight into the material's performance when stressed. [91]

Tensile strength indicates a material's durability, Young's modulus quantifies its stiffness, and elongation at break measures its ductility, all providing insights into the material's mechanical properties. [91]

Tensile testing of the SPE membrane will be performed with an applied tension of 100 N and a strain rate of 20 mm/s. The testing will be carried out in two directions: along the machine direction, which means, the Doctor Blade direction (DB direction) used for membrane manufacturing and in the transverse direction (DO direction).

Tests in both longitudinal and transverse directions are crucial for understanding a material's mechanical properties. The doctor blade technique aligns polymer chains in specific directions, resulting in anisotropic properties. This approach assesses uniformity and robustness of membrane performance, identifying weaknesses due to directional dependencies, thereby evaluating its suitability for various applications.

Mechanical testing was carried out with a Shimadzu instrument (figure 3.6).

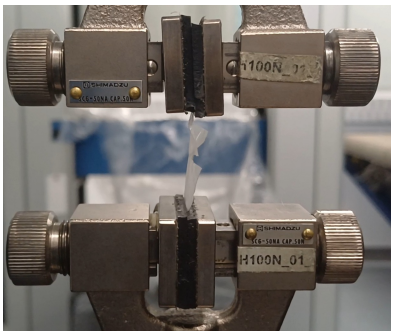

Figure 3.6: Mechanical testing machine

3.5.4 Laser Induced Breakdown Spectroscopy (LIBS)

LIBS is an analytical method for determining the elemental makeup of materials. It includes ablation of the sample's surface with a high-focused laser, resulting in a plasma of electronically excited atoms and ions. As these atoms decay to their ground states, they produce light with particular wavelengths specific to each element. This emitted light is collected, separated into component wavelengths by a diffraction grating, and examined using a spectrometer. The resultant spectral data is processed by a central processing unit (CPU) to provide a comprehensive elemental composition of the sample. [92]

LIBS measurements were performed using a SciAps Z-903 GEOChem Li.

3.6 Electrochemical Analysis

This section discusses various electrochemical tests performed on the Swagelok cell and the coin cell, which contain the electrolytes developed in this thesis. The tests include cyclic voltammetry, electrochemical impedance spectroscopy, chronoamperometry, and galvanostatic charge and discharge. Electrochemical experiments were performed using two distinct potentiostats. Initially, measurements were taken in Swagelok cells with steel electrodes (steel/SPE/steel), constituting a symmetric cell (right figure 3.7), and its electrochemical behavior was measured at Centi using the Autolab PGSTAT302N. Furthermore, these tests, conducted with gold electrodes (gold/SPE/gold) fabricated at MatER Lab (left figure 3.7), were performed using the Gamry 3000 potentiostat, which was also employed for electrochemical studies on coin cells produced at MatER Lab.

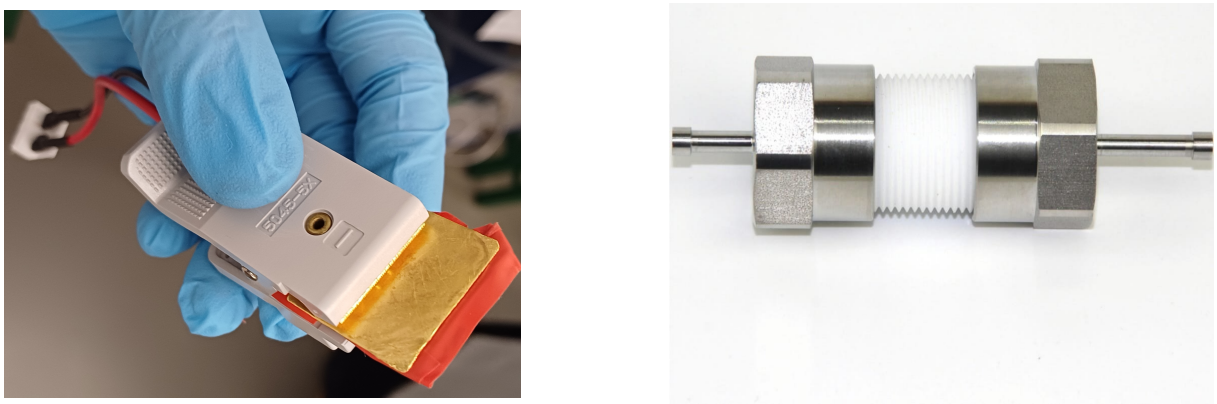

Figure 3.7: On the left: gold electrodes (gold/SPE/gold). On the right: Swagelok cell with steel electrodes. [93]

3.6.1 Electrochemical Impedance Spectroscopy

Electrochemical impedance spectroscopy (EIS) is a technique used to measure impedance (Z) for various frequency values. It is typically performed using a frequency response analyzer (FRA) and an electrochemical interface, which applies a constant voltage or current. The response is measured in potentiostatic mode, where a voltage is applied at each frequency, resulting in a different phase response. [94]

This relationship between voltage, current, and phase can be expressed mathematically by the equation 3.2

$$Z = \frac{V_0 e^{j\phi_V}}{I_0 e^{j\phi_I}} = Z_0 e^{j(\phi_V - \phi_I)} = Z_0(\cos(\phi) + j\sin(\phi)) = Z' + jZ'' \tag{3.2}$$

where ϕ represents the phase difference between the potential and the current.

Nyquist plots are created using data, with $-Z''$ plotted on the y-axis and Z' plotted on the x-axis. Examples of these plots are shown in Fig. 3.8

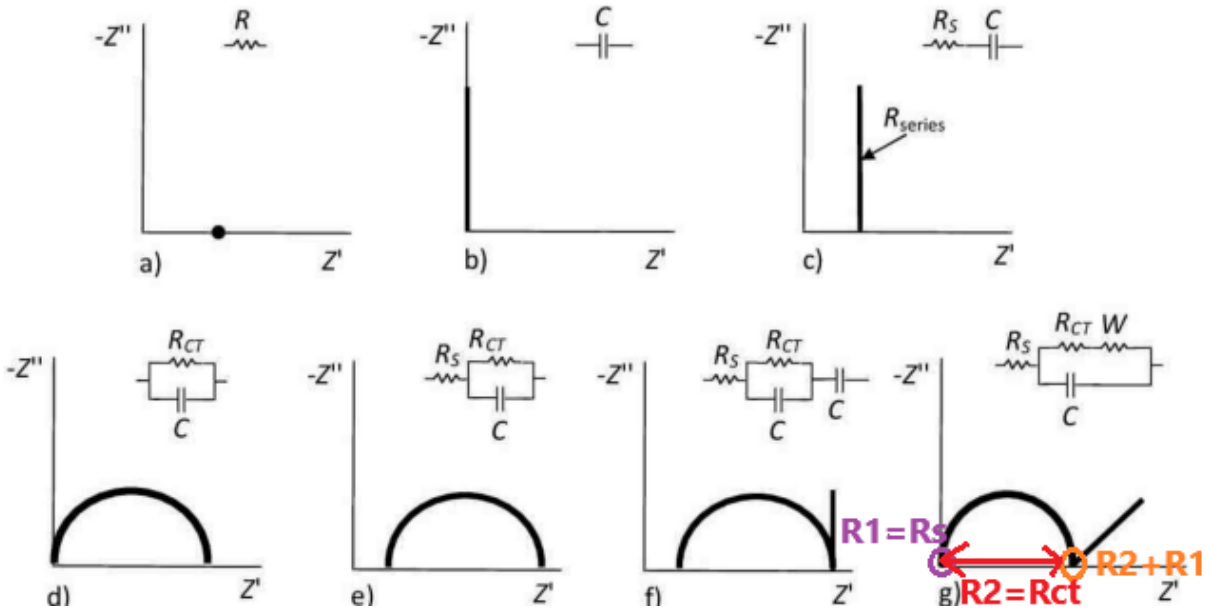

Figure 3.8: Nyquist graphs for various electrical circuits. a) Pure resistance R (only real part of the impedance); b) Pure capacitor C (only imaginary part of the impedance); c) R and C in series; d) R and C in parallel; e) R and C in parallel connected in series with a resistance (there is a shift to the right in relation to graph d) due to this series resistance); f) The same circuit as in e) but with a capacitor in extra series. g) Randles-Ershler circuit, with R_1 and R_2 being highlighted in this EIS graph.[94, 95]

The Nyquist graph is essential for calculating electrolyte ionic conductivity σ from the following formula: [96]

$$\sigma = \frac{l}{R_b A} \tag{3.3}$$

Where l is the thickness of the film measured using a screw micrometer, R_b is the volumetric resistance of the film obtained from the Nyquist plot, and A is the contact area of the film. [96]

In the impedance spectrum, R_{sol}, also known as R_{s}, corresponds to R_1, which is the solution resistance, and R_{ct}, also known as R_p, corresponds to R_2, which is the charge transfer resistance. To test whether it is R_1 or R_2 that represents the resistance of SPE, tests were carried out using gold electrodes (gold/SPE/gold). This setup guarantees that $R_1 = 0$, making R_2 reflects the resistance of the electrolyte, with measurements conducted using the Gamry 3000 potentiometer. Another way to confirm if R_2 is the appropriate resistance for determining the ionic conductivity of our SPE is by evaluating its variation with temperature. If R_2 remains constant with temperature, it indicates the mobility of ClO_4^- anions, suggesting double ion conduction. Conversely, if R_2 changes with temperature, it confirms that R_2 is associated with the SPE resistance and that the ClO_4^- anions are immobile, indicating single ion conduction.

In EIS, the frequency range was from 0.1 Hz to 1 MHz on the Autolab PGSTAT302N potentiostat and from 0.1 Hz to 7 MHz on the Gamry 3000 potentiostat.

During discharge, Li^+ transport and diffusion involve Li^+ diffusion within the anode, transport through the Solid State Electrolyte (SSE)/anode interface into the SSE, diffusion through the SSE from anode to cathode, transport through the SSE/cathode interface into the cathode, and diffusion within the cathode material. Hence, a generic EIS of SSBs is presented in figure 3.9: [97]

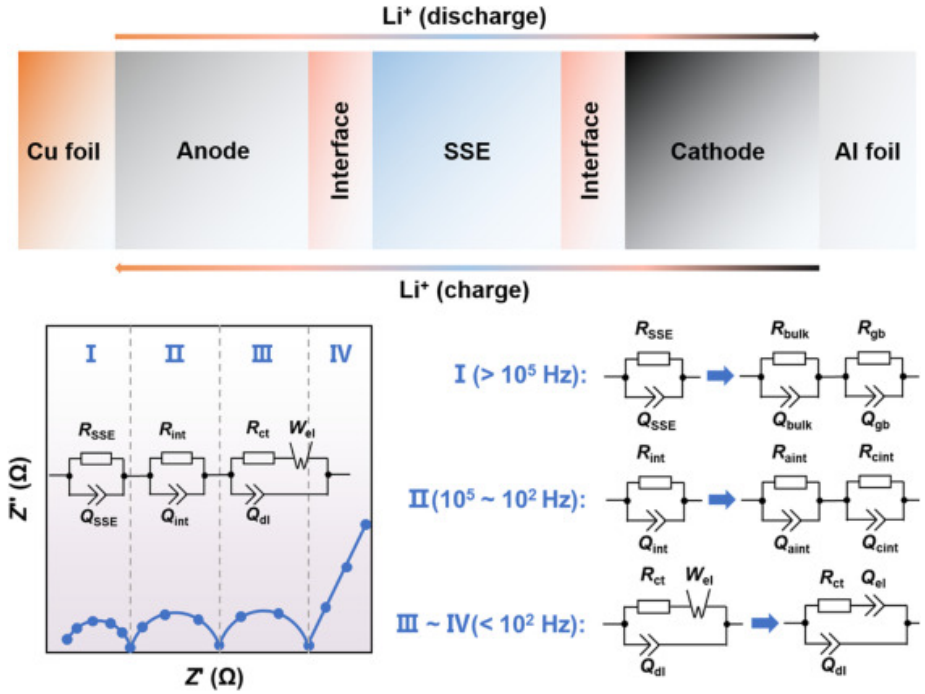

Figure 3.9: Generic physical model for EIS investigation of SSBs. [96]

The impedance spectrum can be divided into four distinct regions: Region I, characterized by a semicircle at high frequency, is attributed to the SSE impedance; Region II, identified by a semicircle at medium frequency, is associated with the SSE/electrode interface impedance, which is caused by solid-solid contact or side-reaction products; Region III, marked by a semicircle at low frequency, corresponds to the SSE/electrode interface charge transfer impedance; and Region IV, indicated by an inclined line at low frequency, represents the Li^+ diffusion impedance within the electrode material, also known as Warburg impedance.

However, certain solid-state batteries (SSBs) exhibit inductive behavior due to increased capacitance at high frequencies (red zone - figure 3.10). This behavior is induced by dielectric materials that are polarized by electric fields, resulting in ferroelectric molecules. These dipoles interact with the applied electric field, resulting in a phase lag and an inductive reaction, similar to how an inductor resists abrupt changes in current. [98]

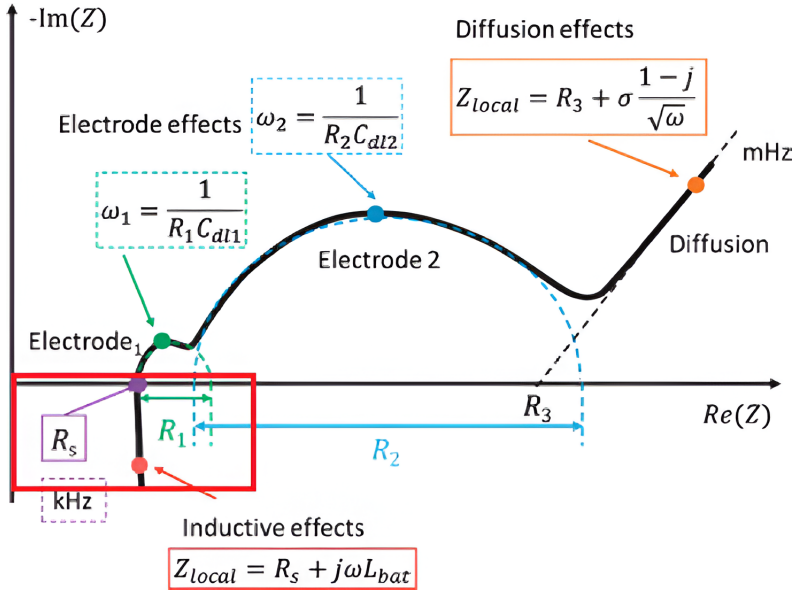

Figure 3.10: Inductive behavior in SSBs. [98]

Nyquist plots enable qualitative and quantitative analysis, identifying equivalent circuits and quantifying resistances and capacitances through fitting to experimental data. [94]

The equivalent circuits used in these graphs are composed of various electrical components that model the behavior of the system which will be described in the following subchapter.

3.6.1.1 Impedance Components in Electrochemical Systems

Charge transfer resistance (R_{CT} or R_p) is the resistance during ion transfer from the electrolyte to the electrode. [99]

Solution resistance (R_{SOL} or R_s) refers to the resistance offered by the electrolyte to the flow of electric current. [100]

The Constant Phase Element (CPE) is fundamental for modeling electrochemical phenomena, as it represents both the double-layer capacitance and the heterogeneities within the system.[100]

The impedance of a CPE is given by: [100]

$$Z_{\mathrm{CPE}} = \frac{1}{Q(j\omega)^a} \tag{3.4}$$

where Q is the effective coefficient and a ranges from 0 to 1, indicating a pure capacitor when

$a = 1$ and a pure resistor when $a = 0$. [100]

Warburg impedance (W) is linked to the ion diffusion behavior in electrochemical materials and is essential for distinguishing between two types of diffusion: semi-infinite linear diffusion and finite-length diffusion. Each type presents unique impedance characteristics in electrochemical systems.[100]

Semi-infinite linear diffusion assumes the diffusion layer is much thinner than the sample, allowing for analysis in a semi-infinite space. Warburg impedance represents the resistance to electroactive species' diffusion, proportional to the inverse square root of frequency ($Z_W \propto \omega^{-1/2}$). In the Nyquist plot, this appears as a 45° line. At low frequencies, impedance diverges towards the negative imaginary axis, indicating no current flow. [100]

Finite-length diffusion has a layer thickness limited by the sample's physical thickness, more realistic for systems with barriers. The layer thickness (L_D) depends on the diffusion coefficient (D) and frequency (ω). Reflective boundaries result in a vertical line in the Nyquist plot, while absorptive boundaries result in a distorted semicircle. [100]

3.6.2 Cyclic Voltammetry

Cyclic voltammetry (CV) is an electrochemical technique used to study the characteristics of an electrochemical system by cyclically varying the electrode's potential between two limits at a constant rate while monitoring the current response. The chosen voltage range and scan rate are based on the experiment's objectives. In the CV measurement of the coin cells, a scan rate of 0.1 V/s was selected. [101]

Various typical CV diagrams are depicted in figure 3.11: [101]

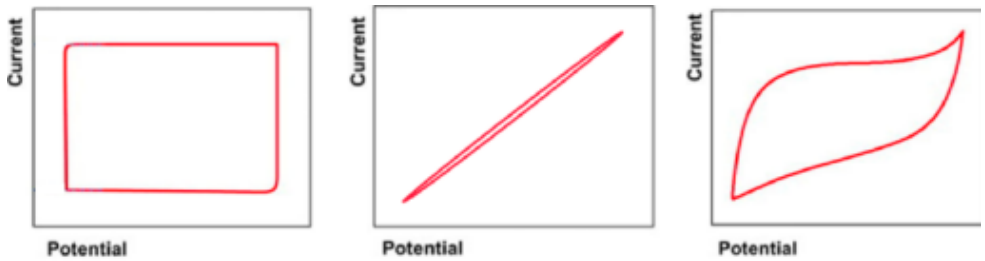

Figure 3.11: Typical CV diagram (a) for an ideal supercapacitor; (b) with mostly resistive behavior; (c) of a device of distorted energy storage due to faradaic reactions

For an ideal supercapacitor, for instance, the CV diagram exhibits a rectangular shape, with

the current showing only two possible values, reflecting that:

$$I = C\frac{d\Delta V}{dt}, \tag{3.5}$$

Where C is the capacitance of the capacitor and the scan rates change with the potential.[101]

For the case of pure resistance, the expected CV diagram will be a straight line with a slope of $\frac{1}{R}$, as according to Ohm's law, $\Delta V = IR$. [101]

Additionally, Fig. 3.11 (C) presents a CV diagram typical of an electric energy storage device, distorted due to faradaic reactions (chemical reactions involving electron transfer, oxidation, or reduction). Oxidation and reduction peaks indicate lithiation and de-lithiation processes occurring in the cell. This occurs when applied potentials cause the removal and addition of electrons to chemical species in the electrolyte, respectively. [101]

The main characteristics of a cyclic voltammogram (CV) representing a reversible reaction include: a well-defined voltage separation between current peaks, the uniformity of peak voltages with varying scan rates, the ratio of peak currents (forward to reverse) being equal to one, and the peak currents being proportional to the square root of the scan rate, as is shown in the figure 3.12. [102]

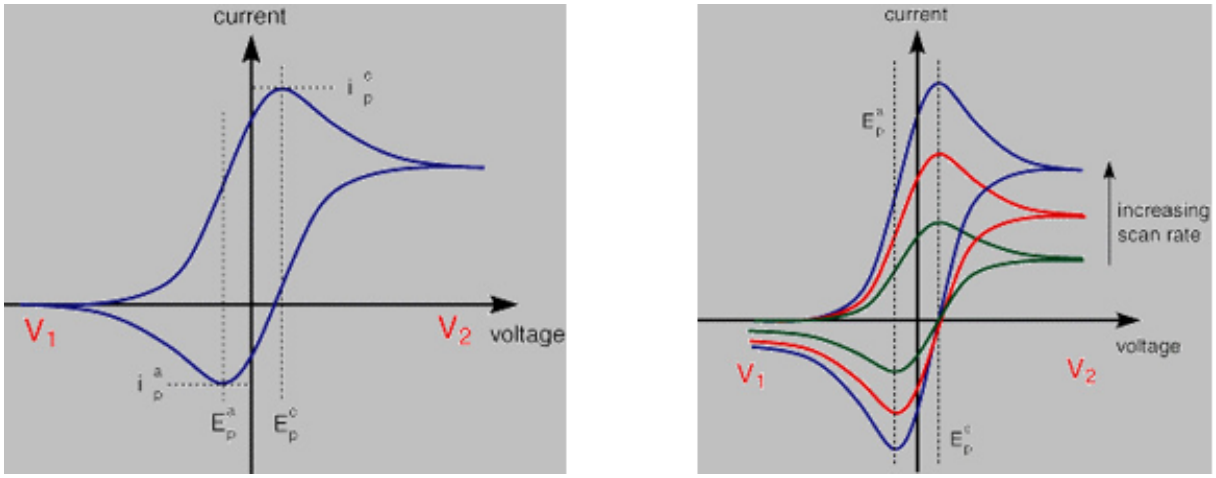

Figure 3.12: Left: Typical reversible cyclic voltammogram characteristics; Right: Effect of increasing scan rate on CV. [102]

3.6.3 Chronoamperometry

Chronoamperometry is a technique used to assess the electrical properties of solid electrolytes by observing steady-state currents. [103]

The total ionic transfer number (Li^+) was calculated using equation 3.6:

$$t_{\text{ion}} = \left(\frac{I_t - I_e}{I_t} \right) \times 100 \tag{3.6}$$

The transference number is the ratio of cation-derived electric current to total electric current. Initially, the total current I_t consists of both ionic current I_i and electronic current I_e, but over time, I_i decreases to nearly zero, leaving only the stable electronic current I_e. A value close to one suggests that the overall conductivity in this system is primarily driven by ion movement, with minimal contribution from electrons. [104]

A typical chronoamperometry graph (figure 3.13) displays the initial current (I_t), followed by the stable current/electronic current (I_e) over time. [103]

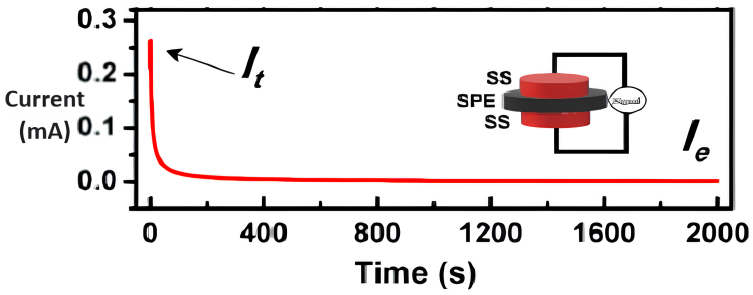

Figure 3.13: Typical chronoamperometry [103]

The open-circuit potential (OCP) was initially measured, followed by applying an OCP-associated potential, and subsequently, a fixed potential of 1V was applied [103]. Measuring the OCP before applying potentials stabilizes the system by achieving equilibrium and minimizing data distortions from rapid changes. Applying a potential close to the OCP allows a smooth transition, reducing transient effects. In contrast, directly applying 1V might result in unstable reactions and distortions owing to sudden shifts. This gradual approach (OCP -> OCP-associated potential -> 1V) ensures more consistent and reliable data for system evaluation.

3.6.4 Galvanostatic Charge and Discharge

Galvanostatic Charge-Discharge (GCD) is a technique for evaluating the performance and lifetime of EDLCs and batteries. It entails charging the cell with a predetermined current until it achieves a maximum voltage, and then discharging with a negative current until a minimum voltage is achieved [105]. This technique yields data on specific capacity, cell activity at various C rates, coulombic efficiency, and life cycle. The cell's composition and architecture influence charge and discharge performance, with potential limits dictated mostly by the cathode's active material, as well as electrolyte deterioration at specified voltages. [105]

Figure 3.14 illustrates the voltage profiles during charge and discharge cycles. The initial charge curve shows a rapid voltage increase followed by a plateau, while the discharge curve shows a steady voltage decrease. The second cycle's improved performance indicates stabilization and capacity retention of the material. [106]

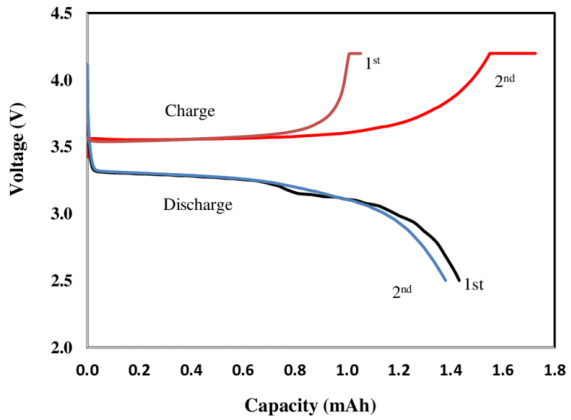

Figure 3.14: Typical charge and discharge voltage versus capacity. [106]

Conclusively, this chapter outlines the comprehensive experimental methodologies employed in this study.

Chapter 4

Results and Discussion

In order to better understand and develop solid-state electronics for increased efficiency, stability, and performance, this effort entails testing and experimentation. Analysing data is essential to this process since it offers insightful information. The objective is to present a thorough and open picture of the work, showcasing the scientific method in SPE optimization.

Several distinct electrolytes were developed for this thesis. The study commenced with the fabrication of SPEs using PVDF as the polymer matrix and $LiClO_4$ as the salt. The initial focus was on identifying the optimal PVDF concentration.

4.1 Solid Electrolyte - PVDF / $LiClO_4$

SPEs were initially prepared using PVDF as the polymer matrix and $LiClO_4$ as the salt. Finding the ideal PVDF concentration to provide the best possible relationship between conductivity, stability, and porosity is the first step.

Three membranes were produced with varying PVDF polymer concentrations (5%, 10%, and 15%), made by NIPS.

4.1.1 FTIR in PVDF membrane

This experiment involved polymer membranes containing varying quantities of PVDF. The composition of the β phase was examined, and FTIR was also employed to assess the material processing, particularly focusing on the fingerprint region to evaluate the success of the procedure.

Figure 4.1 presents the FTIR-ATR spectra of PVDF membranes with different concentrations.

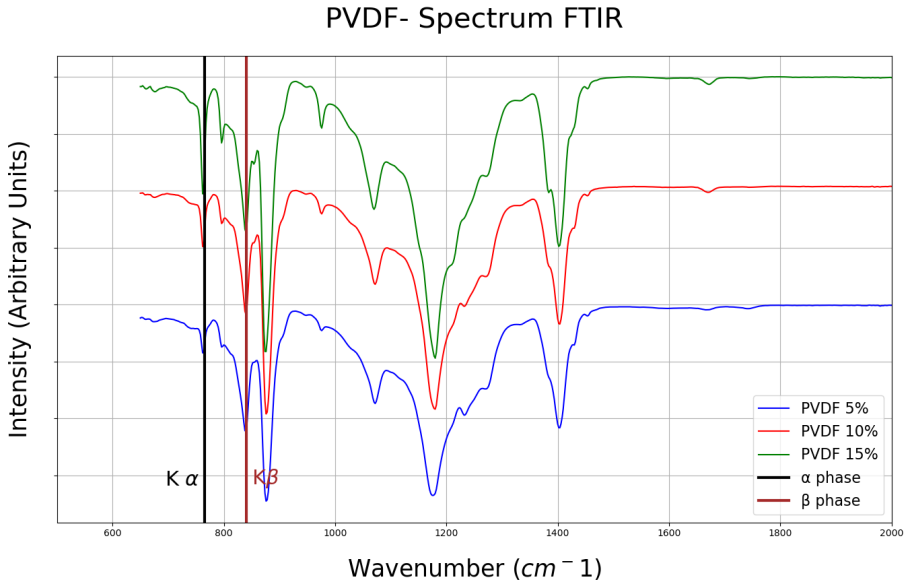

Figure 4.1: FTIR-ATR spectra of the different PVDF membranes

The α and β phases are represented by the peaks at 763 cm^{-1} and 840 cm^{-1} in all samples, respectively. There are no appreciable variations in the spectra obtained from various membranes.

Using equation 2.6 and the absorbances A_α and A_β, the proportion of the electroactive β phase was determined and results presented in figure 4.2.

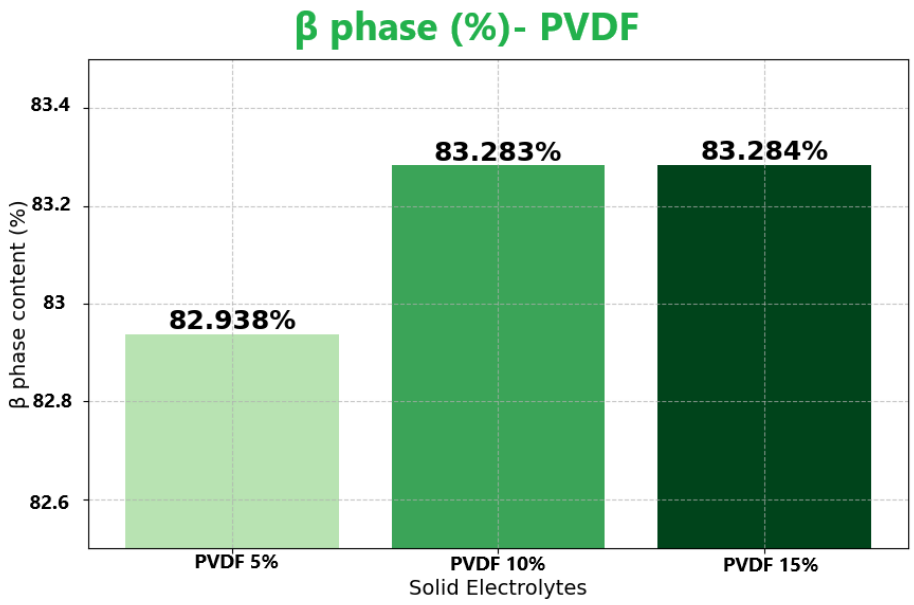

Figure 4.2: β phase content of the PVDF membranes

The crystallization of PVDF in the β phase was successfully achieved as desired. There are no significant differences in β phase content between all PVDF membranes. Therefore, other criteria are necessary to select the optimal PVDF percentage. It is essential to select the PVDF concentration that creates the densest and most cohesive membrane, ensuring mechanical stability while allowing for future integration of the salt into the polymer. Hence, porosity testing is necessary.

4.1.2 PVDF membrane porosity

Figure 4.3 shows the porosity testing made to different PVDF concentrations.

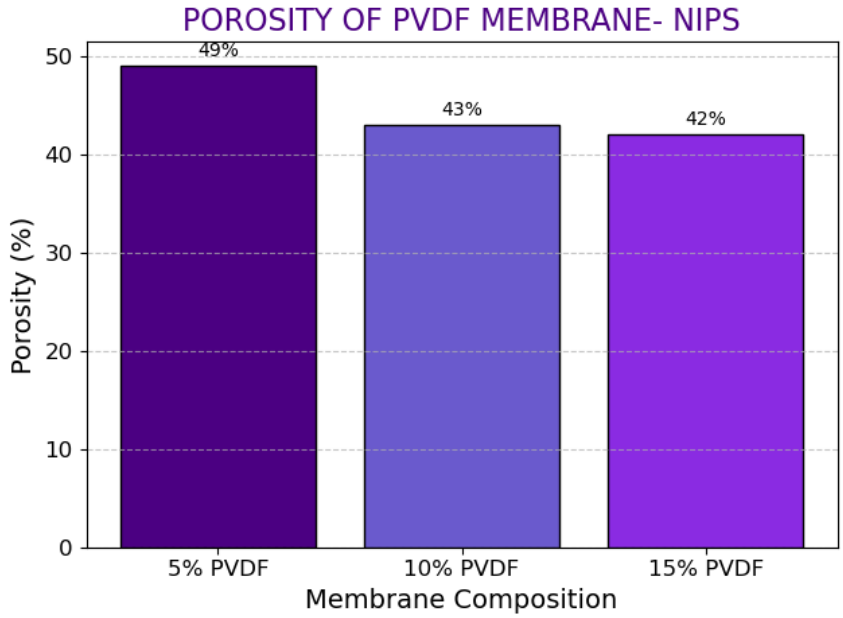

Figure 4.3: PVDF membrane using the NIPS method

The graph shows that increasing PVDF content reduces porosity. A higher polymer-to-solvent ratio increases solution viscosity, leading to a denser membrane with fewer pores, thus reducing overall porosity. Higher PVDF concentrations were capped at 15% as higher levels led to excessive viscosity, poor mixing, and defective films. Thus, 15% was chosen because it results in a denser membrane, which enhances mechanical strength and robustness.

The next section will focus on studying PVDF / $LiClO_4$ membrane porosity, which is crucial for creating membranes that balance mechanical durability with optimal ion permeability, ensuring membranes can withstand battery operation stresses while maintaining efficient ion transport.

4.1.3 PVDF / $LiClO_4$ membrane porosity

This section presents a comparison of the porosity of PVDF membranes with different concentrations of $LiClO_4$ fabricated using two different methods: the Doctor Blade technique and the NIPS method.

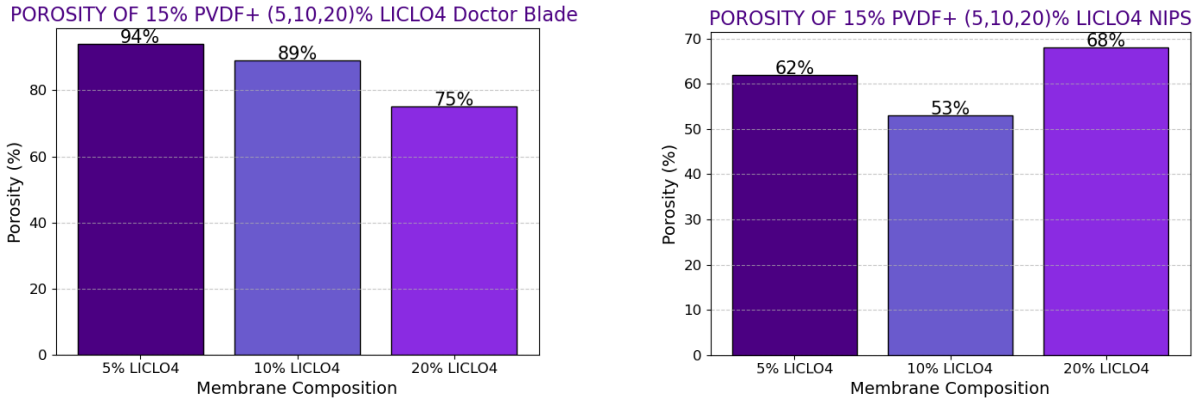

(a) (b)

Figure 4.4: Porosity comparison of PVDF membrane with different $LiClO_4$ concentrations, (a) by the Doctor Blade method; (b) by the NIPS method

These graphs demonstrate that when compared to the Doctor Blade procedure, the NIPS method yields membranes with lower porosity. This is because the NIPS technique creates a dense structure with fewer pores by including a quick solvent exchange. In contrast, the Doctor Blade approach uses a lengthy solvent evaporation process at room temperature. The solvent diffusion is slower, thus leading to a slower restructuration and resulting in a more porous and open structure.

As seen in the state of the art, $LiClO_4$ affects PVDF membranes by increasing pore size and disrupting crystalline structure [67]. However, it was observed that the porosity of membranes formed by the Doctor Blade method decreased as $LiClO_4$ concentrations increased, with this effect being influenced by membrane thickness differences. The average thickness of membranes with 5% $LiClO_4$ was 17 μm, whereas those with 20% $LiClO_4$ had an average thickness of 61.5 μm.

On the other hand, membranes created using the NIPS approach demonstrated the expected behavior: the porosity of the 20% $LiClO_4$ membrane was larger than that of the 5% $LiClO_4$ membrane, which is consistent with the theory, as the thicknesses were considerably more equal. This suggests that membrane thickness is a key component in determining porosity.

The measurement of porosity using butanol is not as precise as other techniques, such as mercury porosimetry, which, although expensive and destructive, provides more reliable results. If laboratory conditions, like temperature, vary from one day to the next, the measurement results can differ. Additionally, while the NIPS process forms small pores, the resulting structure is not homogeneous, which can lead to an uneven distribution of pores on different membrane surfaces, making the results uncertain. The process of removing excess butanol from the membrane is also subjective and not very precise.

4.1.4 LIBS study in PVDF / $LiClO_4$

The graph presented in figure 4.5 illustrates the lithium constitution in three different membranes, all of which contain 10% $LiClO_4$, but have varying concentrations of PVDF: 5%, 10%, and 15%.

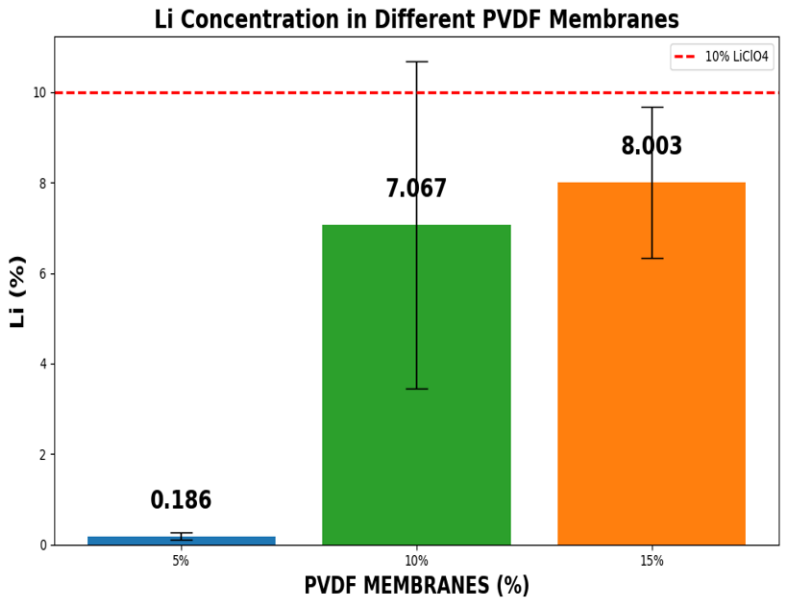

Figure 4.5: LIBS study in PVDF / $LiClO_4$ electrolyte made by NIPS

The observed loss of $LiClO_4$ in the membranes with 10% and 15% PVDF was minimal, around 2% and 3%, respectively, suggesting that this loss is more likely due to minor operational errors rather than significant dissolution. In contrast, the 5% PVDF membrane exhibited no detectable $LiClO_4$ due to its higher porosity and larger pores, which facilitate water penetration and perchlorate dissolution.

For the 15% PVDF membrane used in the SPE, the primary challenge is the non-uniform

distribution of $LiClO_4$ resulting from the NIPS process. This method fails to achieve the uniform distribution found with the Doctor Blade method. The latter provides a more consistent dispersion of $LiClO_4$ even at lower concentrations, such as 5%, which enhances electrochemical performance. In contrast, only high concentrations of $LiClO_4$, like 20%, in the NIPS process manage to achieve a uniform distribution, whereas lower concentrations, like 5% and 10%, lead to poorer performance.

4.1.5 FTIR in PVDF / $LiClO_4$

Figures 4.6a and 4.6b presents the FTIR spectra of PVDF / 20% $LiClO_4$, using both the NIPS and Doctor Blade methods. The analysis focused on the 20% salt concentration, as this is where the most significant differences in the β-phase formation could be observed, highlighting the strongest interaction between PVDF and $LiClO_4$ compared to lower concentrations like 5% and 10%.

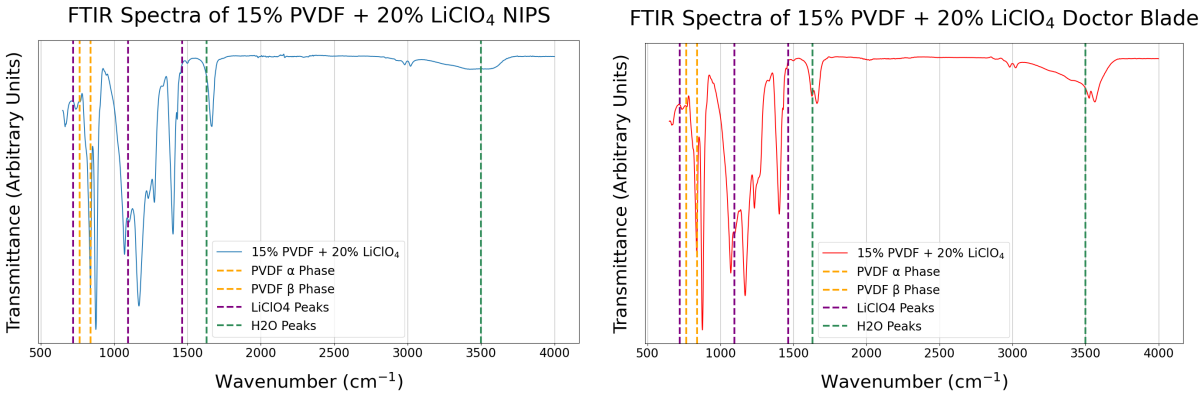

(a) (b)

Figure 4.6: FTIR study in PVDF / $LiClO_4$ membranes, (a) by NIPS method; (b) by Doctor Blade method.

FTIR analysis of PVDF / $LiClO_4$ membranes made by Doctor Blade, reveals a significant absorption peak at 3500 cm^{-1}, indicating a high level of water absorption. This characteristic highlights a notable disadvantage, as the membrane's performance can be compromised due to moisture uptake when exposed to ambient conditions. Conversely, SPE made by NIPS does not exhibit this water absorption issue.

For SPE made by Doctor Blade, β phase content was determined.

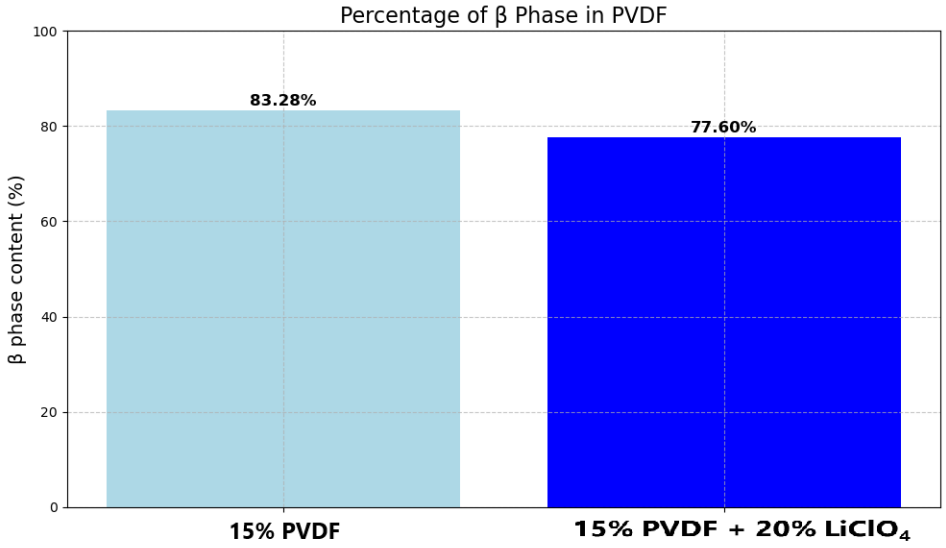

Figure 4.7: FTIR test in PVDF / $LiClO_4$ electrolyte

It is well-known that the addition of $LiClO_4$ to PVDF films leads to a decrease in the β phase content. This is due to the formation of weak "acid-base" complexes between LiClO and PVDF chains, disrupting the ordered arrangement and hindering the formation of well-defined crystalline structures. [68]

4.1.6 Arrehenius law - PVDF / $LiClO_4$

The figure 4.8 shows the impedance response of the solid polymer electrolyte (SPE) with 15% PVDF and 20% $LiClO_4$ made by Doctor Blade at different temperatures, illustrating how resistance changes with temperature. A fitting for each temperature was performed using its equivalent circuit.

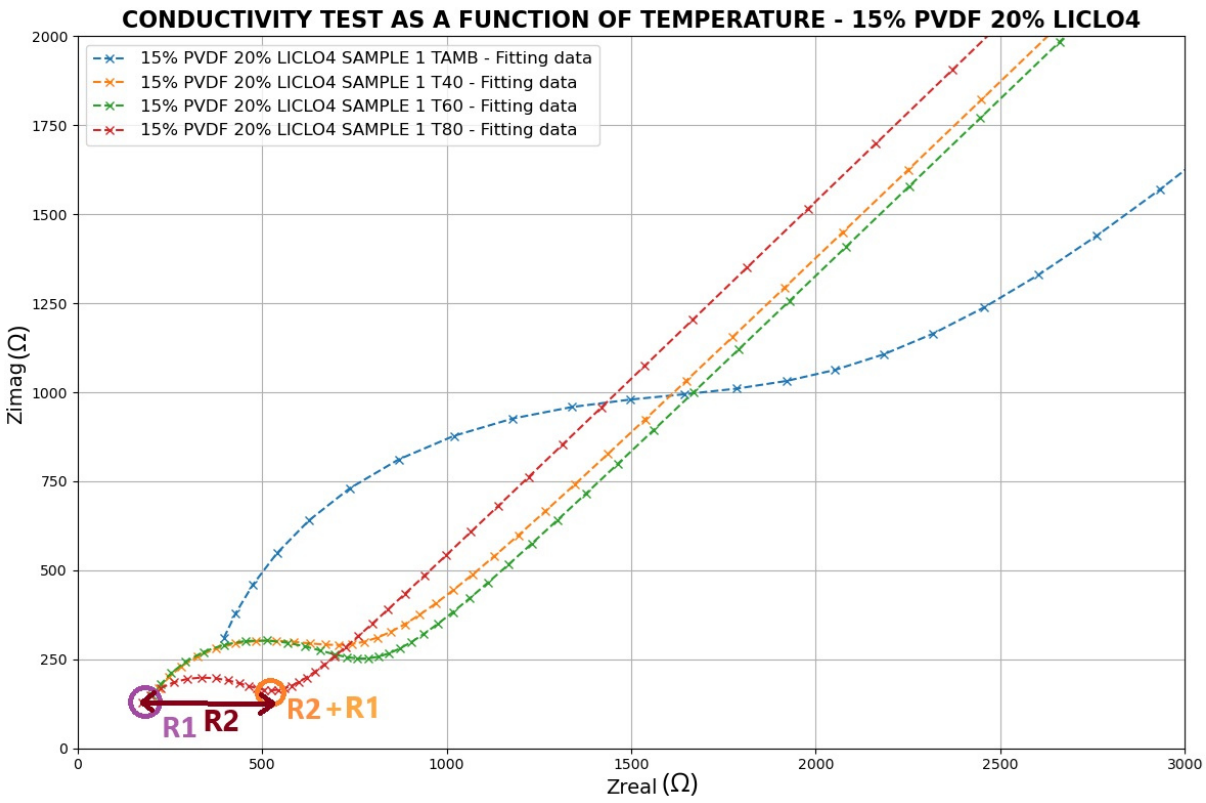

Figure 4.8: Impedance spectra of 15% PVDF 20% $LiClO_4$ at various temperatures.

The test confirmed that R_2 should be used for calculating the conductivity of the SPE, not R_1, due to significant variation in R_2. This confirms single ion conduction and anions' immobility.

Additional impedance tests conducted in the MaTEr Lab using gold electrodes confirmed this finding. The tests revealed that R_1 was 0, validating R_2 as the correct resistance for determining the conductivity of PVDF / $LiClO_4$.

The activation energy of the solid polymer electrolyte (SPE) was determined using the Arrhenius law, which relates the logarithm of conductivity to $\frac{100}{T}$.

The SPE made by the Doctor Blade method resulted in an activation energy of 0.78 eV/mol.

This test involved placing the Swagelok cell containing the SPE in an oven, removing it, and then measuring the EIS. Variations in the measurements can be attributed to potential experimental errors. Firstly, the oven may not have maintained the exact temperature indicated on the panel. Secondly, the Swagelok cell, which houses the SPE, might not have been thermally stable within the oven, leading to non-homogeneous temperatures. Lastly, removing the cell from the oven for a few seconds before measuring impedance could cause heat dissipation, introducing

errors. This procedure was necessary because placing the potentiostat cables inside the oven generates significant noise due to the Joule effect, which interferes with the measurements.

4.1.7 Lithium charge transfer calculated by Chronoamperometry- PVDF / $LiClO_4$

The lithium charge transfer coefficient in an SPE of 15% PVDF and 20% $LiClO_4$ is 0.907, determined by equation 3.6, where initial current and stead current are shown in figure 4.9, indicating efficient lithium-ion mobility within the electrolyte. This high efficiency in ion conduction leads to low resistance to lithium-ion movement, enhancing battery efficiency and performance in lithium-ion batteries.

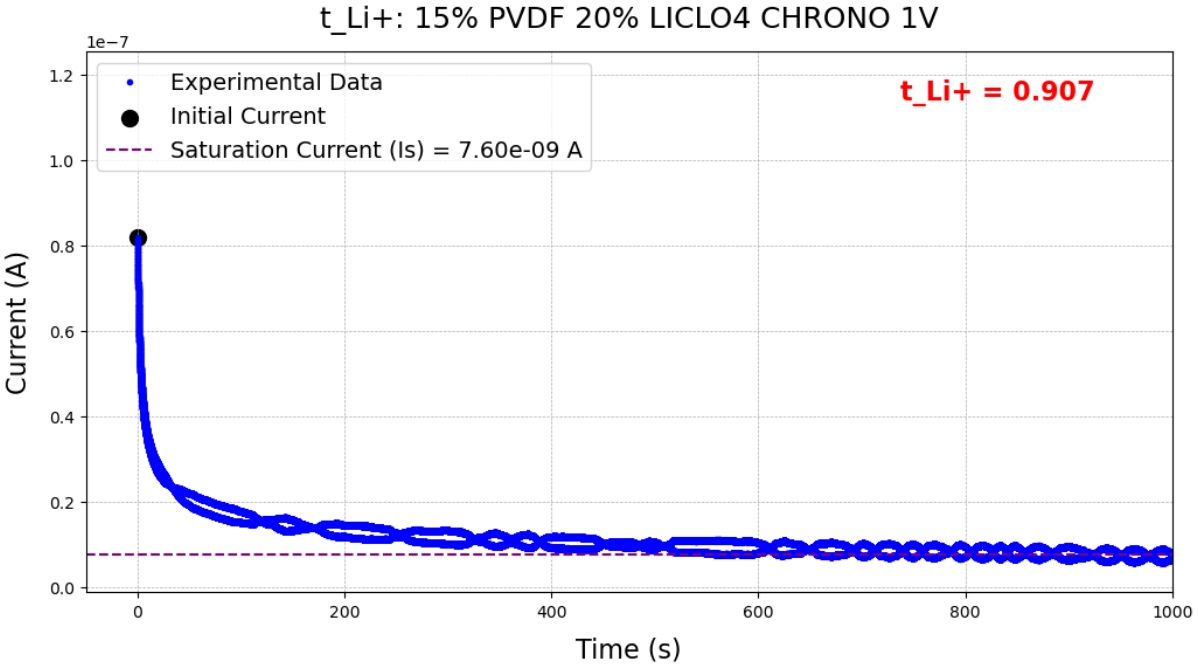

Figure 4.9: Chronoamperometry- 15% PVDF / 20% $LiClO_4$ SPE made by Doctor Blade

4.1.8 $LiClO_4$ Concentration Optimization

The next step is to use the optimal PVDF concentration of 15% while varying the $LiClO_4$ concentration at 5%, 10%, and 20%. The objective is to observe how conductivity changes with $LiClO_4$ concentrations and to determine the ionic conductivity.

Figure 4.10 shows the corresponding circuit and fitting for the 15% PVDF / 20% $LiClO_4$ SPE manufactured by NIPS. It shows how the fitting is achieved using the equivalent circuit,

serving as an example for all impedance data where the SPE conductivity is determined.

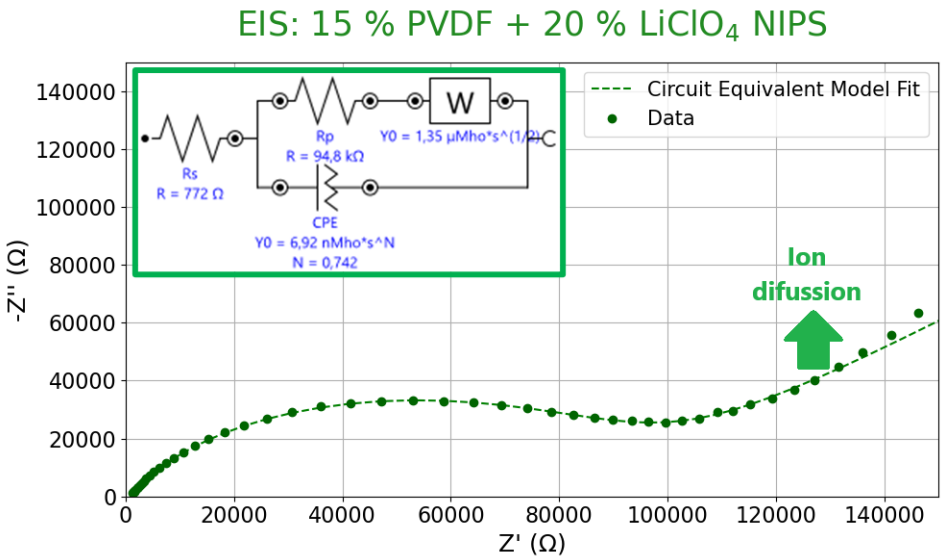

Figure 4.10: Equivalent circuit and its fitting of 15% PVDF / 20% $LiClO_4$ SPE made by NIPS

Table 4.1 presents the ionic conductivity of PVDF / $LiClO_4$ electrolytes produced by NIPS and Doctor Blade methods, determined by the ionic conductivity equation 3.3:

Table 4.1: Ionic conductivity of PVDF / $LiClO_4$ electrolytes made by NIPS and Doctor Blade

15% PVDF / $LiClO_4$			
Method	% $LiClO_4$	$L_{Average}(\mu m)$	Average Ionic conductivity (S cm^{-1})
NIPS	20	55.8 ± 22.61	(3.03 ± 1.05) x 10^{-7}
DOCTOR BLADE	5	19 ± 2	(6.06 ± 4.67) x 10^{-9}
	10	30.3 ± 3.5	(3.48 ± 1.62) x 10^{-8}
	20	28 ± 3	(2.51 ± 1.68) x 10^{-7}

It's conclusive that higher concentrations of $LiClO_4$ improve ionic mobility by increasing the availability of mobile ions and establishing more frequent routes for ion migration.

Table 4.1 does not include the 5% and 10% $LiClO_4$ membranes made by NIPS, as the salt did not become homogeneous within the membrane during the NIPS process. This led to undetectable conductivity values for these concentrations in most areas of the membrane. Consequently, the

impedance spectra for these samples did not exhibit the typical characteristics of ion diffusion and movement, instead resembling those of a polymer without effective ion conduction.

4.2 Solid Electrolyte: PVA / NaAlg / $LiClO_4$

After studying the PVDF-based electrolytes with $LiClO_4$, ionic conductivity results were not the best suited for application in the desired application. Therefore, a blend of PVA and Sodium Alginate arose as a promising solution for application as a SPE. Therefore, PVA / NaAlg / $LiClO_4$ solid polymer electrolyte is another candidate.

4.2.1 PVA / NaAlg FTIR analyse

Tracing and analysing the absorption peaks in the FTIR study of PVA SPE with sodium alginate is a fundamental step in understanding the structure, interactions, and properties of the material, as well as guiding the development and optimization of practical applications.

The FTIR spectrum exhibits key peaks corresponding to characteristic vibrations of PVA / NaAlg blend. The O-H stretching at 3400 cm^{-1} aligns with the theoretical peak for the PVA / NaAlg blend at 3422 cm^{-1}. Similarly, the C-H stretching observed at 2900-3000 cm^{-1} matches the blend's theoretical peak at 2936 cm^{-1}. The C=O stretching appears between 1600-1750 cm^{-1}, aligning with the theoretical peak for the PVA / NaAlg blend at 1715 cm^{-1} (C=O stretching) [107] [49]. These observations confirm the presence and interaction of PVA and NaAlg in the blend.

The FTIR spectrum figure 4.11 reveals the characterization of the main peaks in the PVA / NaAlg blend.

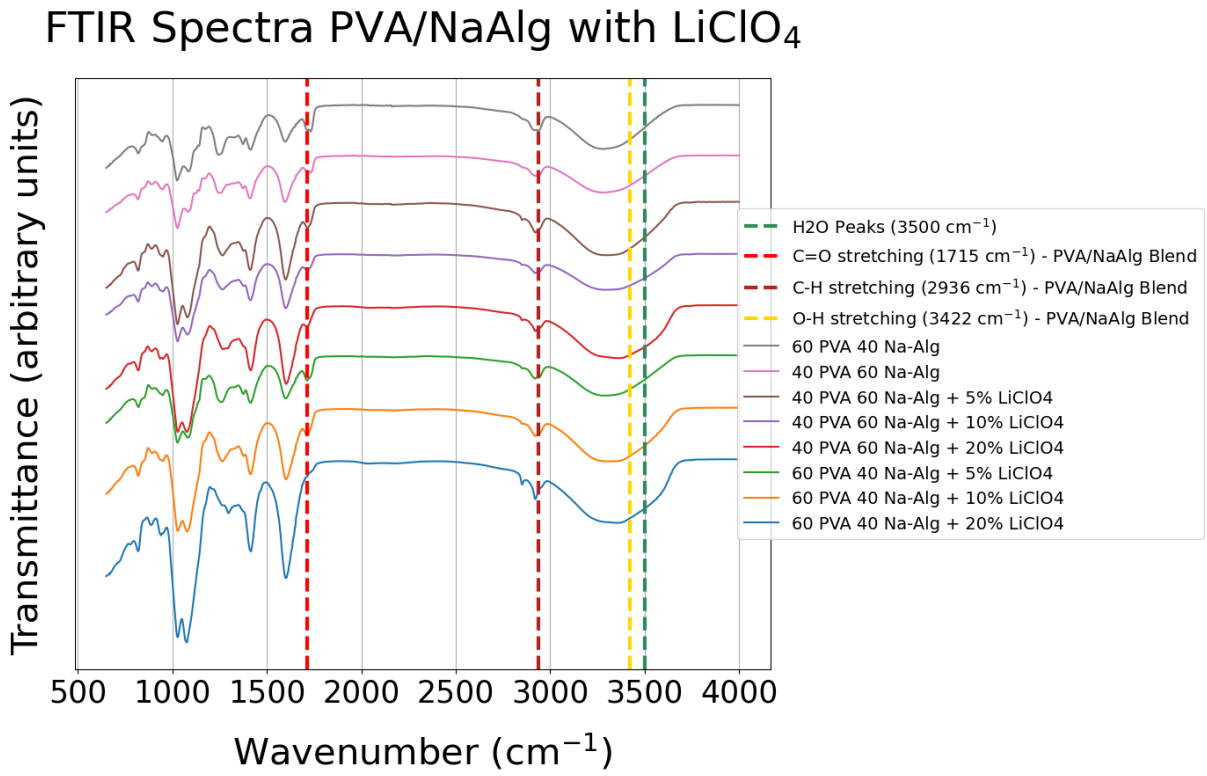

Figure 4.11: FTIR test in 60:40 PVA / NaAlg / (5,10,20) % $LiClO_4$ electrolytes and in 40:60 PVA / NaAlg / (5,10,20) % $LiClO_4$

Generally, the 3422 cm^{-1} (O-H stretching) and 2936 cm^{-1} (C-H stretching) peaks decrease with higher $LiClO_4$ concentrations, reflecting changes in hydrogen bonding and polymer matrix interactions. However, conclusions for these last peaks are challenging due to overlap with the 3500 cm^{-1} water absorption peak, indicating high hydrophilicity.

4.2.2 Porosity test in PVA / NaAlg / $LiClO_4$ membrane

Figure 4.12 illustrates the porosity of PVA / NaAlg membranes with varying concentrations of $LiClO_4$.

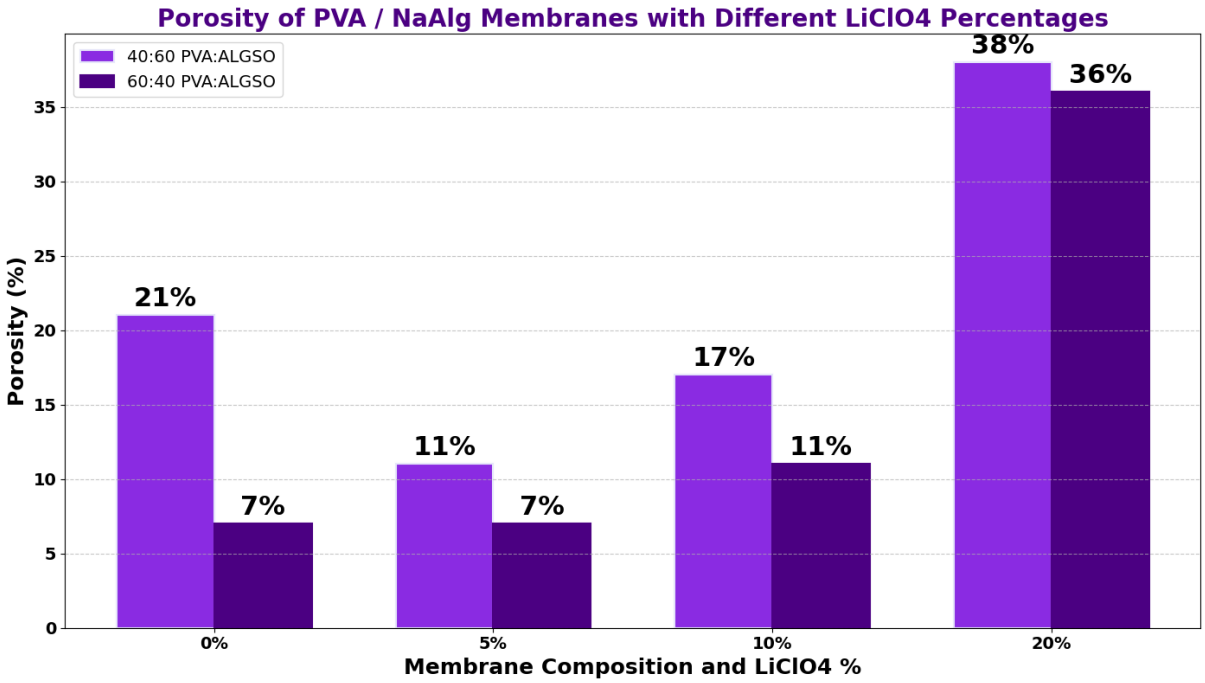

Figure 4.12: Porosity test in 60:40 PVA / NaAlg / (5,10,20) % $LiClO_4$ electrolytes and in 40:60 PVA / NaAlg / (5,10,20) % $LiClO_4$

As explained in the state of the art, the addition of $LiClO_4$ to the PVA / NaAlg composite increases crystallinity and reduces porosity by forming hydrogen bonds with Li^+ ions, leading to tighter packing, higher crystallinity, and occupation of defects and free volume holes by Li^+ and ClO_4^- ions. [49]

However, the observed results did not align with this expectation. The discrepancy arises because the electrolyte membranes tested had inconsistent thicknesses. For example, the average thickness of the membrane with 40:60 PVA / NaAlg / 10% $LiClO_4$ is approximately 116.33 μm, while that of the membrane with 40:60 PVA / NaAlg / 20% $LiClO_4$ is approximately 32.33 μm. Thinner membranes tend to have higher porosity due to a higher proportion of void spaces relative to material volume. Controlling membrane thickness at the micrometer level in the formation of SPEs is challenging, and variations in thickness can significantly impact measured porosity, leading to unexpected results.

The membrane with 40 % PVA and 60 % NaAlg is expected to have higher porosity, as was experimentally confirmed and can be seen in the bar graph above. The increased NaAlg content leads to a significant reduction in crystallinity and the formation of greater amorphous regions, resulting in a more porous membrane structure.

4.2.3 Mechanical Properties of PVA / NaAlg / $LiClO_4$ membrane

Figure 4.13 presents the tensile test results in the longitudinal direction following the movement of the doctor blade, which spread the solution and formed the film. Despite tests in both longitudinal and transverse directions being crucial for understanding a material's mechanical properties, the longitudinal direction remains more significant.

Note that only one replicate for each type of membrane is presented in the following figure.

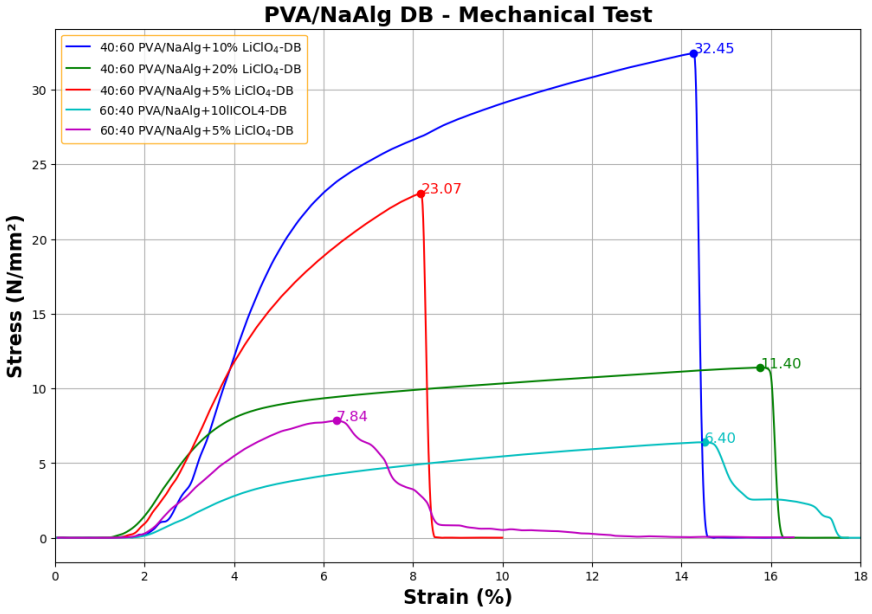

Figure 4.13: Tensile stress-strain curves for PVA-NaAlg membranes in machine direction/ Doctor Blade direction (DB)

Table 4.2 shows the mechanical properties of 40:60 and 60:40 PVA / NaAlg blends with different $LiClO_4$ concentrations, measured in the machine direction (DB) and perpendicular to the machine direction (DO).

Table 4.2: Mechanical properties of 40:60 and 60:40 PVA / NaAlg blends with different $LiClO_4$ concentrations.

Property	40:60 PVA / NaAlg						60:40 PVA / NaAlg	
	5% $LiClO_4$ DB	5% $LiClO_4$ DO	10% $LiClO_4$ DB	10% $LiClO_4$ DO	20% $LiClO_4$ DB	20% $LiClO_4$ DO	5% $LiClO_4$ DB	10% $LiClO_4$ DB
thickness (µm)	17.6	17.3	7	17.4	31.35	40.2	12.3	33
Tensile Strength (MPa)	26.15 ± 3.07	21.27	37.57 ± 5.13	13.78	8.75 ± 2.64	7.78 ± 0.15	7.84	6.4
Young's modulus (MPa)	468.19 ± 55.80	274.15	558.15 ± 27.67	321.56	193.45 ± 18.61	165.14 ± 11.32	168.78	129.67
Elongation (%)	7.20 ± 0.84	6.61	8.34 ± 3.33	6.85	11.25 ± 2.99	5.87 ± 1.44	4.37	12.51

The mechanical properties for the 60:40 PVA / NaAlg + 20% $LiClO_4$ membrane were not reported in the table 4.2 due to its extremely poor mechanical performance, which prevented the test from being initiated.

The tensile strength and Young's modulus decrease with $LiClO_4$ concentration due to Li^+ ions' plasticizing effect on polymer chains, reducing intermolecular forces and allowing more chain mobility. However, elongation increases as chains move freely, enhancing stretchability. The 40:60 PVA / NaAlg blend shows higher strength and higher Young´s modulus

4.2.4 Arrhenius law - PVA / NaAlg / $LilClO_4$

Table 4.3 shows the activation energy (Ea) for different PVA / NaAlg blends as the $LiClO_4$ concentration varies.

Table 4.3: Activation Energy (Ea) of PVA / NaAlg blends with varying $LiClO_4$ concentrations.

PVA / NaAlg Ratio	$LiClO_4$ %	Activation Energy (Ea) (eV/mol)
60:40	5%	1.46
	10%	1.02
	20%	0.89
40:60	5%	4.38
	10%	0.47
	20%	0.90

Based on this table, activation energy decreases with increasing % of $LiClO_4$. Higher concentrations of $LiClO_4$ facilitate ionic conduction, reducing energy barriers. However, there is an exception where 40:60 PVA / NaAlg with 10% $LiClO_4$ showed a higher activation energy (0.47

eV/mol) compared to 40:60 PVA / NaAlg with 20% $LiClO_4$ (0.90 eV/mol). This anomaly could be due to errors previously discussed in section 4.1.6 regarding Arrhenius law - PVDF / $LiClO_4$.

As with the PVDF / $LiClO_4$ SPE, varying the temperature in the PVA / NaAlg / $LiClO_4$ SPE showed that R_2 also varied, indicating the immobilization of anions and confirming single-ion conduction in the PVA / NaAlg / $LiClO_4$ SPE. Therefore, R_2 is used to accurately determine the conductivity of these membranes.

4.2.5 Lithium charge transfer- PVA / NaAlg / $LilClO_4$

Table 4.4 shows the transference number (t_{Li^+}) for PVA / NaAlg blends with varying $LiClO_4$ concentrations.

Table 4.4: Transference number (t_{Li^+}) of PVA / NaAlg blends with varying $LiClO_4$ concentrations.

SPE	% $LiClO_4$	t_{Li^+}
40 PVA 60 NaAlg	5%	0.91
	10%	0.93
	20%	0.93
60 PVA 40 NaAlg	5%	0.90
	10%	0.89
	20%	0.95

The table indicates that both the 40:60 and 60:40 PVA / NaAlg blends exhibit relatively high transference numbers (t_{Li^+}), demonstrating effective ionic conduction.

4.2.6 $LiClO_4$ Concentration Optimization

Figure 4.14 illustrates the equivalent circuit and its fitting for the 40:60 PVA / NaAlg / 20% $LiClO_4$ SPE made by Doctor Blade, serving as one example among all measurements conducted.

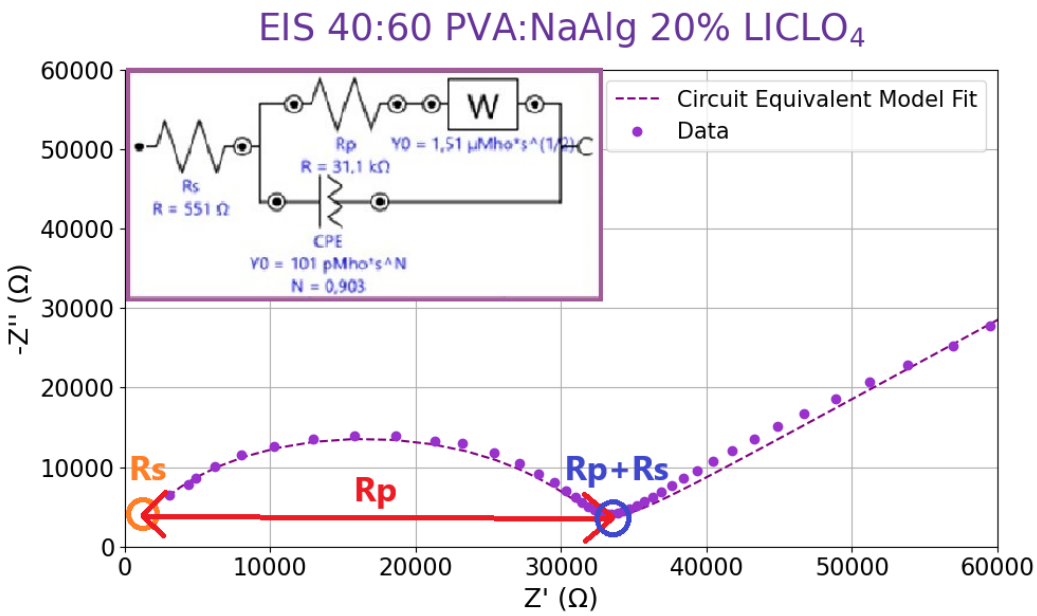

Figure 4.14: Equivalent circuit and its fitting of of 40:60 PVA / NaAlg / 20% $LiClO_4$ SPE made by Doctor Blade

Table 4.5 shows the ionic conductivity of PVA / NaAlg blends made by drop cast and Doctor Blade, with varying $LiClO_4$concentrations.

Table 4.5: Ionic conductivity of PVA / NaAlg blends with varying $LiClO_4$ concentrations.

PVA : NaAlg / $LiClO_4$				
PVA / NaAlg ratio	Method	% $LiClO_4$	$l_{Average}$ (μm)	Average Ionic Conductivity (S cm^{-1})
60 : 40	DROP CAST	5	154.3 ± 31.5	(1.8 ± 1.3) x 10^{-6}
		10	99 ± 22.34	(9.9 ± 4.6) x 10^{-6}
		20	83.75 ± 46.03	(3.8 ± 1.6) x 10^{-5}
	DOCTOR BLADE	5	33.5 ± 6.5	(9.9 ± 2.2) x 10^{-8}
		10	33 ± 7	(2.8 ± 0.5) x 10^{-7}
		20	30.5 ± 0.5	(4.2 ± 0.9) x 10^{-6}
40 : 60	DROP CAST	5	120	1.1 x 10^{-7}
		10	130	2.8 x 10^{-7}
		20	110	2.9 x 10^{-6}
	DOCTOR BLADE	5	46.5 ± 1.5	(2.1 ± 1.2) x 10^{-7}
		10	31.5 ± 8.5	(3.3 ± 0.6) x 10^{-8}
		20	32	1.3 x 10^{-5}

Based on the table, it is concluded that ionic conductivity increases with the percentage of

$LiClO_4$. The conductivity values between the 40:60 and 60:40 PVA / NaAlg ratios do not differ significantly, and both exhibit good conductivity, particularly at 20% $LiClO_4$. However, since the 40:60 ratio demonstrated significantly better mechanical performance (as shown previously), membranes with the 40:60 ratio will be primarily chosen for forming the coin cell.

The drop-casting technique produced slightly better conductivity, but the resulting film thickness was too high. Membranes made with the doctor blade method are closer to the desired 20 μm thickness required for SSBs to compete with liquid electrolyte batteries, being preferred for coin cells. Despite marginally better conductivity from drop-cast membranes, doctor blade membranes are chosen due to their more suitable thickness.

4.3 Coin cell

This section details the fabrication and characterization of coin cells, designed to investigate the impact of various fabrication parameters on their electrochemical performance, particularly focusing on the interaction between SPE and ferroelectric electrolytes to optimize energy storage and conductivity for solid-state batteries.

In the laboratory of MatER, 9 coin cells were prepared in an argon glove box, varying several parameters. In some cells, pressure was applied using a press pressure before assembling the coin cell, while in others, it was not. LFP was pressed with SPE in certain coin cells, while in others, LFP was pressed with SPE and $Li_{2.99}Ba_{0.005}ClO$. Additionally, different numbers of spacers were used: 2 spacers in some cells and 1 in others. Using more spacers increases the resistance of the coin cell but improves its behavior under applied tension when sealing.

Table 4.6: Summary of cell parameters and theoretical specific capacity for different PVDF and PVA / NaAlg blends with $LiClO_4$ and $Li_{2.99}Ba_{0.005}ClO$ additives.

Cell ID	Name SPE + Inorganic Electrolyte	Press pressure	Nº spacers	Synthesis Method	Thickness (L) (µm)	LFP mass (mg)	SPE mass (mg)	ϕ SPE (mm)	$Li_{2.99}Ba_{0.00}$ ClO mass (mg)	Theoretical Specific Capacity (mAh/g)
NE01	40 PVA + 60 NaAlg + 20% $LiClO_4$	Yes. SPE/LFP	2	Doctor Blade	29	12.7	2.1	10	____ __-	10.25
NE02	40 PVA + 60 NaAlg + 20% $LiClO_4$	No	2	Doctor Blade	29	12.6	2	10	____ __-	10.17
CC01	15% PVDF + 20% $LiClO_4$	Yes. SPE/LFP	1	Doctor Blade	50	12.6	4.3	14	____ __-	10.17
CC02	15% PVDF + 20% $LiClO_4$ + $Li_{2.99}Ba_{0.005}ClO$	Yes. SPE/LFP	1	Doctor Blade	50	12.6	2	10	72.9	10.17
CC03	40 PVA + 60 NaAlg + 20% $LiClO_4$ + $Li_{2.99}Ba_{0.005}ClO$	Yes. SPE/LFP	1	Doctor Blade	29	12.4	2.2	10	72.7	10.01
CC04	40 PVA + 60 NaAlg + 20% $LiClO_4$	Yes. SPE/LFP	1	Doctor Blade	29	12.5	4.9	14	____ ___	10.09
CC05	60 PVA + 40 NaAlg + 10% $LiClO_4$	Yes. $Li_{2.99}Ba_{0.005}ClO$ SPE / LFP/	1	Drop Cast	110	12.6	6.6	14	____ ____-	10.17
CC06	15% PVDF + 20% $LiClO_4$ + $Li_{2.99}Ba_{0.005}ClO$	Yes. $Li_{2.99}Ba_{0.005}ClO$ / SPE / LFP/	1	Doctor Blade	50	12.4	2.1	10	72.9	10.01
CC07	40 PVA + 60 NaAlg + 20% $LiClO_4$ + $Li_{2.99}Ba_{0.005}ClO$	Yes. $Li_{2.99}Ba_{0.005}ClO$ / SPE / LFP/	1	Doctor Blade	29	12.5	2	10	72.8	10.09

When LFP was pressed with SPE and $Li_{2.99}Ba_{0.005}ClO$, the resulting coin cell exhibited high resistance. This issue arose because $Li_{2.99}Ba_{0.005}ClO$, an electrolyte, performs poorly under high pressures. Specifically, applying a pressure of 20 bar at 50ºC for 20 minutes led to this adverse effect.

High resistance in some coin cells was attributed to the hydrophilic nature of PVA, which absorbs moisture. The performance was negatively affected by the delay between SPE synthesis and its incorporation, leading to increased moisture absorption. To reduce water absorption, we could try to dry the PVA / NaAlg / $LiClO_4$ SPE in an oven, but this would seriously impair its mechanical stability and increase the likelihood of brittleness when the SPE is used in a coin cell. Moreover, any harm that water absorption has already done to the membrane cannot be undone.

Figure 4.15 shows EIS data for the NE01 cell with a 40:60 PVA / NaAlg SPE and 20% $LiClO_4$, while figure 4.16 shows EIS data for the CC03 cell, using the same SPE combined with $Li_{2.99}Ba_{0.005}ClO$.

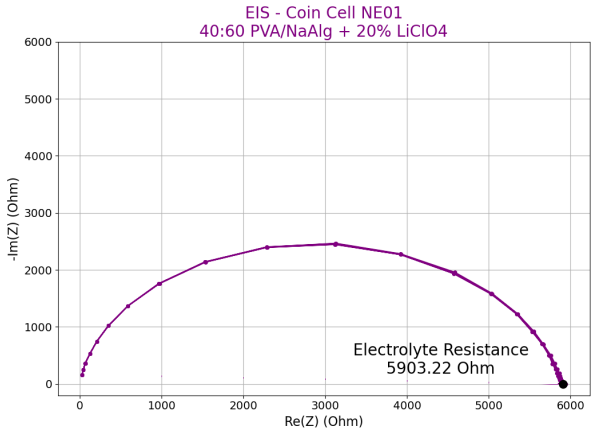

Figure 4.15: EIS - Coin Cell NE01 40:60 PVA / NaAlg / 20% $LiClO_4$

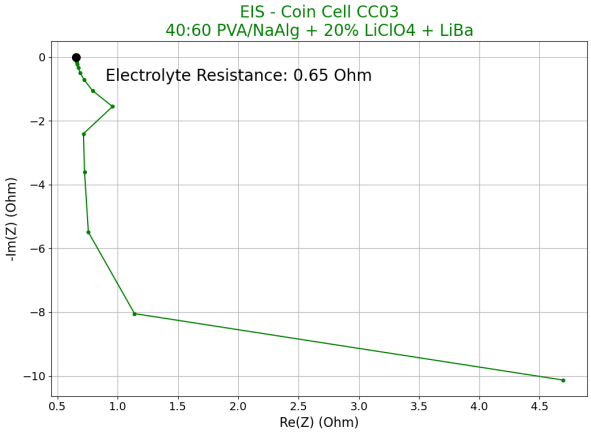

Figure 4.16: EIS - Coin Cell CC03 40:60 PVA / NaAlg / 20% $LiClO_4$ / LiBa

The EIS graph for coin cell CC03 starts with inductive behavior and exhibits an electrolyte resistance of 0.65 Ω, which is significantly lower than the 5903.22 Ω resistance observed in coin cell NE01. This inductive response is typically due to the initial polarization effects and the alignment of dipoles within the ferroelectric electrolyte. As the ferroelectric properties of $Li_{2.99}Ba_{0.005}ClO$ interact with the polymer matrix, they create an initial inductive loop reflecting the establishment of these interactions and the stabilization of the ionic pathways within the cell.

The absence of regions II, III, and IV in the EIS graph for coin cells CC03 and NE01 indicates poor electrode-electrolyte interaction, lack of ion diffusion within the electrode, and missing charge transfer at the SSE/electrode interface, preventing proper battery operation.

Figure 4.17 presents CV analysis for the NE01 coin cell, and figure 4.18 presents CV analysis for the CC03 coin cell.

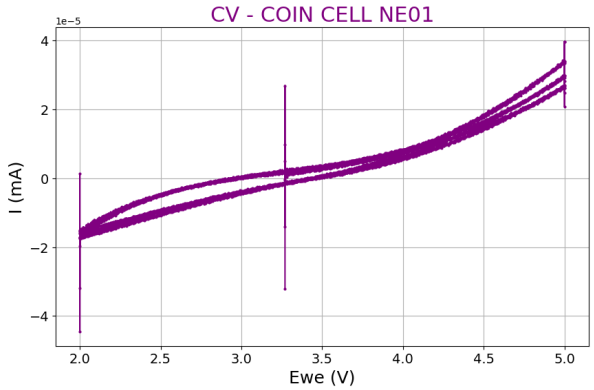

Figure 4.17: CV- Coin Cell NE01 40 % PVA / 60 % NaAlg / 20% $LiClO_4$

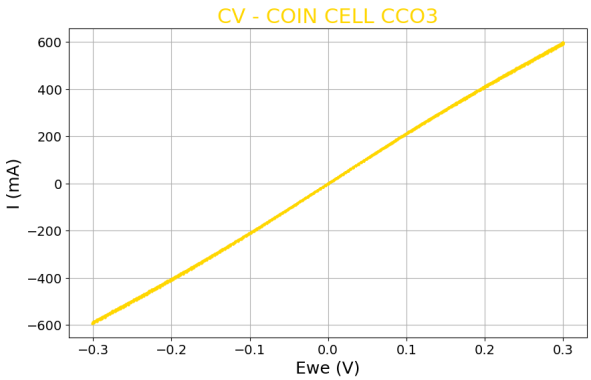

Figure 4.18: CV- Coin Cell CC03 40 % PVA / 60 % NaAlg / 20% $LiClO_4$ / LiBa

The cyclic voltammetry analysis of the two coin cells reveals significant differences in their performance. The CC03 coin cell, which combines the solid polymer electrolyte (SPE) with an amorphous glass ferroelectric electrolyte, demonstrates a much higher current capability compared to the NE01 cell. Specifically, the CC03 cell reaches current values significantly above 1 A, exceeding the maximum measurement range of our potentiostat. This indicates a superior electrochemical performance due to the synergistic effect between the SPE and LiBa. Its ferroelectric properties reduce hysteresis and improve electrochemical performance by polarizing ions from the $LiClO_4$ salt.

The NE01 coin cell exhibits cyclic voltammetry curves that do not show redox peaks, highlighting the lack of charge transfer at the interface. It behaves as a capacitor, storing energy through charge separation at the electrode-electrolyte interface (electric double layer) and pseudocapacitance. In pseudocapacitance, fast surface redox reactions partially transfer charge between ions and the electrode surface without significantly altering its chemical structure.

Graphs from figure 4.19 illustrates the charge and discharge behavior of the coin cell NE01, using an electrolyte composed of 40:60 PVA / NaAlg, and 20% $LiClO_4$, it means, only SPE.

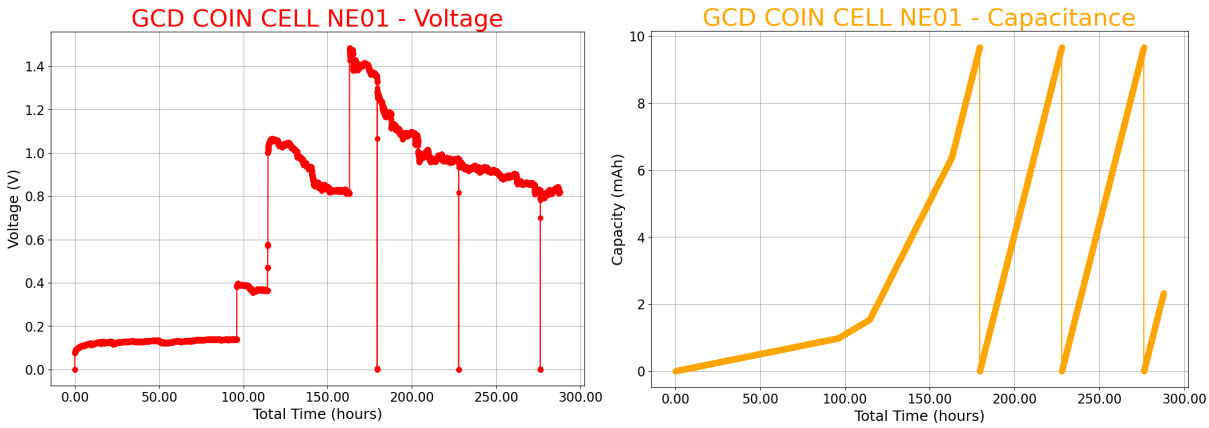

Figure 4.19: Charge/discharge of the NE01 coin cell using SPE (40% PVA, 60% NaAlg, 20% $LiClO_4$). Left: potential vs. time. Right: capacitance vs. time.

The cycle includes rest periods (1 minute each), extended charge phases (up to 179 hours), and instant discharge phases.

The rapid voltage drop during discharge is due to the capacitive behavior of the coin cell. Lithium ions accumulate on the anode surface without undergoing a redox reaction, leading to a quick discharge.

Unfortunately, we were unable to generate the charge and discharge graph for the coin cell

CC03, which consists of 40:60 PVA / NaAlg / 20% $LiClO_4$ / $Li_{2.99}Ba_{0.005}ClO$ electrolyte. This limitation arose because the high conductivity and substantial current capability of the CC03 cell, reaching up to 1 A at 0.4 V, which is the maximum measurement range of our potentiostat, exceeded the limits of the measurement equipment.

Chapter 5

Conclusions and Future Work

Comprehensive characterization tests were essential in understanding the performance of the SPEs. Techniques such as FTIR, mechanical testing, porosity analysis, and electrochemical impedance spectroscopy provided valuable insights into the structure-property relationships of these materials. Additionally, beyond the electrolyte conductivity, the activation energy and lithium ion transference number were calculated, which are important parameters for characterizing the electrolyte.

One outcome of this study is that PVDF / $LiClO_4$ SPE performance depends on the synthesis technique. While the NIPS approach yields reduced porosity electrolytes, which improve mechanical stability, the Doctor Blade methodology ensures superior $LiClO_4$ dispersion.

The findings of this thesis highlight the effectiveness of SPEs composed of PVA and NaAlg with $LiClO_4$ in enhancing ionic conductivity compared to PVDF with $LiClO_4$. PVDF / $LiClO_4$ membranes exhibited ionic conductivity ranging from $(6.06 \pm 4.67) \times 10^{-9}$ S cm^{-1} to $(3.03 \pm 1.05) \times 10^{-7}$ S cm^{-1}, while the PVA / NaAlg / $LiClO_4$ membranes showed conductivity from $(3.3 \pm 0.6) \times 10^{-8}$ S cm^{-1} to 1.3×10^{-5} S cm^{-1}.

Results also indicate that while conductivity increases with higher $LiClO_4$ concentrations, the mechanical properties tend to degrade, highlighting the need to optimize the balance between ionic conductivity and mechanical stability. Notably, the ratio of 40:60 PVA / NaAlg exhibits higher strength and higher Young´s modulus compared to 60:40 PVA / NaAlg.

The study investigated coin cells that combined SPE with an amorphous glass ferroelectric electrolyte, resulting in inductive behavior and improved electrochemical performance. This

combination increased conductivity, reaching up to 1 A with a potential of 0.3 V. It was also discovered that the SPEs needed to be sealed promptly in the coin cells to avoid moisture absorption. In this work, the coin cells were built several weeks after the SPEs were manufactured, resulting in moisture uptake and subsequent performance difficulties.

Another conclusion is that the coin cell lacks redox peaks in CV and typical EIS regions II, III, and IV, suggesting no significant redox activity at the electrode-electrolyte interfaces or ion diffusion within the electrode. It behaves like a capacitor.

This thesis provides a promising foundation because it explores solid-state lithium batteries using PVA / NaAlg / $LiClO_4$, a combination still underexplored. The use of an amorphous ferroelectric electrolyte with SPE is also a significantly underdeveloped area in this field, offering substantial potential for future research and development.

Future work should address producing membranes of uniform thickness, as having membranes of consistent thickness makes characterization tests, such as mechanical and porosity measurements, more reliable. This involves refining the production process to control factors such as drying temperature, humidity, and the percentage of $LiClO_4$.

To enhance the electrochemical performance of coin cells, particularly to achieve optimal discharge characteristics, future work will focus on optimizing the PVA / NaAlg / $LiClO_4$ membrane by synthesizing it shortly before its incorporation into the coin cell to minimize moisture contamination. Due to its high hygroscopicity, PVA can absorb a sizable amount of water from humidity when it is created and kept under uncontrolled conditions. This absorbed water can degrade the SPE membrane and may react with metallic lithium to form oxides or hydroxides that significantly reduce the coin cells' electrochemical performance.

A key focus for upcoming studies is the investigation of the electrode-electrolyte interfaces to clarify the absence of oxidation-reduction reactions, which leads to the capacitive behavior of the coin cell.

Focusing on these challenges could lead to significant advancements in solid-state lithium batteries, possibly utilizing novel electrolyte combinations with solid polymer electrolytes and ferroelectric electrolytes, as demonstrated in the promising results of the coin cell experiments.

References

[1] Maria Helena Braga. O lítio e a bateria de ião-li. *Revista Ciência Elementar*, 8(3), September 2020.

[2] European Commission. Critical raw materials. https://single-market-economy.ec.europa.eu/sectors/raw-materials/areas-specific-interest/critical-raw-materials_en, 2022.

[3] CeNTI. Investigação e desenvolvimento - centi. https://www.centi.pt/Investigacao-desenvolvimento, 2024.

[4] Beatriz Moura Gomes. Solid-state batteries based on sulfide and oxyhalide electrolytes. Master's thesis, Faculty of Engineering, University of Porto, 2023.

[5] Ayad M. Y., S. RAËL, serge Pierfederici, and Bernard Davat. Supercapacitors for embarked systems as a storage energy device solution. 11 2004.

[6] Mustafa Ergin Şahin, Frede Blaabjerg, and Ariya Sangwongwanich. A comprehensive review on supercapacitor applications and developments. *Energies*, 15(3):674, 2022.

[7] Bruno Scrosati. History of lithium batteries. *Journal of solid state electrochemistry*, 15(7):1623–1630, 2011.

[8] Roberto de Andrade Martins. Alessandro volta e a invenção da pilha: dificuldades no estabelecimento da identidade entre o galvanismo e a eletricidade. *Acta Scientianim*, 21(4):823–835, 1999.

[9] Dawn Owen. The constant battery and the daniell-becquerel-grove controversy. *Ambix*, 48(1):25–40, 2001.

[10] Lynn F Schneemeyer. Ecs classics: Making the phone system more reliable: Battery research at bell labs. *The Electrochemical Society Interface*, 25(1):54, 2016.

[11] American Chemical Society. Columbia dry cell battery - landmark. https://www.acs.org/education/whatischemistry/landmarks/drycellbattery.html, 2024. Accessed: 2024-07-03.

[12] Christian Julien, Alain Mauger, Ashok Vijh, Karim Zaghib, Christian Julien, Alain Mauger, Ashok Vijh, and Karim Zaghib. *Lithium batteries*. Springer, 2016.

[13] Giuseppe Antonio Elia, Krystan Marquardt, Katrin Hoeppner, Sebastien Fantini, Rongying Lin, Etienne Knipping, Willi Peters, Jean-Francois Drillet, Stefano Passerini, and Robert Hahn. An overview and future perspectives of aluminum batteries. *Advanced Materials*, 28(35):7564–7579, 2016.

[14] Murata Manufacturing Co., Ltd. Basic lithium-ion battery. https://article.murata.com/en-us/article/basic-lithium-ion-battery-4, 2024. Accessed: 2024-08-21.

[15] Marc Walter, Maksym V Kovalenko, and Kostiantyn V Kravchyk. Challenges and benefits of post-lithium-ion batteries. *New Journal of Chemistry*, 44(5):1677–1683, 2020.

[16] Pengcheng Zhu, Dominika Gastol, Jean Marshall, Roberto Sommerville, Vannessa Goodship, and Emma Kendrick. A review of current collectors for lithium-ion batteries. *Journal of Power Sources*, 485:229321, 2021.

[17] Hyeonggeon Lee, Niranjan Sitapure, Sungwon Hwang, and Joseph Sang-Il Kwon. Multiscale modeling of dendrite formation in lithium-ion batteries. *Computers & Chemical Engineering*, 153:107415, 2021.

[18] UPS Battery Center. Solid-state lithium batteries without dendrites. https://blog.upsbatterycenter.com/solid-state-lithium-batteries-without-dendrites/.

[19] OpenStax. Quantum tunneling of particles through potential barriers. https://phys.libretexts.org/Bookshelves/University_Physics/University_Physics_(OpenStax)/University_Physics_III_-_Optics_and_Modern_Physics_(OpenStax)/07%3A_Quantum_Mechanics/7.07%3A_Quantum_Tunneling_of_Particles_through_Potential_Barriers, 2023. Accessed: 2024-09-03.

[20] Weili Zhang, Yang Lu, Lei Wan, Pan Zhou, Yingchun Xia, Shuaishuai Yan, Xiaoxia Chen, Hangyu Zhou, Hao Dong, and Kai Liu. Engineering a passivating electric double layer for high performance lithium metal batteries. *Nature Communications*, 13(1):2029, 2022.

[21] Qisheng Wu, Matthew T McDowell, and Yue Qi. Effect of the electric double layer (edl) in multicomponent electrolyte reduction and solid electrolyte interphase (sei) formation in lithium batteries. *Journal of the American Chemical Society*, 145(4):2473–2484, 2023.

[22] Seong Jin An, Jianlin Li, Claus Daniel, Debasish Mohanty, Shrikant Nagpure, and David L Wood III. The state of understanding of the lithium-ion-battery graphite solid electrolyte interphase (sei) and its relationship to formation cycling. *Carbon*, 105:52–76, 2016.

[23] Aiping Wang, Sanket Kadam, Hong Li, Siqi Shi, and Yue Qi. Review on modeling of the anode solid electrolyte interphase (sei) for lithium-ion batteries. *NPJ Computational materials*, 4(1):15, 2018.

[24] Henry Adenusi, Gregory A Chass, Stefano Passerini, Kun V Tian, and Guanhua Chen. Lithium batteries and the solid electrolyte interphase (sei)—progress and outlook. *Advanced Energy Materials*, 13(10):2203307, 2023.

[25] Tsutomu Takamura, Morihiro Saito, Atushi Shimokawa, Chieko Nakahara, Kyoichi Sekine, Siji Maeno, and Naoki Kibayashi. Charge/discharge efficiency improvement by the incorporation of conductive carbons in the carbon anode of li-ion batteries. *Journal of power sources*, 90(1):45–51, 2000.

[26] Weijiang Xue, Lixiao Miao, Long Qie, Chao Wang, Sa Li, Jiulin Wang, and Ju Li. Gravimetric and volumetric energy densities of lithium-sulfur batteries. *Current Opinion in Electrochemistry*, 6(1):92–99, 2017.

[27] Xiaoquan Zhu, Jiale Shen, Xifan Chen, Yang Li, Wenchao Peng, Guoliang Zhang, Fengbao Zhang, and Xiaobin Fan. Enhanced cycling performance of si-mxene nanohybrids as anode for high performance lithium ion batteries. *Chemical Engineering Journal*, 378:122212, 2019.

[28] Rui Chen, Xiubin Xu, Siyu Peng, Junmin Chen, Danfeng Yu, Chuanghong Xiao, Yunlong Li, Yanting Chen, Xiaofeng Hu, Mingjie Liu, et al. A flexible and safe aqueous zinc–air battery with a wide operating temperature range from- 20 to 70° c. *ACS Sustainable Chemistry & Engineering*, 8(31):11501–11511, 2020.

[29] Zhen Jiang, Konstantin Klyukin, Kaellen Miller, and Vitaly Alexandrov. Mechanistic theoretical investigation of self-discharge reactions in a vanadium redox flow battery. *The Journal of Physical Chemistry B*, 123(18):3976–3983, 2019.

[30] Isidor Buchmann. Batteries in a portable world: a handbook on rechargeable batteries for non-engineers. 2001.

[31] John Ojur Dennis, MF Shukur, Osamah A Aldaghri, Khalid Hassan Ibnaouf, Abdullahi Abbas Adam, Fahad Usman, Yarima Mudassir Hassan, A Alsadig, Wilson L Danbature, and Bashir Abubakar Abdulkadir. A review of current trends on polyvinyl alcohol (pva)-based solid polymer electrolytes. *Molecules*, 28(4):1781, 2023.

[32] Isidor Wasylkowski. *Batteries in a Portable World: A Handbook on Rechargeable Batteries for Non-Engineers*. Fourth edition, 2017.

[33] Why ev manufacturers are switching from nmc to lfp batteries. https://www.engineering.com/story/why-ev-manufacturers-are-switching-from-nmc-to-lfp-batteries, 2023. Accessed: 2024-06-25.

[34] Man Chen, Qiujuan Sun, Yongqi Li, Ke Wu, Bangjin Liu, Peng Peng, and Qingsong Wang. A thermal runaway simulation on a lithium titanate battery and the battery module. *Energies*, 8(1):490–500, 2015.

[35] Fritz Beck and Paul Rüetschi. Rechargeable batteries with aqueous electrolytes. *Electrochimica Acta*, 45(15-16):2467–2482, 2000.

[36] Sapna Rana, Ramesh Chand Thakur, and Harmanjit Singh Dosanjh. Ionic liquids as battery electrolytes for lithium ion batteries: Recent advances and future prospects. *Solid State Ionics*, 400:116340, 2023.

[37] Xiao Tang, Shuyao Lv, Kun Jiang, Guohui Zhou, and Xiaomin Liu. Recent development of ionic liquid-based electrolytes in lithium-ion batteries. *Journal of Power Sources*, 542:231792, 2022.

[38] Seong Soo Park, Sang A Han, Rashma Chaudhary, Joo Hyeong Suh, Janghyuk Moon, Min-Sik Park, and Jung Ho Kim. Solid electrolyte: Strategies to address the safety of all solid-state batteries. *Advanced Energy and Sustainability Research*, 4(11):2300074, 2023.

[39] Yixin Wu, Yu Li, Yang Wang, Qian Liu, Qingguo Chen, and Minghua Chen. Advances and prospects of pvdf based polymer electrolytes. *Journal of Energy Chemistry*, 64:62–84, 2022.

[40] Ning Xue, Chang Zhang, and Wei Liu. Inorganic lithium-ion conductors for fast-charging lithium batteries: a review. *Journal of Solid State Electrochemistry*, pages 1–16, 2024.

[41] Chae-Ho Yim, Mohamed SE Houache, Elena A Baranova, and Yaser Abu-Lebdeh. Understanding key limiting factors for the development of all-solid-state-batteries. *Chemical Engineering Journal Advances*, 13:100436, 2023.

[42] Kanakaraj Aruchamy, Subramaniyan Ramasundaram, Sivasubramani Divya, Murugesan Chandran, Kyusik Yun, and Tae Hwan Oh. Gel polymer electrolytes: Advancing solid-state batteries for high-performance applications. *Gels*, 9(7):585, 2023.

[43] Xiaoyuan Xue, Long Wan, Wenwen Li, Xueling Tan, Xiaoyu Du, and Yongfen Tong. A self-healing gel polymer electrolyte, based on a macromolecule cross-linked chitosan for flexible supercapacitors. *Gels*, 9(1):8, 2022.

[44] Prasad Raut, Si Li, Yu-Ming Chen, Yu Zhu, and Sadhan C Jana. Strong and flexible composite solid polymer electrolyte membranes for li-ion batteries. *ACS omega*, 4(19):18203–18209, 2019.

[45] Wenjia Zhao, Jin Yi, Ping He, and Haoshen Zhou. Solid-state electrolytes for lithium-ion batteries: fundamentals, challenges and perspectives. *Electrochemical Energy Reviews*, 2:574–605, 2019.

[46] Jianjun Zhang, Jinfeng Yang, Tiantian Dong, Min Zhang, Jingchao Chai, Shanmu Dong, Tianyuan Wu, Xinhong Zhou, and Guanglei Cui. Aliphatic polycarbonate-based solid-state polymer electrolytes for advanced lithium batteries: advances and perspective. *Small*, 14(36):1800821, 2018.

[47] Anand B Puthirath, Sudeshna Patra, Shubhadeep Pal, M Manoj, Aravind Puthirath Balan, S Jayalekshmi, et al. Transparent flexible lithium ion conducting solid polymer electrolyte. *Journal of Materials Chemistry A*, 5(22):11152–11162, 2017.

[48] Shujahadeen B Aziz, Thompson J Woo, MFZ Kadir, and Hameed M Ahmed. A conceptual review on polymer electrolytes and ion transport models. *Journal of Science: Advanced Materials and Devices*, 3(1):1–17, 2018.

[49] T Sheela, RF Bhajantri, PMG Nambissan, V Ravindrachary, Blaise Lobo, Jagadish Naik, and Sunil G Rathod. Ionic conductivity and free volume related microstructural properties of liclo4/pva/naalg polymer composites: Positron annihilation spectroscopic studies. *Journal of Non-crystalline solids*, 454:19–30, 2016.

[50] O Bohnke, Cl Bohnke, and JL Fourquet. Mechanism of ionic conduction and electrochemical intercalation of lithium into the perovskite lanthanum lithium titanate. *Solid State Ionics*, 91(1-2):21–31, 1996.

[51] Jingfeng Zheng, Brian Perry, and Yiying Wu. Antiperovskite superionic conductors: a critical review. *ACS Materials Au*, 1(2):92–106, 2021.

[52] Yaokai Lu, Enyi Hu, Muhammad Yousaf, Longqing Ma, Jun Wang, Faze Wang, and Peter Lund. Nasicon-type lithium-ion conductor materials with high proton conductivity enabled by lithium vacancies. *Energy & Fuels*, 36(24):15154–15164, 2022.

[53] Chengwei Wang, Kun Fu, Sanoop Palakkathodi Kammampata, Dennis W McOwen, Alfred Junio Samson, Lei Zhang, Gregory T Hitz, Adelaide M Nolan, Eric D Wachsman, Yifei Mo, et al. Garnet-type solid-state electrolytes: materials, interfaces, and batteries. *Chemical reviews*, 120(10):4257–4300, 2020.

[54] Myeong Ju Lee, Dong Ok Shin, Ju Young Kim, Jimin Oh, Seok Hun Kang, Jumi Kim, Kwang Man Kim, Yong Min Lee, Sang Ouk Kim, and Young-Gi Lee. Interfacial barrier free organic-inorganic hybrid electrolytes for solid state batteries. *Energy Storage Materials*, 37:306–314, 2021.

[55] Lidan Fan, Mengyue Wang, Zhen Zhang, Gang Qin, Xiaoyi Hu, and Qiang Chen. Preparation and characterization of pva alkaline solid polymer electrolyte with addition of bamboo charcoal. *Materials*, 11(5):679, 2018.

[56] Dongmei Zhang, Xianglong Meng, Wenyan Hou, Weihao Hu, Jinshan Mo, Tianrong Yang, Wendi Zhang, Qianxiao Fan, Lehao Liu, Bing Jiang, et al. Solid polymer electrolytes: Ion conduction mechanisms and enhancement strategies. *Nano Res. Energy*, 2(2):e9120050, 2023.

[57] Peng Fan, Hao Liu, Vladimir Marosz, Nia T Samuels, Steven L Suib, Luyi Sun, and Libing Liao. High performance composite polymer electrolytes for lithium-ion batteries. *Advanced Functional Materials*, 31(23):2101380, 2021.

[58] Mark A Ratner and Duward F Shriver. Ion transport in solvent-free polymers. *Chemical reviews*, 88(1):109–124, 1988.

[59] Kewei Liu, Sisi Jiang, Trevor L Dzwiniel, Hong-Keun Kim, Zhou Yu, Nancy L Dietz Rago, Jae Jin Kim, Timothy T Fister, Jianzhong Yang, Qian Liu, et al. Molecular design of

a highly stable single-ion conducting polymer gel electrolyte. *ACS applied materials & interfaces*, 12(26):29162–29172, 2020.

[60] Lukas Stolz, Sebastian Hochstadt, Stephan Roser, Michael Ryan Hansen, Martin Winter, and Johannes Kasnatscheew. Single-ion versus dual-ion conducting electrolytes: the relevance of concentration polarization in solid-state batteries. *ACS applied materials & interfaces*, 14(9):11559–11566, 2022.

[61] Vera Bocharova and Alexei P Sokolov. Perspectives for polymer electrolytes: a view from fundamentals of ionic conductivity. *Macromolecules*, 53(11):4141–4157, 2020.

[62] Shujahadeen B Aziz and Zul Hazrin Z Abidin. Electrical conduction mechanism in solid polymer electrolytes: new concepts to arrhenius equation. *Journal of soft matter*, 2013(1):323868, 2013.

[63] L Sampathkumar, P Christopher Selvin, S Selvasekarapandian, P Perumal, R Chitra, and M Muthukrishnan. Synthesis and characterization of biopolymer electrolyte based on tamarind seed polysaccharide, lithium perchlorate and ethylene carbonate for electrochemical applications. *Ionics*, 25:1067–1082, 2019.

[64] P Martins, AC Lopes, and S Lanceros-Mendez. Electroactive phases of poly (vinylidene fluoride): Determination, processing and applications. *Progress in polymer science*, 39(4):683–706, 2014.

[65] Liuxia Ruan, Xiannian Yao, Yufang Chang, Lianqun Zhou, Gaowu Qin, and Xianmin Zhang. Properties and applications of the β phase poly (vinylidene fluoride). *Polymers*, 10(3):228, 2018.

[66] Anil Arya and AL Sharma. Tailoring of the structural, morphological, electrochemical, and dielectric properties of solid polymer electrolyte. *Ionics*, 25:1617–1632, 2019.

[67] Khushbu Gohel and DK Kanchan. Ionic conductivity and relaxation studies in pvdf-hfp: Pmma-based gel polymer blend electrolyte with liclo4 salt. *Journal of Advanced Dielectrics*, 8(01):1850005, 2018.

[68] YJ Shen, M Jaipal Reddy, and Peter P Chu. Porous pvdf with liclo4 complex as 'solid'and 'wet'polymer electrolyte. *Solid State Ionics*, 175(1-4):747–750, 2004.

[69] YS Zhu, XJ Wang, YY Hou, XW Gao, LL Liu, YP Wu, and M Shimizu. A new single-ion polymer electrolyte based on polyvinyl alcohol for lithium ion batteries. *Electrochimica Acta*, 87:113–118, 2013.

[70] Li Ping Teo, Mohd Hamdi Buraidah, and Abdul Kariem Arof. Development on solid polymer electrolytes for electrochemical devices. *Molecules*, 26(21):6499, 2021.

[71] I Gunawan, B Sugeng, et al. Synthesis and characterization of pva blended liclo4 as electrolyte material for battery li-ion. In *IOP Conference Series: Materials Science and Engineering*, volume 223, page 012039. IOP Publishing, 2017.

[72] Shuijiao Peng, Xingzong Jiang, Xiaotong Xiang, Kai Chen, Guoqi Chen, Xiancai Jiang, and Linxi Hou. High-performance and flexible solid-state supercapacitors based on high toughness and thermoplastic poly (vinyl alcohol)/nacl/glycerol supramolecular gel polymer electrolyte. *Electrochimica Acta*, 324:134874, 2019.

[73] Naman Jain, Vinay Kumar Singh, and Sakshi Chauhan. A review on mechanical and water absorption properties of polyvinyl alcohol based composites/films. *Journal of the Mechanical Behavior of Materials*, 26(5-6):213–222, 2017.

[74] Designerdata. Polyvinylidene fluoride (pvdf). https://designerdata.nl/materials/plastics/thermo-plastics/polyvinylidene-fluoride, 2024. Accessed: 2024-07-11.

[75] Haigang Yang, Shoubin Xu, Long Jiang, and Yi Dan. Thermal decomposition behavior of poly (vinyl alcohol) with different hydroxyl content. *Journal of Macromolecular Science, Part B*, 51(3):464–480, 2012.

[76] M Helena Braga, Joana E Oliveira, Tianhan Kai, Andrew J Murchison, Allen J Bard, and John B Goodenough. Extraordinary dielectric properties at heterojunctions of amorphous ferroelectrics. *Journal of the American Chemical Society*, 140(51):17968–17976, 2018.

[77] M Helena Braga, Andrew J Murchison, Jorge A Ferreira, Preetam Singh, and John B Goodenough. Glass-amorphous alkali-ion solid electrolytes and their performance in symmetrical cells. *Energy & Environmental Science*, 9(3):948–954, 2016.

[78] Yuhuan Xu. *Ferroelectric materials and their applications*. Elsevier, 2013.

[79] Nazar Khalaf Mahan, Ehab Mohammed Ali, Ahmed N Abd, et al. Synthesis of cds: Cu5% thin films by chemical method based on silicon for gas sensor applications. *Materials Today: Proceedings*, 45:5800–5803, 2021.

[80] Ganesh C Patil. Doctor blade: A promising technique for thin film coating. In *Simple Chemical Methods for Thin Film Deposition: Synthesis and Applications*, pages 509–530. Springer, 2023.

[81] João Teixeira, Vanessa Fernandes Cardoso, Gabriela Botelho, António Miguel Morão, João Nunes-Pereira, and Senentxu Lanceros-Mendez. Effect of polymer dissolution temperature and conditioning time on the morphological and physicochemical characteristics of poly (vinylidene fluoride) membranes prepared by non-solvent induced phase separation. *Polymers*, 13(23):4062, 2021.

[82] Lukas Stolz, Gerrit Homann, Martin Winter, and Johannes Kasnatscheew. Realizing poly (ethylene oxide) as a polymer for solid electrolytes in high voltage lithium batteries via simple modification of the cell setup. *Materials Advances*, 2(10):3251–3256, 2021.

[83] AOTBattery. Coin cell batteries material. https://www.aotbattery.com/new/Coin-Cell-Batteries-Marerial.html. Accessed: 2024-07-14.

[84] Beatriz Arouca Maia, Beatriz Moura Gomes, Antonio Nuno Guerreiro, Raquel Miriam Santos, and Maria Helena Braga. Cathodes pinpoints for the next generation of energy storage devices: the lifepo4 case study. *Journal of Physics: Materials*, 7(2):025001, 2024.

[85] MSE Supplies LLC. Mse pro single-side lithium iron phosphate ($lifepo_4$) coated aluminum foil for battery research, 260mm x 230mm x 90um, 5 sheets/pack, 2024. Accessed: 2024-07-19.

[86] Renheng Wang, Weisheng Cui, Fulu Chu, and Feixiang Wu. Lithium metal anodes: Present and future. *Journal of Energy Chemistry*, 48:145–159, 2020.

[87] Allan Hynes, David A Scott, Angela Man, David L Singer, Michael G Sowa, and Kan-Zhi Liu. Molecular mapping of periodontal tissues using infrared microspectroscopy. *BMC medical imaging*, 5:1–10, 2005.

[88] M.A. Mohamed, J. Jaafar, A.F. Ismail, M.H.D. Othman, and M.A. Rahman. Chapter 1 - fourier transform infrared (ftir) spectroscopy. In Nidal Hilal, Ahmad Fauzi Ismail, Takeshi Matsuura, and Darren Oatley-Radcliffe, editors, *Membrane Characterization*, pages 3–29. Elsevier, 2017.

[89] Endah R Dyartanti, Agus Purwanto, I Nyoman Widiasa, and Heru Susanto. Ionic

conductivity and cycling stability improvement of pvdf/nano-clay using pvp as polymer electrolyte membranes for lifepo4 batteries. *Membranes*, 8(3):36, 2018.

[90] Jianjun Zhang, Zhihong Liu, Qingshan Kong, Chuanjian Zhang, Shuping Pang, Liping Yue, Xuejiang Wang, Jianhua Yao, and Guanglei Cui. Renewable and superior thermal-resistant cellulose-based composite nonwoven as lithium-ion battery separator. *ACS applied materials & interfaces*, 5(1):128–134, 2013.

[91] Ioannis Tranoudis and Nathan Efron. Tensile properties of soft contact lens materials. *Contact Lens and Anterior Eye*, 27(4):177–191, 2004.

[92] Thermo Fisher Scientific. How does libs work? Accessed: 2024-07-15.

[93] IndiaMART. Swagelok type cell. https://www.indiamart.com/proddetail/swagelok-type-cell-2849741863662.html, 2024. Accessed: 2024-09-10.

[94] Laurence A Middlemiss, Anthony JR Rennie, Ruth Sayers, and Anthony R West. Characterisation of batteries by electrochemical impedance spectroscopy. *Energy Reports*, 6:232–241, 2020.

[95] Juvissan Aguedo, Lenka Lorencova, Marek Barath, Pavol Farkas, and Jan Tkac. Electrochemical impedance spectroscopy on 2d nanomaterial mxene modified interfaces: application as a characterization and transducing tool. *Chemosensors*, 8(4):127, 2020.

[96] Xinming Qian, Ningyu Gu, Zhiliang Cheng, Xiurong Yang, Erkang Wang, and Shaojun Dong. Methods to study the ionic conductivity of polymeric electrolytes using ac impedance spectroscopy. *Journal of Solid State Electrochemistry*, 6:8–15, 2001.

[97] Lei Zhang, Yao Dai, Chao Li, Yuzhen Dang, Runguo Zheng, Zhiyuan Wang, Yuan Wang, Yanhua Cui, Hamidreza Arandiyan, Zongping Shao, et al. Recent advances in electrochemical impedance spectroscopy for solid-state batteries. *Energy Storage Materials*, page 103378, 2024.

[98] Olfa Kanoun. Impedance spectroscopy advances and future trends: A comprehensive review. *Impedance Spectroscopy*, pages 1–22, 2018.

[99] Fengliu Lou and De Chen. Aligned carbon nanostructures based 3d electrodes for energy storage. *Journal of Energy Chemistry*, 24(5):559–586, 2015.

[100] Vadim F Lvovich. *Impedance spectroscopy: applications to electrochemical and dielectric phenomena*. John Wiley & Sons, 2012.

[101] Noémie Elgrishi, Kelley J Rountree, Brian D McCarthy, Eric S Rountree, Thomas T Eisenhart, and Jillian L Dempsey. A practical beginner's guide to cyclic voltammetry. *Journal of chemical education*, 95(2):197–206, 2018.

[102] Department of Chemical Engineering and Biotechnology. Linear sweep and cyclic voltammetry: The principles. https://www.ceb.cam.ac.uk/research/groups/rg-eme/Edu/linear-sweep-and-cyclic-voltametry-the-principles, 2024. Accessed: 2024-07-16.

[103] Anil Arya, Mohd Sadiq, and Achchhe Lal Sharma. Structural, electrical and ion transport properties of free-standing blended solid polymeric thin films. *Polymer Bulletin*, 76(10):5149–5172, 2019.

[104] L Ye and Z Feng. Polymer electrolytes as solid solvents and their applications. In *Polymer electrolytes*, pages 550–582. Elsevier, 2010.

[105] F. Licht, M.A. Davis, and H.A. Andreas. Charge redistribution and electrode history impact galvanostatic charging/discharging and associated figures of merit. *Journal of Power Sources*, 446:227354, 2020.

[106] Yustinus Purwamargapratala, Evi Yulianti, Wagiyo Honggowiranto, Evvy Kartini, et al. Electrochemical impedance spectroscopy study of lifepo4/li during discharging process. In *IOP Conference Series: Materials Science and Engineering*, volume 924, page 012035. IOP Publishing, 2020.

[107] Iuliana Mihaela Jipa, Anicuta Stoica, Marta Stroescu, Loredana-Mihaela Dobre, Tanase Dobre, Sorin Jinga, and Christu Tardei. Potassium sorbate release from poly (vinyl alcohol)-bacterial cellulose films. *Chemical Papers*, 66:138–143, 2012.